VYSOKÉ UČENÍ TECHNICKÉ V BRNĚ

BRNO UNIVERSITY OF TECHNOLOGY

FAKULTA STROJNÍHO INŽENÝRSTVÍ
ÚSTAV FYZIKÁLNÍHO INŽENÝRSTVÍ

FACULTY OF MECHANICAL ENGINEERING
INSTITUTE OF PHYSICAL ENGINEERING

PROPAGATION OF FATIGUE CRACKS UNDER SHEAR LOADING MODES II, III AND II+III IN THE NEAR-THRESHOLD REGION

PROPAGATION OF FATIGUE CRACKS UNDER SHEAR LOADING MODES II, III AND II+III IN THE NEAR-THRESHOLD REGION

DIZERTAČNÍ PRÁCE
DOCTORAL THESIS

AUTOR PRÁCE — Ing. TOMÁŠ VOJTEK
AUTHOR

VEDOUCÍ PRÁCE — prof. RNDr. JAROSLAV POKLUDA, CSc.
SUPERVISOR

BRNO 2014

Abstract

The work is focused on fatigue crack propagation under modes II, III and II + III in the near-threshold region in metallic materials. Experiments were conducted for ARMCO iron, titanium, nickel and stainless steel on three types of specimens for shear-mode crack loading. A special technique of precrack generation was used which enabled a closure-free loading at the beginning of the shear-mode experiments. For all investigated materials the effective thresholds under the remote mode II loading were found to be about 1.7 times lower than those under the remote mode III. Tendency to local mode I branching was assessed by a measurement of local deflection and twist angles of fracture facets using stereophotogrammetry in SEM. The lowest angles of both mode II and mode III cracks were identified for the ARMCO iron, the intermediate ones in titanium and nickel and the highest ones (pure mode I branches) were determined for the stainless steel. These differences can be explained by different numbers of available slip systems in crystal lattices of investigated materials. Ratios of measured effective thresholds in modes I, II and III were compared with results predicted by theoretical models. An analytical formula for effective mode-II thresholds was proposed and found in a good agreement with experimental results. The mode I branching criterion in terms of effective thresholds led to a critical deflection angle of $\approx 40°$ related to a transition from local shear to opening mode.

Abstrakt

Práce je zaměřena na šíření únavových trhlin v módech II, III a II + III v prahové oblasti v kovových materiálech. Byly provedeny experimenty pro ARMCO železo, titan, nikl a austenitickou ocel na třech druzích vzorků pro zatěžování trhliny ve smykových módech. Byl použit zvláštní způsob vytváření iniciační trhliny, který eliminoval efekt zavírání trhliny na začátku smykového zatěžování. Ve všech zkoumaných materiálech byly efektivní prahové hodnoty v módu II přibližně 1,7-krát nižší než v módu III. Měřením úhlů lokálních odklonů a natočení lomových faset s použitím stereofotogrammetrie v SEM bylo usuzováno na tendenci trhliny k vyhýbání do lokálního módu I. Nejmenší úhly byly zjištěny u ARMCO železa pro trhliny v módech II i III, středně velké úhly u titanu a niklu a největší úhly (vyhnutí do čistého módu I) byly pozorovány u austenitické oceli. Tyto rozdíly lze vysvětlit různým počtem dostupných skluzových systémů v krystalových mřížkách daných materiálů. Poměry mezi naměřenými prahovými hodnotami v módu I, II a III byly srovnány s předpověďmi teoretických modelů. Byl navržen analytický vztah pro efektivní prahové hodnoty v módu II, který byl v dobré shodě s experimentálními výsledky. Pomocí efektivních prahových hodnot bylo vyčísleno kritérium pro vyhýbání do módu I, které vedlo ke kritickému úhlu odklonu $\approx 40°$ souvisejícímu s přechodem z lokálního smykového módu do otevíracího módu.

Key Words

shear-mode fatigue cracks, effective threshold, dislocation crack growth models, mode I branching, quantitative fractography, metallic materials

Klíčová slova

smykové únavové trhliny, efektivní prahové hodnoty, dislokační modely růstu trhlin, vyhýbání do módu I, kvantitativní fraktografie, kovové materiály

VOJTEK, T. *Propagation of Fatigue Cracks under Shear Loading Modes II, III and II+III in the Near-threshold Region.* Brno: Vysoké učení technické v Brně, Fakulta strojního inženýrství, 2014. 72 s. Vedoucí dizertační práce prof. RNDr. Jaroslav Pokluda, CSc.

Čestné prohlášení

Prohlašuji, že jsem disertační práci vypracoval samostatně a že všechny použité literární zdroje jsem správně a úplně ocitoval.

.....

Ing. Tomáš Vojtek

Acknowledgements

It would like to express my gratitude to Prof. Jaroslav Pokluda for his kind help, advice, guidance and dedication of much of his time to my Ph.D. study. I am also very grateful to Prof. Reinhard Pippan and Dr. Anton Hohenwarter from the Erich Schmid Institute of Materials Science in Leoben for their help and guidance as well as to other colleagues from this institute, especially Dr. Stefan Wurster, Dr. Johannes Zechner and Dipl.-Ing. Peter Kutleša for their helping hands. Finally, I would like to thank to Assoc. Prof. Jana Horníková and Prof. Pavel Šandera for their support.

Table of Contents

1 Introduction

The history of studies of fatigue shear cracks is much shorter than that of cracks under push-pull loading. In fact, the systematic research in this field started only after 1970 [1-10]. The first works dealing with shear cracks were focused on mixed modes I + II and I + III loading and complicated fracture morphologies (factory roofs) obtained after torsion loading. A significance of friction effects caused by interaction of asperities in the crack wake was already recognized. A superimposed static mode I loading accelerated crack growth rates due to friction stress removal. On the other hand, a superposition of static mode III on the cyclic mode I loading was found to have the effect of slowing down the crack growth, which was also quantitatively described [4]. Data on mode II, mode III and mixed mode II + III crack growth for various materials were preferentially reported in later works [11-17]. In a more recent study [18] the influence of superimposed out-of-phase cyclic compressive loading on mode III crack growth was observed and discussed in terms of smoothing the crack-wake asperities and inducing tensile residual stresses, which also increased the crack growth rate. An exception to the friction problems are microstructurally short cracks growing in the mixed mode I + II during the stage I. in push-pull loading [19,20], where practically no roughness-induced closure takes place. Behaviour of these cracks is, however, not a part of the focus of this work.

Precise experimental measurements are required in order to get closer to the inherent properties of materials and to compare them with the theoretical predictions. However, in the case of shear-modes cracks only a few of such data are available due to experimental problems connected to roughness-induced crack closure and the related local superposition of mode I (e.g., [12]). Therefore, propagation of long fatigue cracks under shear loading modes II, III and II + III in metallic materials is still one of the strong fields in the world fatigue research. Recent possibilities of modelling of materials properties (discrete dislocations dynamics with the support of molecular dynamics and ab-initio calculations) enable a deeper insight into the physical mechanisms of crack propagation [19,21,22]. Basic considerations concerning these micromechanistic models are presented in Section 1.3.

One of the important mechanical properties of materials is a parameter that determines the transition from non-propagation to propagation of a cyclically loaded crack. Under small-scale yielding in metals this parameter is represented by the *threshold of the stress intensity factor range* (SIFR). In order to discuss the crack propagation phenomena near the threshold, it is helpful to divide the crack loading mechanisms into two groups – extrinsic and intrinsic ones [23,24]. The intrinsic (effective) mechanisms are responsible for the generation of new fracture surfaces at the crack tip, i.e., the fatigue crack propagation. The extrinsic (shielding) mechanisms occur in the surrounding of the crack tip as contacts of fracture surfaces during the cyclic loading, usually called crack closure. Hence, the resistance to fatigue crack growth in metallic materials consists of two components: effective and crack-closure induced. The related friction stresses, particularly pronounced in mode II and mode III loading, reduce the real acting crack driving force at the crack tip (Eq. (1)) which is called the *effective driving force* or the effective SIFR.

$$\boxed{\Delta K_{\text{applied}} = \Delta K_{\text{effective}} + \Delta K_{\text{closure}}} \tag{1}$$

1.1 Background

1.1.1 Lack of Effective Data

As mentioned above, the resistance against the fatigue crack growth consists of an effective part and a contribution induced by crack closure. There is still a limited knowledge of basic mechanisms of the effective resistance to shear-mode crack growth, in particular, a lack of experimental data on effective thresholds $\Delta K_{\mathrm{IIeff,th}}$ and $\Delta K_{\mathrm{IIIeff,th}}$ and only a few data available on effective crack-growth rates in the Paris-Erdogan region [7,8,14]. The measured data of shear-mode cracks in engineering materials suffer from highly different levels of the friction-induced component, depending on many factors as precrack roughness, material microstructure, residual stress, loading amplitude, cyclic ratio, $\Delta K_{\mathrm{II}}/\Delta K_{\mathrm{III}}$ ratio, loading frequency, environment, etc. Therefore, measured values of remote thresholds $\Delta K_{\mathrm{II,th}}$ and $\Delta K_{\mathrm{III,th}}$ are usually higher than those of $\Delta K_{\mathrm{I,th}}$, although the effective values $\Delta K_{\mathrm{IIeff,th}}$ and $\Delta K_{\mathrm{IIIeff,th}}$ should be less than or comparable to $\Delta K_{\mathrm{Ieff,th}}$.

1.1.2 Closure-induced Resistance

The knowledge of mechanisms of the closure-induced resistance component, which becomes significant particularly in the near-threshold regime, is somewhat better. Here, the size of the shear-mode plastic zone is typically less than (or comparable to) that of the characteristic microstructural features (grains, secondary phases or particles) which causes a microstructure-induced tortuosity of the crack front and a creation of crack-wake asperities [25].

In contrast to the mode I crack growth, where the crack surface interaction in the tensile part of a cycle is usually small, interaction of shear-mode crack surfaces is, during the whole cycle, accompanied by the following effects:

- interlocking of asperities in the crack wake,
- frictional stress fields between crack flanks,
- roughness-induced mode I at the crack front.

Since the height of asperities is usually significantly greater than the crack tip shear-opening displacements, the related premature contact of asperities produces a high friction stress that usually increases with crack extension. This leads either to a crack arrest or its deflection (branching) to mode I. Besides the friction stress, the contact of asperities in the crack wake also induces an additional mode I component [26]. Therefore, a quantification of the closure component for shear-mode cracks is a very demanding problem and only rough assessments can be made using simplified analytical or numerical models for various metallic materials [18,26,15]. These effects may become a major part of the resistance to crack growth in the near-threshold region.

On the other hand, the crack-wake roughness becomes smoothed by an intensive abrasive wear (reduced friction) under large-scale yielding conditions since the shear displacements become comparable or larger than the size of asperities. At the same time, the density of crack initiation sites along the precrack front becomes higher [19,27,28]. For pure geometrical reasons, therefore, the size of crack-wake asperities in form of branches or factory roofs reduces and completely vanishes in the very low-cycle fatigue regime. Moreover, the shear-

mode cyclic plastic zone is widely extended along the maximum shear plane thus embracing many characteristic microstructural elements and promoting the damage mechanism based on the coalescence of the main crack with microcracks nucleated inside the plastic zone. As a result of all these effects, the large-scale yielded cracks keep growing nearly along the maximum shear plane without any remarkable mode I branching [9,19,29].

The effects of asperities interactions on the effective mode III stress intensity factor (SIF) were evaluated [15] for circumferentially cracked round shafts loaded by torsion. Various pressure distributions between mating fracture surfaces were considered. The results showed that when the applied mode III stress intensity range reached its critical value, the fracture surface becomes macroscopically flat and the friction stress becomes insignificant. The critical value depends on the height and the wavelength of asperities.

1.2 Goals of the Work

The knowledge of long shear cracks behaviour improved during the last years before the start of this Ph.D. work but many aspects were still not sufficiently described or remained unclear. The most important unresolved aspects were:

- determination of effective (intrinsic) threshold values $\Delta K_{\mathrm{IIeff,th}}$, $\Delta K_{\mathrm{IIIeff,th}}$ and identification of underlying mechanisms of effective resistance to crack growth,
- experimental comparison of the near-threshold crack growth rates in modes II and III,
- quantitative description of a competition between shear and opening modes,
- appropriate description of the mixed-mode II + III crack growth data.

The main goal of this Ph.D. work is to accomplish these four points by performing and evaluating experiments with pure shear-mode crack propagation, followed by a detailed quantitative fractography analysis in three dimensions (3D) in order to investigate the crack paths and the related local crack propagation modes. The additional goals comprise improving of a special experimental method developed and reported in [30] and to extend this method to other specimen types in order to verify the measured data and to improve mutual comparison of crack growth rates obtained for modes II and III.

The basic ideas are related to distinguishing between the macroscopic and local crack propagation mode. Crack growth under macroscopic mode is described by '*classical fracture mechanics*' (linear elastic fracture mechanics) whereas '*micromechanics of fracture*' focuses on microscopic level of local crack growth and the influence of microstructure of the material, which is essential for explaining the crack propagation mechanisms. Therefore, emphasis is put on the latter approach in this work. A comparison of predictions of classical fracture mechanics criteria for mode I crack deviation [31] with the observed material behaviour is, however, one of the goals of this work as well.

1.3 Basic Micromechanistic Models of Propagation of Ideal Cracks

Fatigue damage of macroscopically homogeneous and isotropic material elements ahead of the crack front of equally loaded pure mode II and mode III cracks was, for a rather long time, considered to be identical [32]. Therefore, mode II and mode III crack growth rates $(\mathrm{d}a/\mathrm{d}N)_{\mathrm{II}}$ and $(\mathrm{d}a/\mathrm{d}N)_{\mathrm{III}}$ as well as the related thresholds $\Delta K_{\mathrm{II,th}}$ and $\Delta K_{\mathrm{III,th}}$ were also expected to be equal. However, there are several experimental indications [16,33,34,35] that $\Delta K_{\mathrm{III,th}} > \Delta K_{\mathrm{II,th}}$ and $(\mathrm{d}a/\mathrm{d}N)_{\mathrm{III}} < (\mathrm{d}a/\mathrm{d}N)_{\mathrm{II}}$ which is also taken into account in numerical codes for 3D crack propagation [36,37]. The explanation can be based on the fact that the damage caused by mode II and III loading in materials elements directly connected with the crack front is significantly different [38]. In particular, the mode III displacements do not lead to a straightforward creation of new fracture surfaces as the mode II ones (see hereafter in more detail).

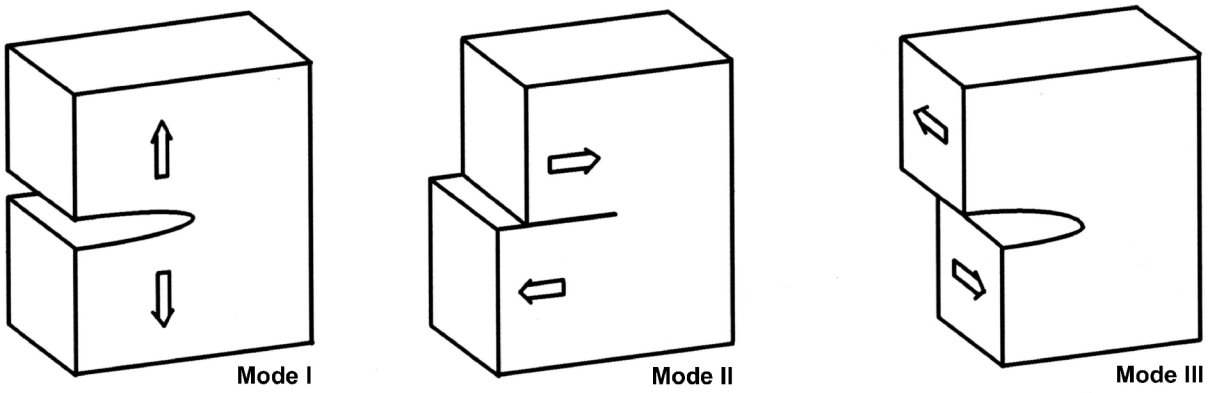

Fig. 1. Definition of the three crack loading modes.

The three modes of crack loading are schematically illustrated in Fig. 1. In mode I, the opening mode, the loading is normal to the crack plane. In mode II, the in-plane shear, the shear loading is applied in the plane of the crack normal to the crack front. In mode III, the antiplane shear, the shear loading is applied in the plane of the crack parallel to the crack front [39]. Any crack loading can be expressed by superposition of those three modes. In this section, models of micromechanisms of fatigue crack propagation are discussed. The principle of this approach is that the crack propagation is a consequence of cyclic plasticity at the crack tip which has a discrete nature, i.e., the explanations are based on movements of dislocations.

Near-threshold fatigue cracks in metallic materials propagate by a creation of new free surfaces connected to the crack front rather than by a continuous accumulation of damage inside the plastic zone. There are two most physically based models of fatigue crack growth that differ with respect to the generation of new fracture surfaces by means of a movement of discrete dislocations [40-44]. Both models, originally considered only for mode I loading, assume an ideal crack with plane crack flanks and straight crack front and predict the existence of crack-growth threshold as a consequence of the discrete nature of plasticity. Note that this is not the case of crack-growth models based on continuum mechanics [41]. In the following, these two models will be briefly introduced.

1.3.1 Deformation Model

In this model [40-42] the fatigue crack propagation is a consequence of a deformation-induced generation of new surfaces in terms of the formation of dislocation slip steps on a free surface.

Ideal crack Lying in the Slip Plane

The simplest explanation can be done for the case of a crack plane lying in a slip plane (coplanar crack) or inclined only by a small angle with respect to the slip plane. Moreover, the crack front is considered to be exactly perpendicular to the slip direction for modes I and II and parallel with the slip direction for mode III.

In mode I, the creation of new fracture surface accomplishes by blunting during loading and re-sharpening during unloading as schematically depicted in Fig. 2. The mechanism is similar to the models proposed by Pelloux [45] and Neumann [46] or the models based on the direct observation of the crack propagation at larger crack propagation rates [47,48]. Due to both the small cyclic plastic zone near the threshold and the limited number of available dislocation sources the movements of dislocations emitted from the crack tip will dominate the cyclic plastic deformation. New surface is generated by a formation of dislocation slip steps on free surfaces. Edge dislocations are emitted from the crack tip in two symmetrically oriented slip systems with respect to the crack plane. Such generated dislocations are usually called ‘shielding’ because they repulse the next dislocations emitted from the crack tip by external loading. During unloading, some of them return back to the crack tip and re-sharpen it. The newly created surfaces will not re-weld due to oxidation. As a consequence, the crack will propagate cycle per cycle with a growth rate proportional to the cyclic crack tip opening displacement. Since a critical stress concentration, i.e., a critical local stress intensity, is needed to emit a dislocation from the crack tip and due to the fact that the dislocations move away from this stress concentration, a certain minimum ΔK is necessary to cause cyclic plastic deformation: this ΔK determines $\Delta K_{\mathrm{eff,th}}$. For a symmetric arrangement of slip planes the crack propagates in an ideal mode I manner even on the local scale. For a usual case of asymmetric arrangement of slip planes, the crack should propagate predominately along the dominant slip plane, i.e., in a serrated crystallographic manner.

Mode II

The classical crack-growth models proposed, e.g., by Weertman [49] for mode I loading are based on a continuous accumulation of fatigue damage ahead of the crack tip. When adopting this phenomenological model also for shear-mode cracks, both the crack growth rates and the effective thresholds in modes II and III should be equal. As argued by Murakami [32], an isotropic material element inside the process zone ahead of the crack front should not “feel” any difference in fatigue damage accumulation caused by modes II and III. However, the real mechanism of shear-mode fatigue crack growth in metallic materials is not so simple.

In mode II, the dislocations generated in the deformation model will cause crack sliding displacements ahead of the crack tip and generate new surfaces, see Fig. 2. If there is a sufficient number of slip systems in the lattice the crack should preferentially propagate in a nearly coplanar mode II manner, with small inclinations to the direction where the tensile stresses are developed during the crack-tip loading. Such a small deflection generates an opening of the crack during loading, thus reducing crack closure and friction of the crack flanks.

Mode III

For the mode III case the explanation of crack propagation is more difficult. In the ideal deformation-based model [40], the slip plane of screw dislocations is co-planar with the crack plane and their Burgers vector is parallel to the crack front. If mode III cyclic plastic shear displacements appear at that front then no new fracture surface is generated and the crack does not propagate at all. This corresponds to the phenomenon that a deformation produced by dislocations with a Burgers vector parallel to a free surface does not cause surface steps at the crack front. However, such an ideal crack/slip configuration is very unlikely. The Burgers vector will always have a certain component in the crack propagation direction. Hence, even in the case of an ideal straight crack front the mode III loading will initiate not only a plastic mode III crack tip displacement but also generate a certain sliding displacement in the mode II direction generating new surfaces [50]. A deviation from the ideal straight crack front is a further reason that a mode III crack can propagate by a deformation-induced new surface generation [38]. Microscopic serrations of the crack front in the plane of the crack locally generate a mixture between mode II and mode III loading. Even if the local mode III segments of the crack front do not propagate the mode II segments should propagate and, in the pure deformation-based model, the crack will propagate in the plane of the crack – see Sub-section 1.3.4 for more detail.

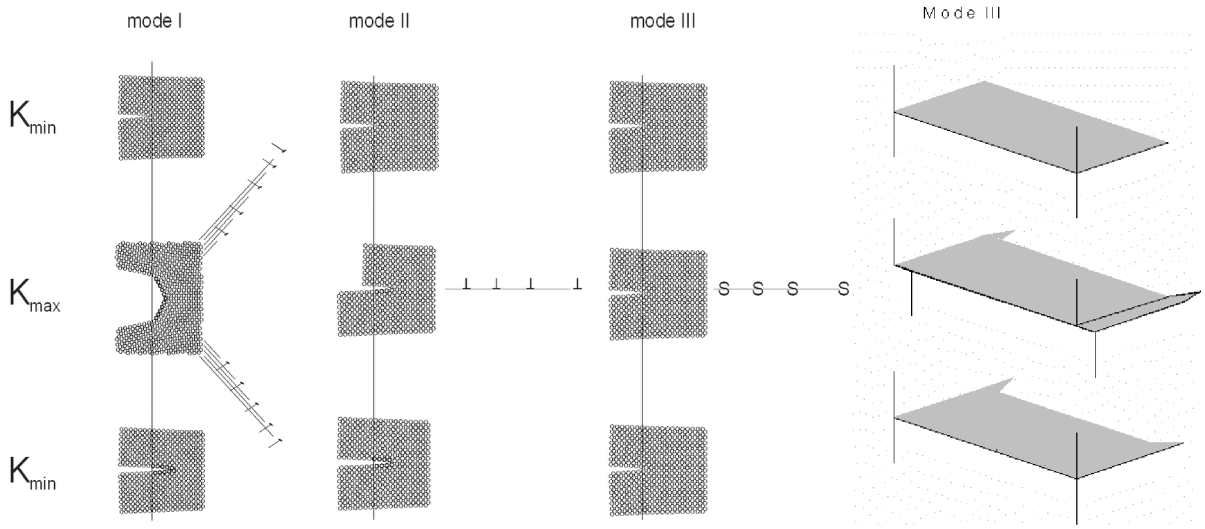

Fig. 2. Illustration of microscopic crack extension in modes I, II and III and a macroscopic scheme for mode III.

Crack Front Inclined by High Angle from the Slip Planes

In polycrystalline materials, the slip planes are usually deflected from the crack plane with a line intersection (“deflected” slip planes) or the slip planes intersect the crack front in one point (“oblique” slip planes).

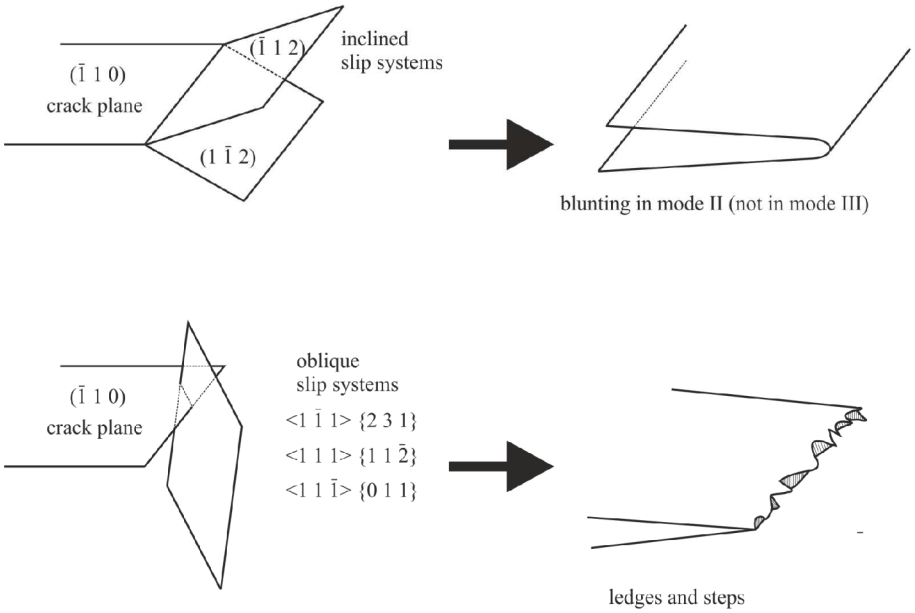

Fig. 3. Deflected and oblique slip planes with the corresponding crack front extension [21, 22].

For example, for a crack lying in the $(\bar{1}10)$ plane in a bcc crystal, molecular dynamics simulations were done in [21,22] to identify the picture of fatigue damage at the crack tip. When the slip planes intersect at the crack front $\langle 110 \rangle$, i.e. the planes $(\bar{1}12)$ and $(1\bar{1}2)$, the mode I crack propagates in an ideal manner described above. During mode II loading, edge dislocations move in the intersecting slip planes and the crack propagates by blunting and re-sharpening similarly to the case of mode I (see Fig. 3). However, this process is less effective than that in the ideal mode II case in Fig. 2.

If the slip planes do not intersect the crack plane at the crack front (oblique slip systems $\langle 1\bar{1}1 \rangle \{231\}$, $\langle 111 \rangle \{11\bar{2}\}$ and $\langle 11\bar{1} \rangle \{011\}$), small steps and protrusions of new fracture surface are generated (Fig. 3). In this case mode III crack propagation is only possible due to a generation of microcracks in the cyclic plastic zone and their coalescence with the main crack front.

1.3.2 Decohesion Model

The second model, proposed by Deshpande, Needleman and Van der Giessen [43,44], is based on multiscale numerical simulations and assumes that plasticity is caused by dislocation sources away from the crack tip only. The generated dislocations form the plastic zone with some of the dislocations running out of the crack flanks. Most of the dislocations shield the crack tip from the external loading, which allows applying stress intensity factors larger than the Griffith's stress intensity K_G. However, a few dislocations also cause anti-shielding. If one of them comes very close to the crack tip it can induce a nanoscopic decohesion. In other words, when the tensile stress fields of the crack and the dislocation have a sufficient overlap, the crack will propagate by decohesion until it reaches the anti-shielding dislocation as schematically depicted in Fig. 4. Such a process can, most probably, occur only if the anti-shielding dislocation is just a few lattice spacings away from the crack front. The crack should not propagate on a slip plane, rather it would predominately grow under the local mode I on a cleavage plane or in a non-crystallographic manner.

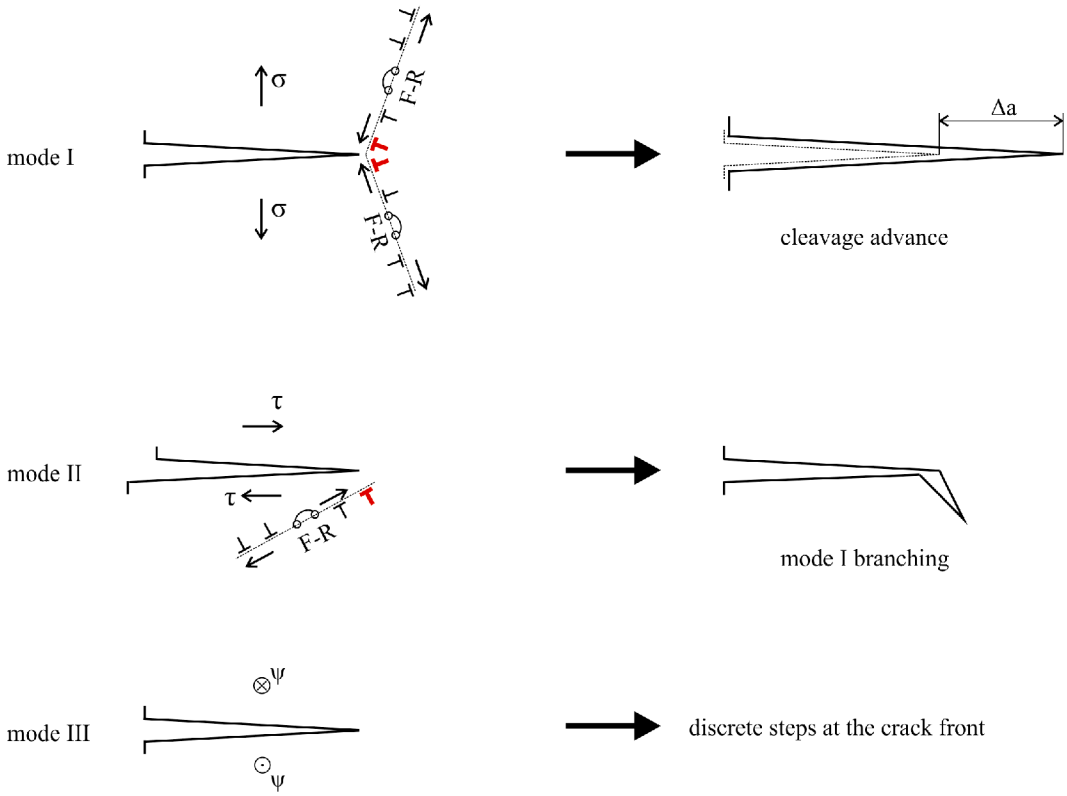

Fig. 4. Decohesion model based on absorption of antishielding dislocations.

Mode II

If the probability of having a slip plane with the external dislocation sources nearly coplanar with the crack plane is low (high angle between slip planes), then, considering the decohesion model, the generated dislocations will not cause a plastic crack tip sliding displacement. Depending on the location of the dislocation source, one part of the generated dislocations will move in front of the crack tip, the other one will move to the crack tip and behind. The dislocations coming very near to the crack tip can generate a local decohesion due to a superposition of their tensile stress field with that of the crack. The most probable crack propagation direction is determined by a maximum tensile component of the crack tip stress field, i.e., by the maximum of local SIF k_{Id}. This is reached when the crack tip deflects out of its plane by a formation of an elementary kink with the angle of 70° – see Fig. 4. Thus, for the mode II loading case, the decohesion model predicts a non-crystallographic crack propagation with a high probability of the crack front deflection to local mode I.

Mode III

During mode III loading no new fracture surface is generated for the same reason as in the deformation model presented in 1.3.1. The explanation of mode III crack growth in the frame of the ideal decohesion model is also not straightforward. Indeed, the mode III cracks do not generate a tensile stress singularity so only the tensile stresses generated by the edge segments of dislocations near the crack flanks can contribute to decohesion. Even in this case, however, the crack front segments locally loaded in mode II can propagate in the same manner as under the pure remote mode II loading [50]. This means that such segments of the mode III crack

front will deflect from the macro crack plane thus receiving a support of the tensile component of crack tip stress field. Such deflections are, however, not as simple as those of the pure mode II crack front and the segments can only locally twist.

1.3.3 Coalescence of Microcracks

A possibility of propagation of coplanar mode II and III cracks according to the damage-based Weertman model, i.e., out of the frame of both deformation and decohesion models, should also be considered. The activity of dislocations in intersecting spatial slip systems with non-zero Schmid factor can lead to a production of vacancies, twins and eventually microcracks inside the cyclic plastic zone ahead of the crack front even in the near-threshold region. The crack propagation then succeeds by interconnection (coalescence) of such created microcracks with the main crack front similarly to the large-scale yielding case. This was observed in molecular-dynamics simulations [21,22] of cracked perfect iron single crystals. In these simulations, the selected crystallographic orientation of crack plane/crack front (110)/[110] completely avoided the production of new fracture surfaces coplanar with the crack plane and connected to the crack front according to the deformation model. The resulting crack paths were spatially micro-tortuous, thus including some contribution of the local mode I loading component. This accumulative damage mechanism leads to comparable growth rates of modes II and III cracks. In real polycrystalline materials such a mechanism must be much less effective than those predicted by the deformation and decohesion models. In spite of this, Tanaka [28] reported a coplanar shear-mode crack growth by microcrack coalescence in carbon steel close to the near-threshold region. This means that, in some metallic materials, a certain contribution of this damage mechanism to fatigue crack growth should not be excluded even in the near-threshold regime.

In summary, mode II and a mode III cracks driven by the deformation induced surface generation should preferentially propagate along the plane of maximum shear stress, i.e., nearly coplanar with the precrack plane, in a crystallographic manner. In the case of the dislocation-induced (or dislocation-supported) decohesion, however, the model predicts a deflection of cracks: the mode II cracks should globally tilt and the mode III ones should locally twist. Both these models predict $(\mathrm{d}a/\mathrm{d}N)_{\mathrm{II}} > (\mathrm{d}a/\mathrm{d}N)_{\mathrm{III}}$ for $\Delta K_{\mathrm{IIeff}} = \Delta K_{\mathrm{IIIeff}}$ and $\Delta K_{\mathrm{IIeff,th}} < \Delta K_{\mathrm{IIIeff,th}}$. Such a difference between mode II and mode III loaded cracks is expected to stand for all metallic materials. The presence of the accumulative damage mechanism can only diminish this difference: the more significant this damage mechanism, the smaller becomes the difference.

1.3.4 Local Mode II Propagation of Remote Mode III Cracks

As already mentioned, a pure mode III crack propagation is much more difficult than the mode II one. The authors of [34,38] suggested that a fatigue crack loaded in mode III can only grow by the support of local modes I and II components. The mechanisms described in Section 1.3 are connected to a crack front in a single crystal. In polycrystalline materials, new fracture surfaces under remote mode III loading can also be generated by local mode II mechanisms. The following two models describe crack propagation in the shear plane.

The model reported in [38] is schematically depicted in Fig. 5(a). In real polycrystalline materials, the crack front is never microscopically straight. Macroscopic mode III crack front

propagation can be produced by displacements in local mode II. Ledges of a tortuous crack front experience non-zero components of mode II loading. The crack propagates by alternating step by step mode II growth (under the resolved shear stress component $\tau_{II,d}$) of the diversely oriented crack front segments. This leads to gradual smoothing of the crack front and may decelerate the remote mode III crack growth. After a certain number of cycles, the shape of the crack front looks similar to a mode III-like crack propagation.

The second model considers even a microscopically straight crack front but the assistance of secondary phase particles is needed here (Fig. 5(b)). Dislocation pile-ups are gradually generated at the particle-matrix interfaces and eventually produce microcracks perpendicularly oriented to the main crack front. These cracks can then extend under the local mode II along the crack front.

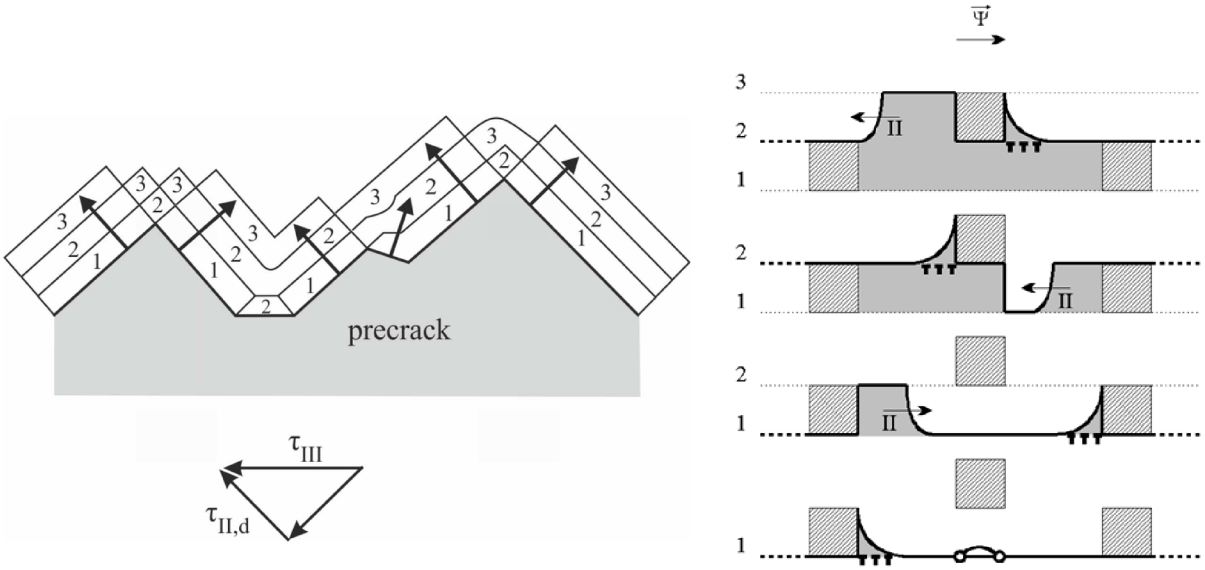

(a) Mode II controlled mechanism of mode III growth from micro-tortuous crack front

(b) Decohesion of the particle –matrix interface (or particle breaking) supported by dislocation pile-ups

Fig. 5. Local mode II crack front propagation along the original mode III front.

1.4 Competition Between Shear and Opening Modes

Mode II and mode III fracture morphologies considerably differ particularly in the near-threshold region [19]. The change in the crack growth direction is related to a competition between shear and opening loading modes that can lead to mode I branching. This phenomenon is mostly observed in both the near-threshold region and the Paris regime while in the high loading ranges, i.e. in the large scale yielding case, the cracks usually propagate in a coplanar manner along the maximum shear plane (e.g. [4,6-8]). Some simple concepts for the description of the mode I branching condition for mode II cracks were also proposed [9,10] but their verification is difficult due to a lack of reliable effective values of $\Delta K_{\mathrm{IIeff}}$. Thus, the interaction between crack sliding and the deviation from the ideal mode II and mode III crack propagation induces inherent difficulties in the analyses of the mode II and mode III fatigue crack growth data. Small semi-elliptical shear cracks, initially growing coplanar with the precrack in remote modes II and III, are often observed to form mode I branches – see Fig. 6.

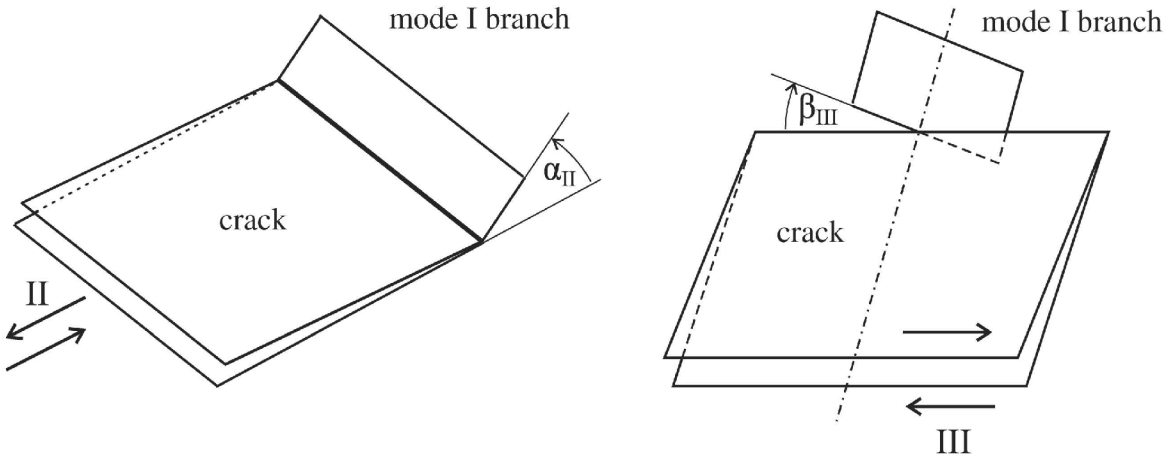

Fig. 6. Schematic illustration of deflected and twisted cracks forming mode I branches under mode II and mode III loading, respectively.

1.4.1 Mode I Branching of Remote Mode II Cracks

According to the criteria based on linear elastic fracture mechanics, the crack should diverge to the direction perpendicular to the maximal principal stress, i.e. to locally grow under mode I loading [31]. The maximum-tangential stress (MTS) criterion is widely used because of its simplicity and agreement with many experiments. The quasi-two-dimensional model in Fig. 6 considers an elementary mode I crack branch subjected to the main crack stress field loading. Local SIFs k_{I} and k_{II} for the imaginary branch can be expressed as follows [31]:

$$k_{\mathrm{I}} = \cos\frac{\alpha_{\mathrm{II}}}{2}\left(K_{\mathrm{I}}\cos^2\frac{\alpha_{\mathrm{II}}}{2} - \frac{3}{2}K_{\mathrm{II}}\sin\alpha_{\mathrm{II}}\right) \tag{2}$$

$$k_{\mathrm{II}} = \frac{1}{2}\cos\frac{\alpha_{\mathrm{II}}}{2}\left[K_{\mathrm{I}}\sin\alpha_{\mathrm{II}} + K_{\mathrm{II}}\left(3\cos\alpha_{\mathrm{II}} - 1\right)\right], \tag{3}$$

where α_{II} is the deflection angle (Fig. 6) and K_{I} and K_{II} are the remote SIFs for the main crack.

The angle α_{II} for the mode I branch under pure remote mode II loading corresponds to $k_{II} = 0$. Considering Eq. (3) and $K_I = 0$, $K_{II} \neq 0$ and $|\alpha_{II}| < 90°$, one obtains

$$k_{II} = \frac{1}{2}\cos\frac{\alpha_{II}}{2} K_{II}\left(3\cos\alpha_{IId} - 1\right) = 0 \tag{4}$$

$$\cos\alpha_{IId} = \frac{1}{3}. \tag{5}$$

This gives the value $\alpha_{IId} = \pm 70.5°$ which determines the direction of the initial crack growth according to the MTS criterion. The corresponding value of k_I for this angle is $k_I = 1.15\,K_{II}$. Therefore, a simple necessary condition for growth of a mode I branch at the crack front loaded in mode II was formulated as follows [3,31,51]: the local stress intensity range Δk_I for the deflected (branched) crack must be greater than the mode I threshold $\Delta K_{I,th}$, i.e.,

$$\Delta k_{Id} = 1.15\ \Delta K_{II} > \Delta K_{I,th}. \tag{6}$$

Some experiments revealed that mode I branch crack formation is preceded by a limited amount of shear dominated crack growth [31,17] or that mode II crack extension was possible until a crack arrest. When the loading was increased and the local Δk_I for an initial branch exceeded the ΔK_I threshold, branching to mode I occurred.

It should be emphasized that the criterion for mode I branching can only be used when considering the effective SIF values. If the effective values are not known it is not possible to evaluate correctly the criterion, which is the reason why different authors observed different thresholds and crack branching behaviour. To the author's knowledge, however, no reliable data of ΔK_{IIeff} in the near-threshold region were reported until 2013, except for an assessment $\Delta K_{IIeff,th} \leq 3.5$ MPa·m$^{1/2}$ in the ferritic-pearlitic steel [14]. Determination of ΔK_{IIeff} for more metallic materials is one of the main contributions of the recent works [50,52] (see herafter).

The interaction of crack flanks during remote mode II loading can induce additional mode I loading which can also contribute to the local mode I crack branch SIF k_I. With this mode I support, the crack can more easily propagate and partially avoid the friction force.

1.4.2 Mode I Branching of Remote Mode III cracks (Factory Roof Formation)

The branching of mode II cracks is relatively easy since the deflected (tilted) plane intersects the main crack plane along a line (or curve). On the other hand, the mode III crack segments under a pure shear can only get an additional mode I support by a twist around the axis perpendicular to the crack front [31] as schematically depicted in Fig. 6. The condition for growth of the elementary mode I branch at the crack front loaded in mode III might be, in principle, similar to that for the crack loaded in mode II: $\Delta k_{It} = \Delta K_{III} > \Delta K_{I,th}$ with the related twist angle $\beta_{IIIc} = 45°$ (e. g. [31] and resulting from Eq. (18) for $\Delta k_{IIIeff,t} = 0$). However, the planes of the twisted element and the main crack intersect just in one point which means that the twisting can occur only on microscopic ledges at the main crack front that are locally loaded under the mixed mode II + III. In particular, the mode I branches at fronts of semi-elliptical surface microcracks loaded in mode II + III initiate at those crack-front elements that potentially get the highest synergy of mixed-mode I + II + III loading in terms of an equivalent SIFR $\sqrt{\Delta K_I^2 + \Delta K_{II}^2 + \left[1/(1-\nu)\right]\Delta K_{III}^2}$ [51]. The related numerical analysis [19,27]

revealed that such elements are located at crack front sites predominantly loaded in mode II. In the notched specimens loaded in torsion, this analysis precisely predicted locations of branches initiating the factory-roof fracture morphology as documented by a stereophotogrammetry of fracture surfaces.

The transition to local mode I represents geometrically difficult combined deflection/twisting of the crack front. Creation of mode I branches occurs at particular sites along mixed-mode II + III fronts of multiple semielliptical surface cracks and starts the formation of factory-roof crack shape [16,53,32]. A 3D image of a factory roof is presented in Fig. 7. The positions of mode I branches are marked at the semi-elliptical crack front segments. After coalescence of these branches, the mode I cracks spread in planes deflected by 45° from the macroscopic maximum shear stress plane. During further growth, the massifs get mutually closer and decrease its height.

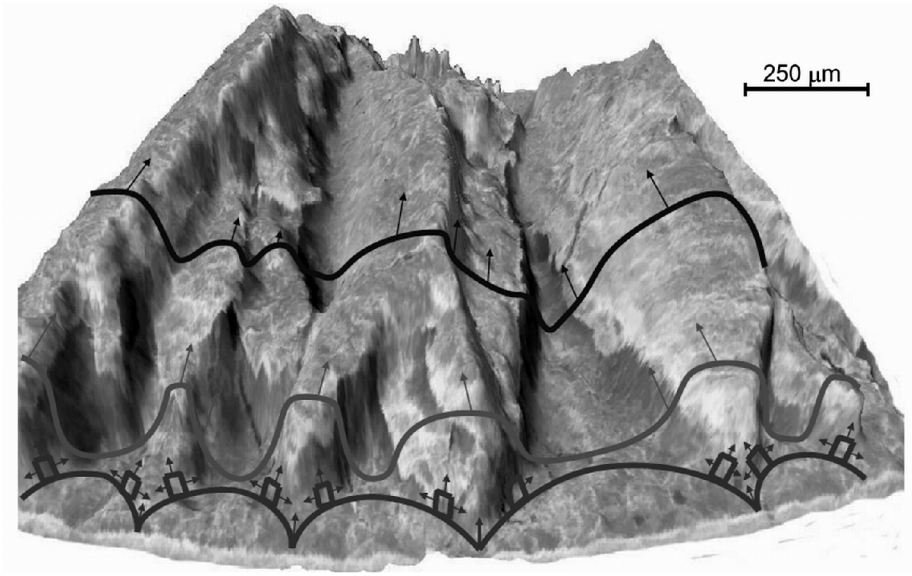

Fig. 7. Example of the factory-roof morphology with highlighted positions of mode I branching [27].

Recently, the role of mode II loaded segments causing instabilities and branching of the planar crack front under the remote mode I + III loading by their local deflections (vanishing of mode II) was confirmed by general theoretical analyses [54,55]. Similarly, the very recent review paper [56] on three-dimensional effects at cracks and sharp notches reports that, near the corner points, modes II and III cannot exist in isolation. For a through-thickness crack in a bar, e.g., the ratio of the induced K_{II}-factor to that of the remote mode III tends to $K_{II,ind}/K_{III} \approx 2$, while the ratio of induced K_{III}-factor to that of the remote mode II tends only to $K_{III,ind}/K_{II} \approx 0.5$. Hence, the creation of mode I branches at crack fronts loaded in a pure mode III is highly improbable and the above mentioned simple branching condition is not useful. In the case of torsion loading, however, the mode III cracks can still get some mode I support just by a deflection from the maximum shear plane. This is why, for a limited number of cycles, the semi-elliptical microcracks often propagate along deflected planes towards the specimen bulk before they bifurcate to factory-roof morphology [38].

1.5 Experimental Data Available in Literature

1.5.1 Mode II

There is an agreement between many authors [31] that the near-threshold cracks under mode II loading usually branch to mode I controlled (or at least supported) crack growth in practically all kinds of steels. Moreover, $\Delta K_{II,th} > \Delta K_{I,th}$ is usually measured although it should be vice versa when taking the results of atomistic models into account [57,58]. The reason for that is a friction-induced shielding of the precrack leading to a decrease of the effective crack driving force ΔK_{IIeff}. The most extended near-threshold coplanar growth was reported by Doquet and Pommier [14] for the ferritic-pearlitic steel to crack lengths in the range of 12 – 450 µm related to the ΔK_{II}-range of 7.5 – 43.0 MPa·m$^{1/2}$ (R = –1). It should be noted, however, that the shear-mode crack growth was associated with many mode I branches along the crack paths which contributed to deceleration and final bifurcation of mode II cracks. In the 0.47% carbon steel (JISS45C), Murakami [59] investigated small mode II cracks emanating from artificial defects. The most frequently observed behaviour was a very short coplanar crack growth that was stopped after 10 µm to create a mode I branch of 70°, although an immediate branching was observed as well. In the same steel, Murakami et al. [32] also measured $\Delta K_{II,th}$ = 10.6 MPa·m$^{1/2}$ by observing the sizes of semi-eliptical mode II + III cracks initiating the factory-roof morphology. In the rail steel, Hellier et al. [12] assessed the remote crack growth threshold as $\Delta K_{II,th} \approx 9$ MPa·m$^{1/2}$ (R = 0). In the weldable structural steel BS4360 50D, Tong et al. [60] reported an immediate transition to mode I branching above $\Delta K_{II,th} \approx 11.5$ MPa·m$^{1/2}$ (R = 0.1). In the maraging steel, Doquet et al. [61] observed an immediate transition to mode I branch below ΔK_{II} = 15 MPa·m$^{1/2}$.

In titanium alloys, Campbell and Ritchie [62] reported that the ratio $\Delta K_{II,th}/\Delta K_{I,th}$ (R = 0.1 – 0.8) for long cracks was also higher than 1. In the case of short cracks, the microstructurally small semi-elliptical (3D) cracks exhibited the smallest $\Delta K_{II,th} \approx 5$ MPa·m$^{1/2}$ due to the biased sampling of microstructurally weak paths and reduced shielding. The through-the-thickness (2D) short cracks exhibited a higher $\Delta K_{II,th}$ but lower than that for the long cracks. For aluminium alloys 2014-T6 and 7075-T6 Merati et al. [63] used the four-point testing method (R = 0.1 – 0.2) with sharply edge-notched square bar specimens. Although some small shear-mode growth was always present before mode I branching, there were only small semi-elliptical cracks in the middle of the specimens in the near-threshold region. $\Delta K_{II,th} \approx 4.5 – 6.0$ MPa·m$^{1/2}$ was measured for the 7075-T6 alloy and $\Delta K_{II,th} \approx 5.0$ MPa·m$^{1/2}$ for the 2014-T6 alloy. Because of the imperfections in the four-point test (see 2.1), the validity of these values should not be overestimated.

1.5.2 Mode III

In the hardened rail steel with a fine pearlitic structure, Hellier et al. [35] observed semi-elliptical cracks with mode I branches started at mode II sites of semi-elliptical cracks, in accordance with the quantitative model [27]. Such a shear-mode growth was a dominant feature of the fracture surface morphology. In some cases, however, parallel arrays of semi-elliptical cracks were found to join up by mode I branches to develop the initial stage of the factory-roof morphology (also in accordance with the model [27]).

The mode III threshold was assessed as $\Delta K_{III,th} \approx 11.6$ MPa·m$^{1/2}$. In the 3.5% NiCrMoV steel, Tong et al. [64] reported $\Delta K_{III,th} \approx 10.1$ MPa·m$^{1/2}$ (R = –1) and $\Delta K_{III,th} \approx 8.1$ MPa·m$^{1/2}$

($R = 0.1$) for a precrack generated in tension, but $\Delta K_{III,th} \approx 6.1$ MPa·m$^{1/2}$ ($R = -1$) for a precrack generated in torsion. In aluminium alloys, Merati et al. [63] determined $\Delta K_{III,th} \approx 6.1$ MPa·m$^{1/2}$ for the 7075-T6 alloy and $\Delta K_{III,th} \approx 3$ MPa·m$^{1/2}$ for the 2014-T6 alloy. Beretta et al. [65] reported $\Delta K_{III,th} \approx 9.2$ MPa·m$^{1/2}$ ($R = -1$) for a gear steel in torsion. Murakami et al. [32] measured $\Delta K_{III,th} = 10.6$ MPa·m$^{1/2}$ ($= \Delta K_{II,th}$) in the 0.47% carbon steel (JISS45C) steel by observing the sizes of semi-elliptical mode II + III cracks initiating the factory-roof morphology. However, the result of such a measurement is doubtful since the size of the semi-elliptical crack in the mode III direction is determined by walls of the factory roof already growing from mode I branches rather than by pure mode III growth [27].

In the stainless steel, Pokluda et al. [66,67] has shown that the sharp factory-roof morphology and the related clamping of crack-wake asperities caused lower crack growth rate under the mode III than that under the mode II, where the cracks propagated along smooth mode I branches. In the AISI 4340 steel, Ritchie et al. [33] measured a very slow crack propagation under mode III in comparison with that under mode I also in the Paris-Erdogan and near-fracture region (relatively smooth mode III fracture surfaces), i.e., $(da/dN)_I >> (da/dN)_{III}$ for $\Delta K_I = \Delta K_{III}$ ($R = -1$). In terms of CTOD it represented $(da/dN)_{III} \approx (0.0005 - 0.002)$ $\Delta CTOD_{III}$ in contrary to both $(da/dN)_I \approx (0.01 - 0.1)$ $\Delta CTOD_I$ and $(da/dN)_{II} \approx (0.1 - 1.0)$ $\Delta CTOD_{II}$. Well developed factory-roof morphology was observed in the near-threshold region.

Some experiments were done on specimens with sharp notches generated by cutting rather than fatigue precracking [62]. Since the precrack geometry influences the roughness-induced crack closure, these flat precracks led to measurement of thresholds closer to the effective ones.

1.5.3 Effective Stress Intensity Factor Data

Stress intensity factors are usually computed for a smooth frictionless crack and do not contain the closure component. Thus, they overestimate the effective crack driving force [17]. Experimental determination of effective SIF values under shear-mode loading is a rather subtle problem which is, most probably, the reason why there are very rare experimental data available in literature. Moreover, the pure modes II and III experiments are difficult to arrange. The effective SIF values are important for several reasons:

- determination of the effective thresholds as a material constant and the lowest (safe) value for structural-integrity assessments,
- determination of the effective thresholds for evaluating conditions to mode I branching,
- evaluation of the efficiency of modes II and III during shear-mode crack growth.

The lowest $\Delta K_{II} = 7.5$ MPa·m$^{1/2}$ ($R = -1$) applied in [14] on the ferritic-pearlitic steel corresponded to $(da/dN)_{II} \approx 5 \cdot 10^{-11}$ m/cycle, i.e., very close to the threshold. Using the digital scanning electron microscope (SEM) image correlation and elasto-plastic finite element analyses (FEA), the related effective SIF was assessed as $\Delta K_{IIeff} \approx 3.5$ MPa·m$^{1/2}$.

Tschegg [7,8] reported a method of assessment of effective values $\Delta K_{III,eff}$ during the crack growth rate within the Paris-Erdogan and near-fracture regime in the AISI 4340 and mild steels. This method consists in an extrapolation of $(da/dN)_{III}$ values to the zero-length cracks

under various levels of remote ΔK_{III} with superimposed mode I static loading. Such obtained $(da/dN)_{III}$ vs. ΔK_{IIIeff} plot lies even above that of $(da/dN)_{I}$ vs. ΔK_{I}. However, the ΔK_{I} data were not corrected with respect to crack closure and the extrapolation to zero-length cracks might include the small-crack effect, i.e., higher $(da/dN)_{III}$ values in comparison with those for long cracks.

One should note, however, that the effective thresholds $\Delta K_{IIeff,th}$ and $\Delta K_{IIIeff,th}$ were not directly experimentally determined before this Ph.D. work. Such measurements for ARMCO iron, α-titanium, nickel and austenitic steel are presented in the following chapters that include description of the experimental results obtained by using a special technique for precrack preparation and two different experimental arrangements for each of modes II and III tests.

2 Experimental Procedures

2.1 Overview of Experimental Arrangments Used in Shear-mode Cracks Research

A variety of specimens and testing procedures were employed during the research on propagation of shear-mode cracks – see Fig. 8. Specimens for mixed modes I + II and II +III in Fig. 8(a),(c) were used in some earlier experiments [68]. The tubular specimen for mode II under torsion loading in Fig. 8(d) and the centrally edge-notch bar of square cross-section for mixed-mode II + III loading in Fig. 8(b), arranged for a four-point bend test as proposed by Chell and Girvan [69], have been permanently utilized for many years [5,14,70].

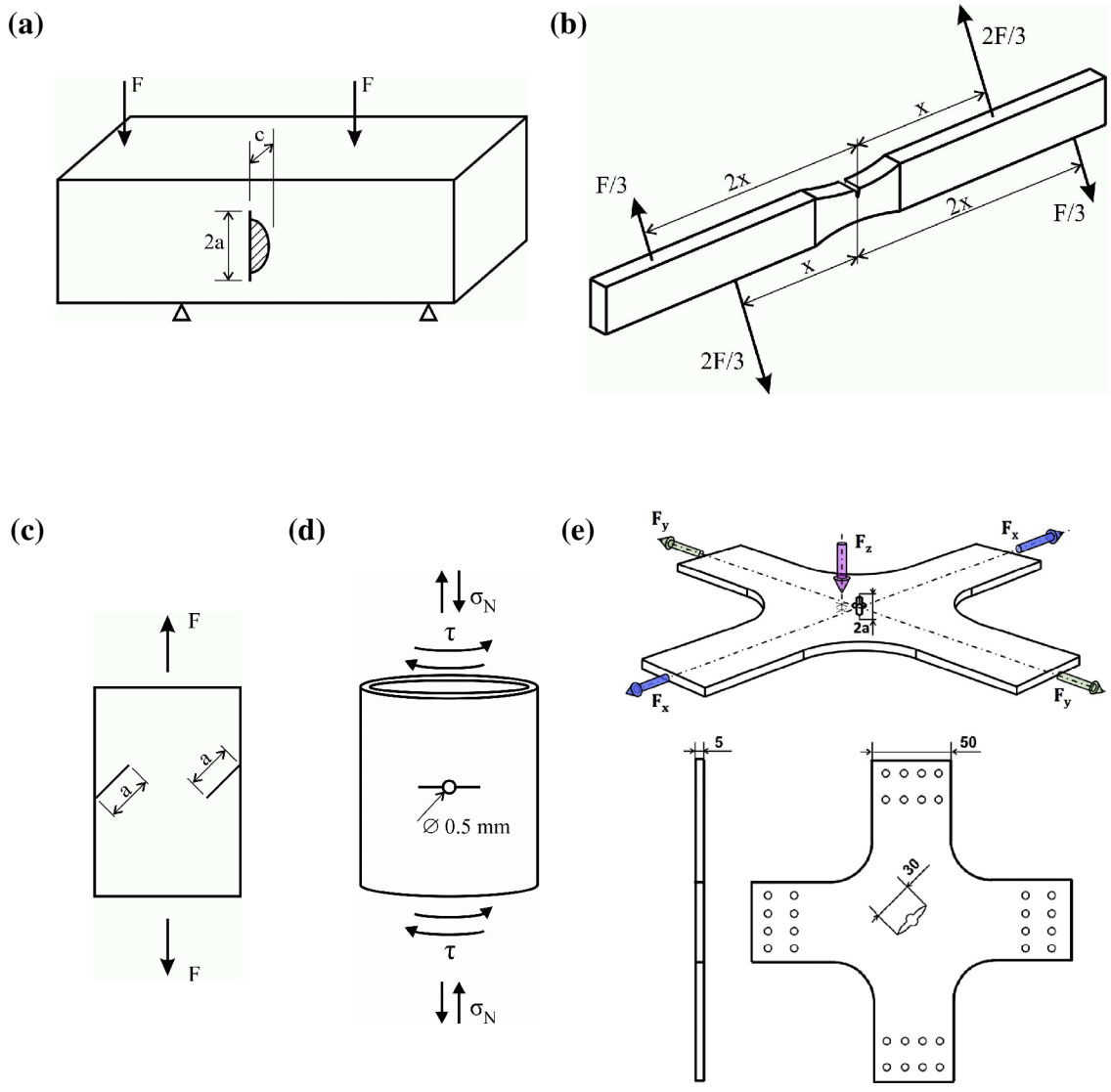

Fig. 8 Experimental arrangements used in shear-mode crack growth tests. (a) four-point bending specimen with semi-circular surface crack for mixed mode II + III loading; (b) four-point bending specimen with rectangular surface crack for mixed-mode II + III loading; (c) edge-cracked specimen for mixed mode I+II loading; (d) tubular specimen for mode II loading; (e) cruciform specimen for mixed mode I + II + III loading [71].

In the latter specimen, the relative proportions of mode II and mode III may be varied by rotating the test-piece about its longitudinal axis. As found out by Doquet et al. [17], however, a pure modes II and III loading can be achieved only in its very middle section and, consequently, the relevancy of results has to be analysed based on the local values of ΔK_{II} and ΔK_{III} issued from a 3D finite element computation taking the crack front shape into account. A new device for non-proportional I + II + III loading of centrally cracked cruciform specimen was introduced recently (Fig. 8(c)) [71]. The CTS specimen for mixed-mode I + II loading and the circumferentially-notched cylindrical specimen for torsion loading (mode III) are also widely employed in experiments and related finite element analyses (FEA) hitherto [28,33,72,73]. The last two mentioned arrangements were also used in this work and they are mentioned in Sections 2.2 and 2.3 in more detail along with a new testing device described in 2.4.

2.2 Compact-tension Shear Specimens (Mode II)

A standard device for mode I + II testing was used for pure mode II loading of compact tension-shear (CTS) specimens (Fig. 9). The SIFs were calculated using the numerically determined formulas (7) and (8) for the CTS specimens [74]:

$$K_I = \frac{F}{wt}\sqrt{\pi a}\frac{\cos\psi}{1-\frac{a}{w}}\sqrt{\frac{0.26+2.85\frac{a}{w-a}}{1+0.55\frac{a}{w-a}-0.08\left(\frac{a}{w-a}\right)^2}} \tag{7}$$

$$K_{II} = \frac{F}{wt}\sqrt{\pi a}\frac{\sin\psi}{1-\frac{a}{w}}\sqrt{\frac{-0.23+1.40\frac{a}{w-a}}{1-0.67\frac{a}{w-a}+2.08\left(\frac{a}{w-a}\right)^2}} \quad . \tag{8}$$

Here, F is the applied force, W is the specimen width, t is the specimen thickness, $\psi = 0°$ for pure mode I and $\psi = 90°$ for pure mode II, $a = l_{\mathrm{n2}} + l_{\mathrm{o}} + l_{\mathrm{s}}/2$ is the total crack length, $l_{\mathrm{n2}} = 21$ mm is the notch depth, l_{o} is the mode I precrack length and $l_{\mathrm{s}}/2$ is a half of the mode II crack length. The values given by this formula are in accordance with the graphically expressed values in [72]. The Eq. (7) for K_{I} was used during generation of precracks.

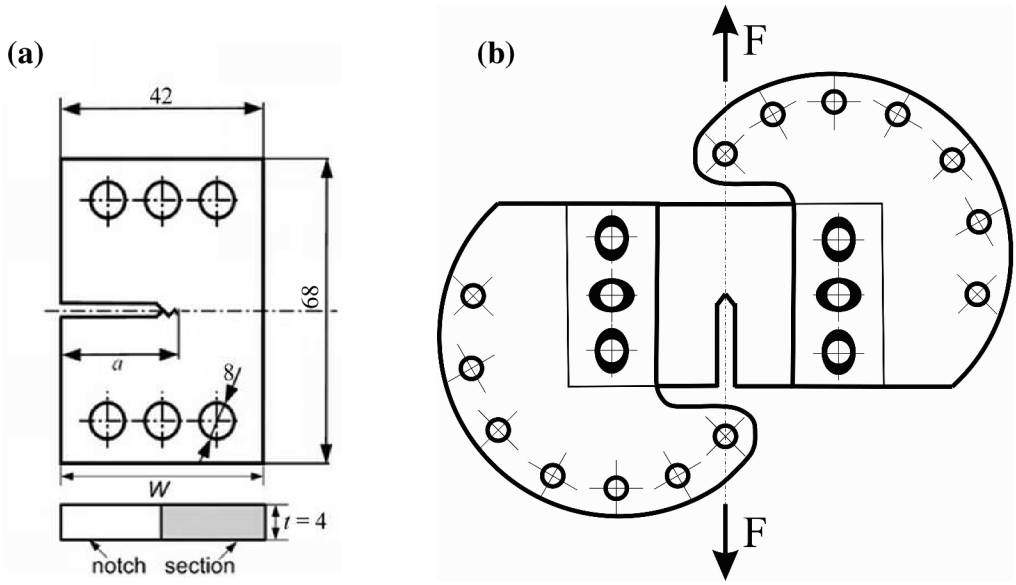

Fig. 9. Mode II experiment scheme: (a) compact tension shear (CTS) specimen; (b) scheme of the loading device [75].

2.3 Cylindrical Specimens Loaded in Torsion (Mode III)

Pure mode III experiments were conducted by means of a special device transforming tensile or compressive force to torsion loading of a cracked cylindrical specimen (Fig. 11) with the same geometry as in the pure shear experiment (Fig. 12). The specimens were fixed into this device by ring clamping elements and loaded by cyclic torque T. The SIFs were calculated according to equation (9)

$$K_{\mathrm{III}} = \frac{16T}{\pi D^3}\sqrt{\pi a}\cdot Y_{\mathrm{III}}, \tag{9}$$

where $a = l_{\mathrm{n1}} + l_{\mathrm{o}} + l_{\mathrm{s}}/2$ is the total crack length, $l_{\mathrm{n1}} = 6.5$ mm is the notch depth and Y_{III} is the factor of geometry, which was derived from the asymptotic relationship (10) published in [76]:

$$\tau_{\theta z} \to Y_{\mathrm{BK}} \frac{2T}{\pi\left(\frac{d}{2}\right)^3}\left(\frac{ad}{D}\right)^{\frac{1}{2}}\frac{1}{\sqrt{2r}}, \tag{10}$$

where $Y_{\mathrm{BK}} = 1+\frac{1}{2}\xi+\frac{3}{8}\xi^2+\frac{5}{16}\xi^3+\frac{35}{128}\xi^4+0.208\xi^5$ is a dimensionless factor introduced by Benthem and Koiter in [76] and $\xi = \frac{d}{D}$. After adaptation and using the definition of stress intensity factor it gives:

$$\tau_{\theta z} \to Y_{\mathrm{BK}} \frac{16T}{\pi d^3}\left(\frac{d}{D}\right)^{\frac{1}{2}}\frac{\sqrt{\pi a}}{\sqrt{2\pi r}},$$

$$K_{\text{III}} = \frac{16T}{\pi d^3}\sqrt{\pi a}\left(\frac{d}{D}\right)^{\frac{1}{2}} Y_{\text{BK}},$$

$$Y_{\text{III}} = \left(\frac{d}{D}\right)^{-\frac{5}{2}} Y_{\text{BK}} = \xi^{-\frac{5}{2}}\left(1+\frac{1}{2}\xi+\frac{3}{8}\xi^2+\frac{5}{16}\xi^3+\frac{35}{128}\xi^4+0.208\xi^5\right) \qquad (11)$$

The accuracy of this formula was analyzed in terms of FEM in [77] and the error was found to be less than 1% (see Fig. 10).

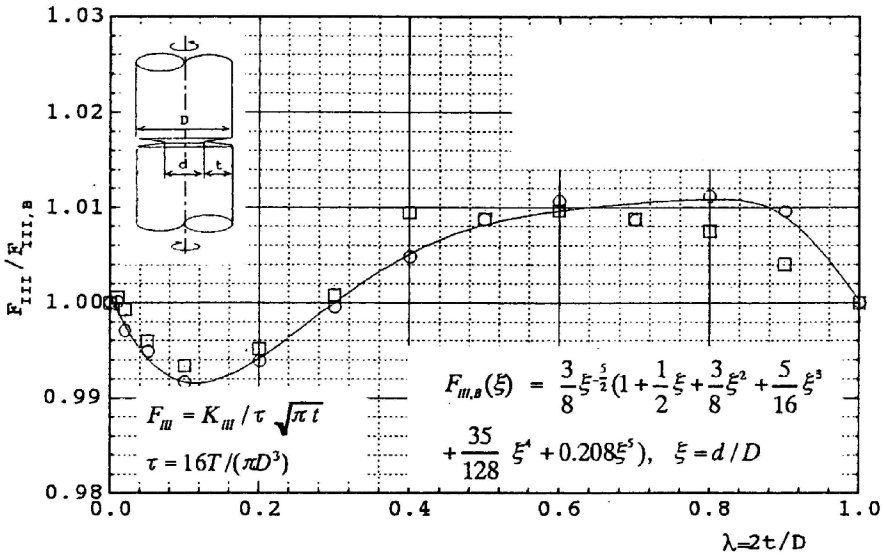

Fig. 10. Accuracy of the asymptotic solution of the SIF in mode III from [76], here denoted $F_{\text{III,B}}$. The circle and square points correspond to the results of numerical analysis [77].

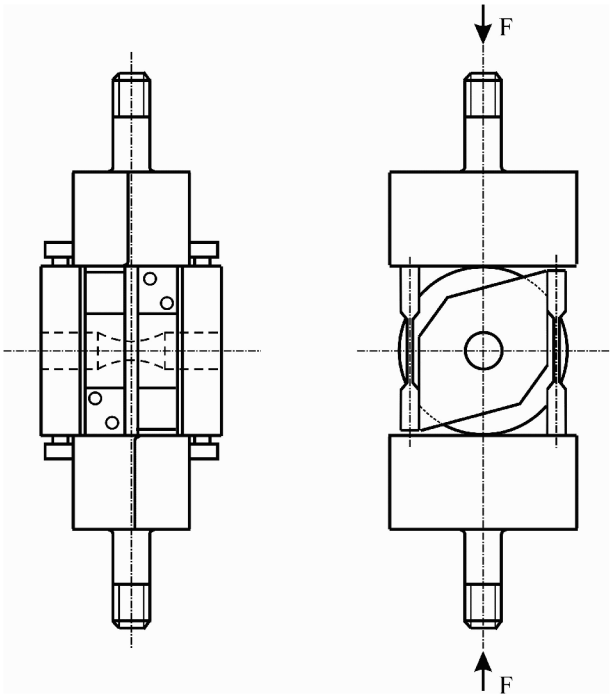

Fig. 11. Device for torsion loading of cylindrical specimens.

2.4 Cylindrical Specimens Loaded by Pure Shear (Mode II + III)

To load a single specimen simultaneously by remote mode II, mode III and mixed mode II + III, a special testing device was utilized [16,50]. The device transforms tensile forces to a simple-shear loading of circumferentially notched cylindrical bars with the inner diameter $d = 12$ mm and the outer diameter $D = 25$ mm (Fig. 12). At the exact central point of the bar the bending moment was zero when considering ideal testing conditions and, therefore, no superposition of mode I was present. The circumferential crack was subjected to cyclic shear loading that resulted in various combinations of modes II and III (Fig. 12(c) as a function of the polar angle φ. At the top and the bottom of the circular cross-section the crack was loaded in a pure mode II, on the left and right in a pure mode III and, in between, a mixed-mode II + III loading was applied.

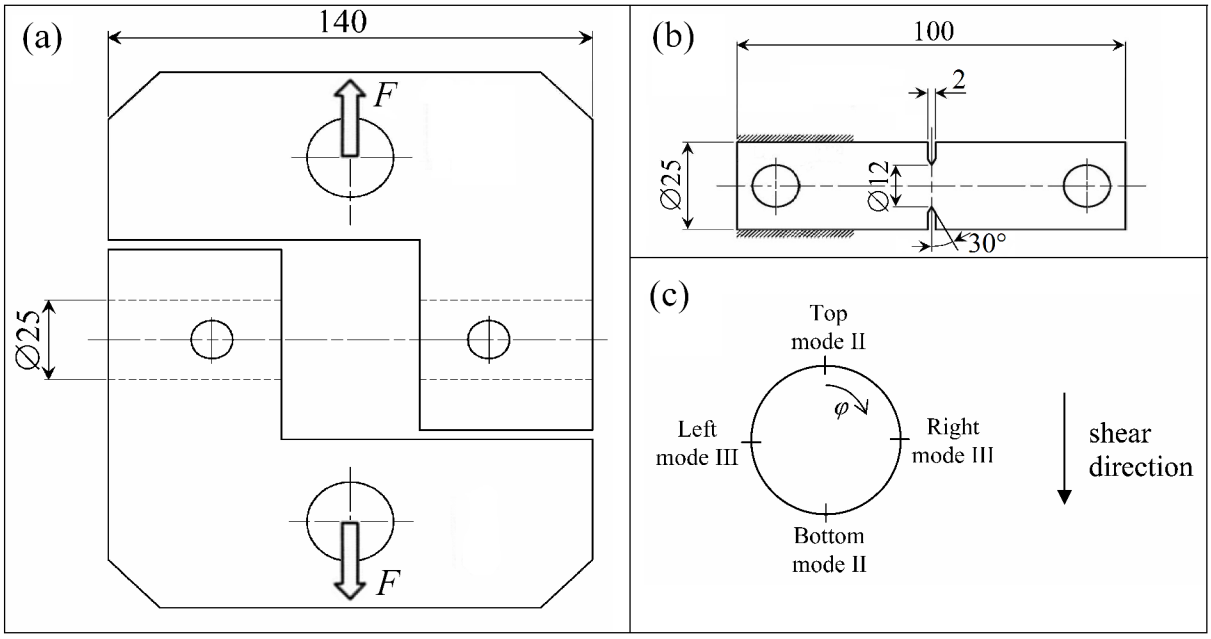

Fig. 12. Scheme of the experiment with cylindrical specimens loaded in pure shear: (a) loading device; (b) pure shear specimen; (c) specimen cross section with the corresponding loading modes.

The precracks started at the notch of the depth $l_{n1} = 6.5$ mm and reached the length l_o. The lengths l_o and the shear-crack length l_s were measured on SEM images of fracture surfaces (see Fig. 18). The dependences of modes II and III SIFs (see Eq. (12)) on both the fatigue crack length $l_o + l_s/2$ and the angle φ were calculated using FEM [78,79]. Details of the FEM model and the K-calibration procedure based on J-integral are described in [79]. In this approach, the ANSYS model (with one sub-model) reported in [78] was refined by an additional second sub-model to obtain particularly precise K-values around the circumferential precrack. Based on these results, dimensionless geometrical factors Y_{II}, Y_{III} were evaluated using a power regression function and plotted in Fig. 13. An example of the K_{II} and K_{III} dependences on the angle φ is presented as the polar diagram in Fig. 14. The K-values were utilized for the experimental determination of crack-growth rate curves $\Delta a/\Delta N$ vs. ΔK under modes II and III loading.

$$K_{\mathrm{J}} = \frac{4F}{\pi D^2}\sqrt{\pi a}\cdot Y_{\mathrm{J}}; \quad \mathrm{J} = \mathrm{II},\mathrm{III} \tag{12}$$

$$Y_{\mathrm{II}} = 27.7861\cdot(l_{\mathrm{o}} + l_{\mathrm{s}}/2)^{0.388981}$$

$$Y_{\mathrm{III}} = 8.15575\cdot(l_{\mathrm{o}} + l_{\mathrm{s}}/2)^{0.173354}$$

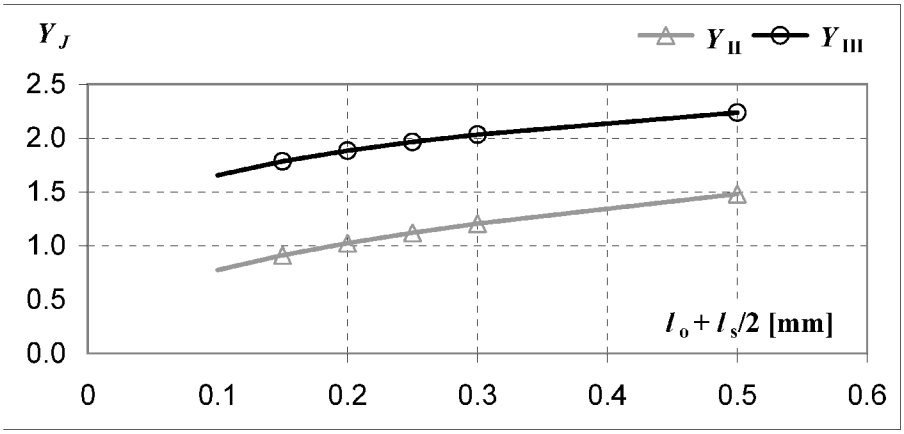

Fig. 13. Geometrical factors Y_{II}, Y_{III} as functions of fatigue crack length $l_{\mathrm{o}} + l_{\mathrm{s}}/2$ for the notched cylindrical pure shear specimen.

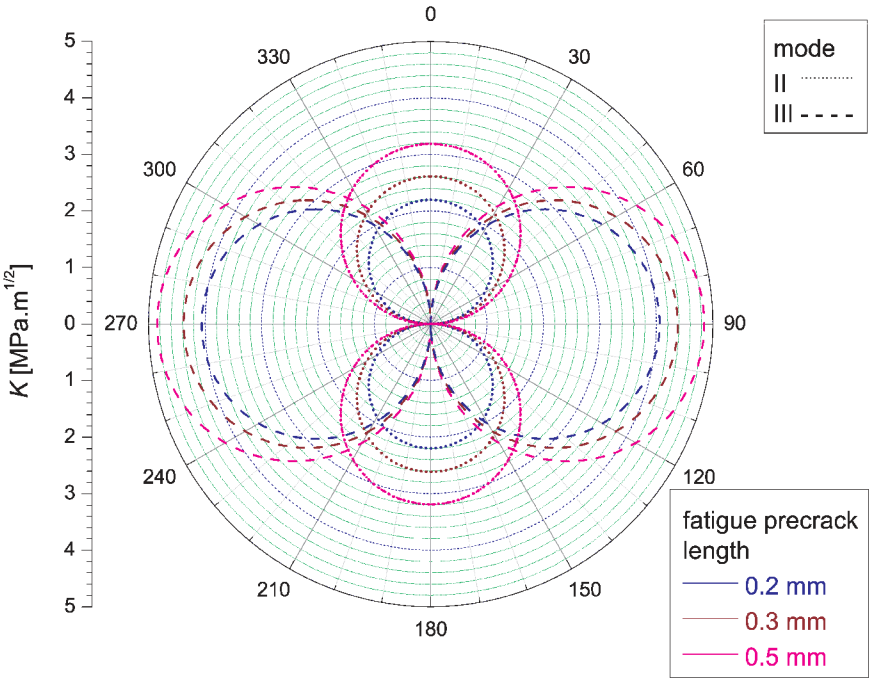

Fig. 14. Example of K_{II} and K_{III} dependences on the angle φ for various fatigue crack lengths $l_{\mathrm{o}} + l_{\mathrm{s}}/2$ and the loading force of 7355 N for the notched cylindrical pure shear specimen.

The dependence in Fig. 13 given by Eq. (12) covers the notch effect which causes a decreasing of the geometry factor to 0 when approaching the notch root. This effect, however, is not covered by Eqs. (8) and (9) for the CTS specimens and the torsion specimens. In this case the precrack length should be higher than a certain minimum estimated in [82]. Fig. 15(a) shows schematically a precrack of length l_o growing from a notch of length l_n and radius ρ. Fig. 15(b) shows the stress intensity factor K as a function of l_o. The dashed curve is the result of a numerical calculation. The two solid lines are the approximations for $l_o << \rho$:

$$K_s \approx 1.12\, k_t\, \sigma \sqrt{\pi\, l_o}\ ,$$

for short-length precrack, where k_t is the elastic stress concentration factor and σ the nominal stress, and for $l_o > \rho$:

$$K \approx \sigma \sqrt{\pi (\, l_n + l_o)} \cdot Y\ ,$$

where Y is a factor of geometry. The intersection between these two approximation lies near $l = \rho/4$ or even lower. Notches of the CTS and torsion specimens had the radius $\rho \approx 150$ μm. The precrack length, therefore, should be $l_o > 35$ μm, which was fulfilled for all specimens and the Eqs. (8) and (9) ensure correct values.

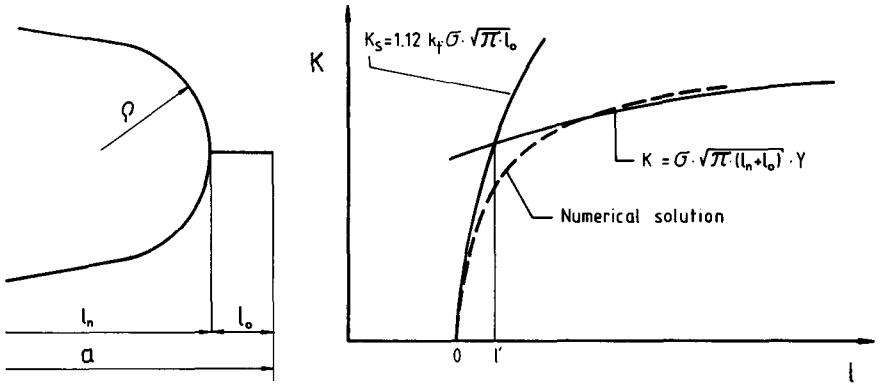

Fig. 15. (a) crack emanating from a notch; (b) schematic illustration of the stress intensity factor as a function of the precrack length l_o.

It should be mentioned that in some torsion specimens the precrack length was not symmetric around the circular cross section. In this case the lengths were averaged when calculating the shape factor Y_{III}. The local precrack lengths were taken into account only in the term $\sqrt{\pi a}$.

2.5 Investigated Materials

Experiments were done with four different single-phase metallic materials of various crystal lattices. Their simple structure enables to a certain extent application of the theoretical models described in Section 1.3. The first material was ARMCO iron, a representative of body-centred cubic (bcc) metals. It is a nearly pure polycrystalline ferrite with the chemical composition as follows (wt%): C 0.009, Mn 0.06, P 0.009, S 0.007 and Fe (the rest). It was received in a cold-rolled state and after annealing, it had the yield strength $\sigma_y \approx 150$ MPa and the mean grain size $d_m \approx 110$ μm (see Fig. 16(a)).

The commercially pure polycrystalline α-titanium (99.5 % Ti) was investigated as a representative of metals with the hexagonal close-packed (hcp) lattice. Two different microstructures of this material were prepared by applying annealing temperatures of 850 °C ($\sigma_y \approx 180$ MPa, $d_m \approx 50$ μm) and 950 °C ($\sigma_y \approx 230$ MPa, $d_m \approx 1$ μm), see Fig. 16(c), (d). The latter microstructure (denoted Ti-needles) contained fine needle-shaped grains of a preferential crystallographic orientation with the mean spacing of about 10 μm.

Two materials with the face-centered cubic (fcc) lattice were also selected. The first was a cold-rolled austenitic steel X5CrNi18-10 with the chemical composition (wt%): C 0.03, Si 1.00, Mn 2.00, Cr 17.00-19.50, Ni 8.50-11.50, N 0.12-0.22, Fe (the rest) and the yield strength after annealing $\sigma_y \approx 230$ MPa. The microstructure can be seen in Fig. 16(b). The austenitic steel has a low stacking fault energy (SFE) and, therefore, another fcc material with a high SFE was selected – commercially pure nickel 201 (99.5% Ni) that had the yield strength $\sigma_y \approx 140$ MPa after annealing. The microstructure is depicted in Fig. 16(e). Some of the mechanical materials characteristics are presented in Table 1.

Table 1. Overview of structures of investigated materials (bcc – body-centred cubic lattice, hcp – hexagonal close-packed lattice, fcc – face-centred cubic lattice, SFE – stacking fault energy).

	ARMCO	Titanium, 850°C	Titanium, 950°C	Nickel	Austenitic steel
Structure	bcc	hcp	hcp	fcc high SFE	fcc low SFE
0.2%-offset yield strength	150 MPa	180 MPa	230 MPa	140 MPa	230 MPa
Mean grain size	110 μm	70 μm	10 μm	45 μm	30 μm

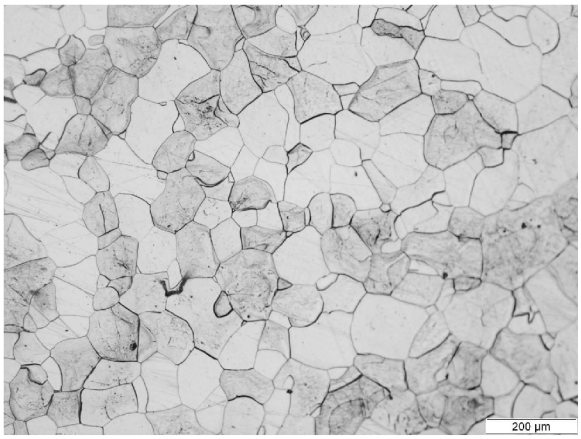

(a) ARMCO iron, $d_m \approx 110$ µm

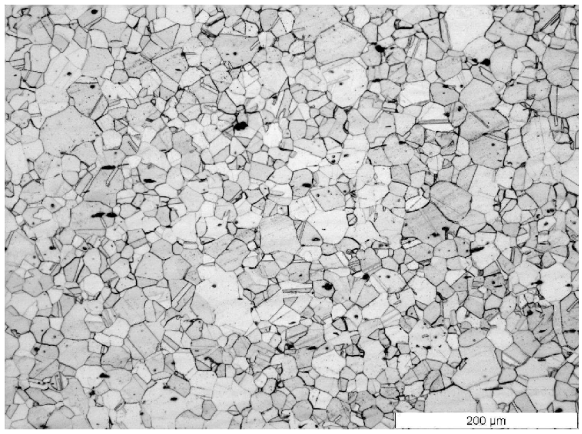

(b) austenitic steel, $d_m \approx 30$ µm

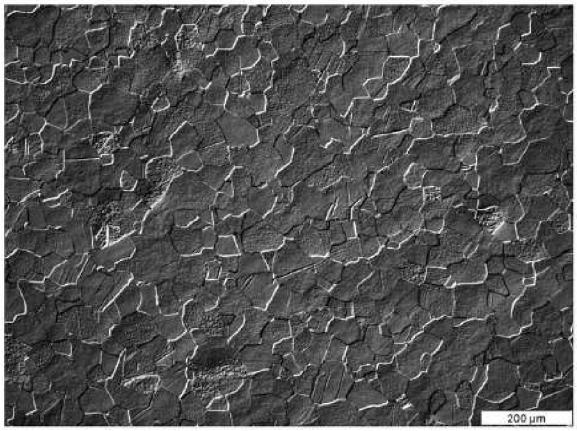

(c) titanium, annealed at 850°C, $d_m \approx 70$ µm

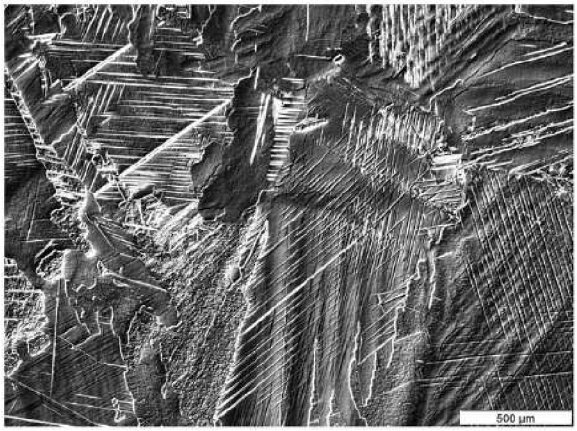

(d) titanium, annealed at 950°C, primary grain size ≈ 1 mm, microstructure parameter ≈ 10 µm

(e) nickel, $d_m \approx 45$ µm

Fig. 16. Etched metallographical samples of the investigated materials.

2.6 Details of the Experimental Procedure

In order to determine the effective thresholds $\Delta K_{\mathrm{IIeff,th}}$ and $\Delta K_{\mathrm{IIIeff,th}}$ the mode II and mode III fatigue cracks should start to propagate from a nearly perfect precrack, which means no contact of the precrack flanks and a plane precrack with a sharp crack front. These requirements were mostly fulfilled by applying a special technique of pre-fatigue loading and heat treatment. The whole experimental procedure consisted of the following steps:

- machining of the specimens with a notch
- sharpening of the notch by a razor-blade polishing, surface polishing of the CTS specimens
- pre-fatigue loading under mode I in compression
- cleaning in ultrasonic bath
- annealing and cooling down in vacuum
- shear-mode fatigue loading
- drilling of holes for final fracture (cylindrical specimens)
- final fracture of the specimen under mode I fatigue loading or in liquid nitrogen
- observation in SEM, creation of stereo-pair images
- 3D reconstruction of fracture surfaces, quantitative fractographical analysis
- metallographical analysis

2.6.1 Pre-fatigue Loading in Mode I

Fatigue precracks were generated under pure cyclic compression at the notch root of all specimens. The applied technique was similar to the experiments performed to investigate the effective mode I threshold and study the formation of crack closure during propagation of a crack subjected to mode I loading [50,80,81,82]. In this way, the crack closure effects could be substantially suppressed at the onset of the experiment. The cyclic compression loading was in the range of $\Delta K_{\mathrm{I}} = 20 \div 25$ MPa·m$^{1/2}$ depending on material and the cyclic ratio was $R = 20$. The precracks reached the length $l_{\mathrm{o}} = 100 \div 500$ μm before they stopped due to a decrease of the effective opening-mode loading. The SIF in mode I for cylindrical (torsion and simple-shear) specimens was calculated using formula (13) found in [83].

$$K_{\mathrm{I}} = \frac{4F_{\mathrm{c}}}{\pi D^2}\sqrt{\pi a}\cdot Y_{\mathrm{I}} \tag{13}$$

where F_{c} is the compressing force and Y_{I} is the geometrical factor defined as follows:

$$Y_{\mathrm{I}} = \frac{1}{2}\xi^{-\frac{3}{2}}\left(1+\frac{1}{2}\xi+\frac{3}{8}\xi^2-0.363\xi^3+0.731\xi^4\right)\cdot\left[1+0.1\cdot\left(2\frac{a}{D}\right)^{\frac{1}{2}}\left(1-2\frac{a}{D}\right)^2\right];\quad \xi=\frac{d}{D}.$$

The flanks of such created cracks remained open after unloading (see Fig. 17) and their relatively planar geometry with a fairly smooth crack front reduced the roughness-induced crack closure effects at the beginning of the experiment. Therefore, the measured values of ΔK_{IIth} and $\Delta K_{\mathrm{IIIth}}$ could be considered to be very close to the effective ones.

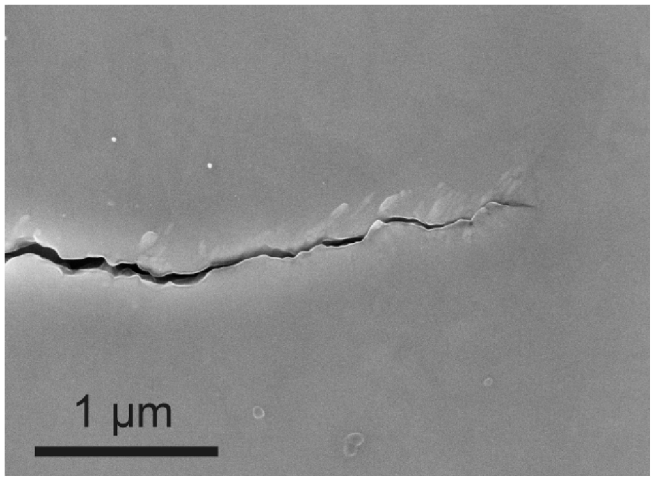

Fig. 17. Opening of the precrack after cyclic compression loading.

2.6.2 Heat Treatment

After pre-fatigue loading, the specimens were annealed to recrystallize in order to avoid any effect of pre-fatigue and hardening of the material, i.e. to eliminate residual stresses and plastic zone at the crack front. It also caused a further smoothening of the precrack facets resulting in even more eliminated roughness-induced crack closure. Annealing and cooling down of the specimens were done in vacuum to avoid generation of oxide layer at the precrack surfaces and the related oxide-induced crack closure effect. The annealing temperature and dwell time for each material is summarized in Table 2. The heating rate was 10°C/min.

Table 2. Annealing temperature of specimens of the investigated materials.

	ARMCO	Titanium	Nickel	Austenitic steel
Annealing T [°C]	950	850 and 950	700	900
Dwell time [min]	90	90	60	90

2.6.3 Experimental Conditions and Parameters

The number of shear-mode loading cycles was usually $N = 10^5$ and the cyclic stress-ratio was $R = 0.1$. Tests with CTS specimens and simple-shear specimens were done on a servo-hydraulic fatigue testing machine (Zwick) at the cycling frequency of 10 or 15 Hz and the torsion experiments were done on a resonance fatigue testing machine (Rumul) at the cycling frequency of 100 Hz. All experiments were performed at room temperature. After the shear-mode experiments, the specimens were fractured by cyclic fatigue loading in mode I and some of the ARMCO iron specimens were fractured monotonically in liquid nitrogen.

2.6.4 Measurement of SIFs and Crack Growth Rates

The obtained SEM images of fracture surfaces enabled measurement of the precrack length l_o, starting at the notch root, and of the shear-mode crack length l_s, depicted in Fig. 18. It should be noted that l_o and l_s are not real crack lengths but their vertical projections.

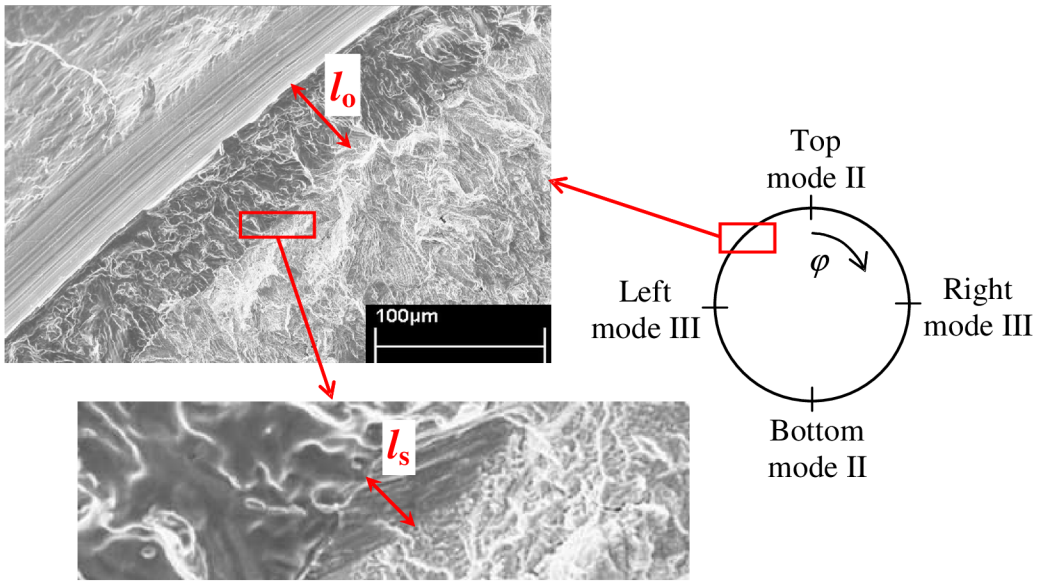

Fig. 18. Measurement of precrack length l_o and shear-mode crack length l_s in the SEM image of fracture surface [84].

The precrack lengths l_o and $l_s/2$ were utilized for calculation of SIFs (after the experiments) according to Eqs. (8), (9) and (12). The shear-mode crack lengths l_s were used for calculation of the crack growth rate $\Delta a/\Delta N$, where $\Delta a = l_s$ and ΔN is the total number of loading cycles of a specimen. The values $\Delta a/\Delta N$ representing averaged crack growth rates were plotted for each material and each of loading modes II and III as diagrams $\Delta a/\Delta N$ vs. ΔK in Fig. 21 in Chapter 3.

2.7 Quantitative Fractography

The crack paths and topography were studied by means of three dimensional reconstruction of the fracture surfaces using stereophotogrammetry in the scanning electron microscope (SEM). This method uses two images of the analyzed region taken from different angles of view to build so-called stereopair (Fig. 19). Additional parameters characterizing the projection enter the algorithm that was processed in the software package Alicona MeX™. An SEM equipped with eucentric holder was employed and the stereopair was obtained by tilting the specimen in the microscope chamber by an angle 5, 6 or 10 degrees depending on the local roughness of the surface. The stereopair was processed via a matching algorithm in order to find corresponding points on both images (homologous points) and the relative z-coordinates of these points were calculated. The 3D model of the depicted surface area usually consisted of 10 – 20 thousand non-equidistant points and so called Delaunay triangulation had to be performed [85,86].

After the 3D reconstruction of the fracture surfaces, measurements by means of the profile analysis were done to determine local deflection and twisting angles of the crack with respect to the remote shear direction (results are in 3.2).

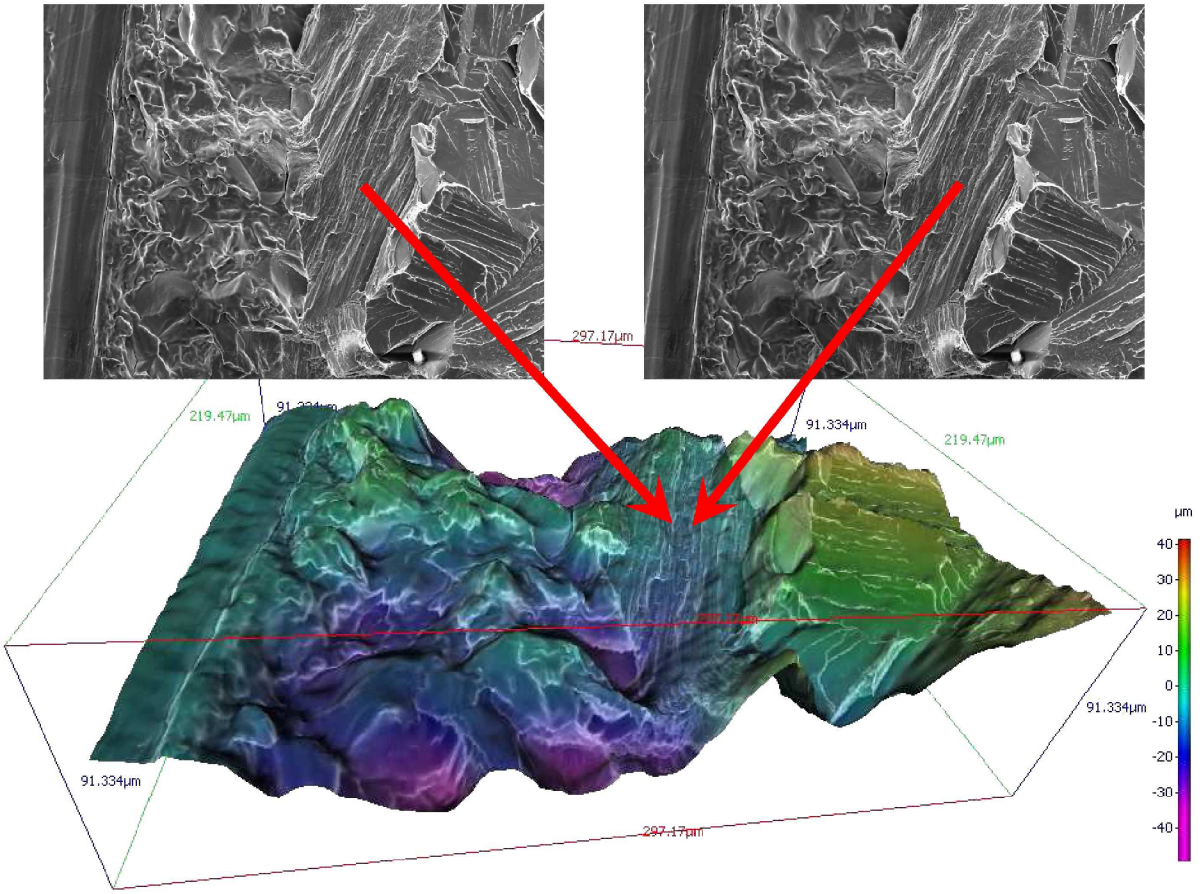

Fig. 19. Example of a three-dimensional reconstruction of a fracture surface using the stereophotogrammetry in SEM [67].

2.8 Size of the Plastic Zone

Elasto-plastic analysis of the crack tip stress-strain field was performed by Horníková et al. [87] for the simple shear specimen presented in 2.4 made of the ARMCO iron. The results showed that loading in the near-threshold region meets the condition of small-scale yielding $a > 20r_p$, where a is the total crack length of 6.7 mm. For levels of loading higher than $2\Delta K_{th}$ (see results in Section 3.3) this condition was not fulfilled when considering the static plastic zone r_p defined as a size of the region where plastic strain intensity

$$\varepsilon_{INT} = \frac{\max\left(|\varepsilon_1 - \varepsilon_2|, |\varepsilon_2 - \varepsilon_3|, |\varepsilon_3 - \varepsilon_1|\right)}{1 + \nu} \tag{14}$$

expressed in terms of the principal plastic strains ε_1, ε_2 and ε_3, is higher than 0.2 %.

However, one should emphasize that the cyclic plastic zone is relevant for fatigue crack growth instead of the static one. For the cyclic ratio $R = 0$ (close to the ratio $R = 0.1$ used in experiments), the cyclic plastic zone size is $r_{cp} = 0.25 r_p$. This means that practically all values of loading used in experiments lie within the small-scale region and can be described in terms of ΔK_{II} or ΔK_{III}. This is also the reason why all experimental data $(\Delta a/\Delta N)_{II,III}$ vs. $\Delta K_{II,III}$ (Section 3.1), obtained by means of three different kinds of cracked specimens, lay practically on an identical curve.

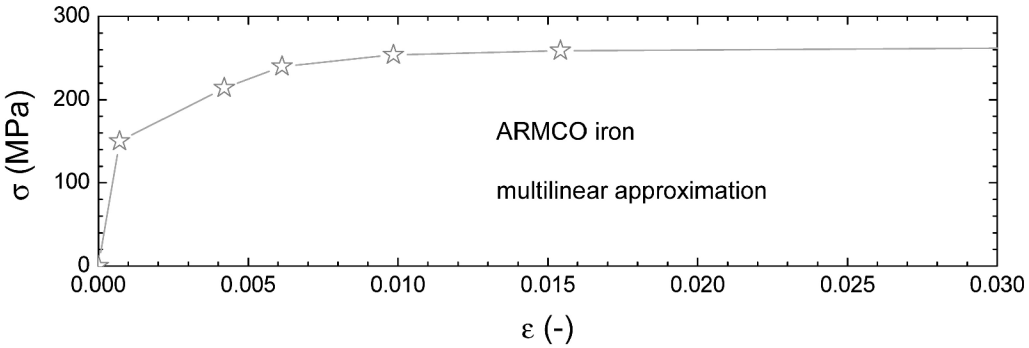

Fig. 20. The multi-linear approximation of the cyclic stress-strain curve for ARMCO iron used in the ANSYS code [87].

3 Results and Discussions

3.1 Crack Growth Rates

The near-threshold crack growth rate data obtained for all investigated materials were plotted as diagrams $\Delta a/\Delta N$ vs. ΔK_{II} in Fig. 21. The values $\Delta a/\Delta N$ were determined as averaged crack growth rates of the shear-mode cracks during $\Delta N = 10^5$ cycles when the crack growth rate was gradually decreasing due to an increasing friction-induced crack closure. In all experiments, the related ratio $\Delta a/a \approx 0.01$ was very small and the corresponding changes of ΔK during the shear-mode crack growth could, therefore, be considered to be negligible.

These crack growth data were fitted using the equation $\Delta a/\Delta N = A(\Delta K^n - \Delta K_{th}^n)$ suitable for the near-threshold region [88]. The data corresponding to the absence of crack growth (below the threshold) are assigned to $\Delta a/\Delta N = 10^{-13}$ m/cycle. The data for the two α-titanium microstructures are not distinguished here since they lie in the same narrow band. With regard to an expected high scatter near the threshold, the data obtained using single-shear and CTS specimens are in a good agreement and the effective threshold values, $\Delta K_{IIeff,th}$, could be determined with a reasonable precision. These values are displayed in Table 6 for all investigated materials.

In general, a rather high scatter of $\Delta a/\Delta N$ values was observed, especially in the near-threshold region. The data obtained using single-shear and CTS specimens in mode II and simple-shear and torsion specimens in mode III are in a good agreement.

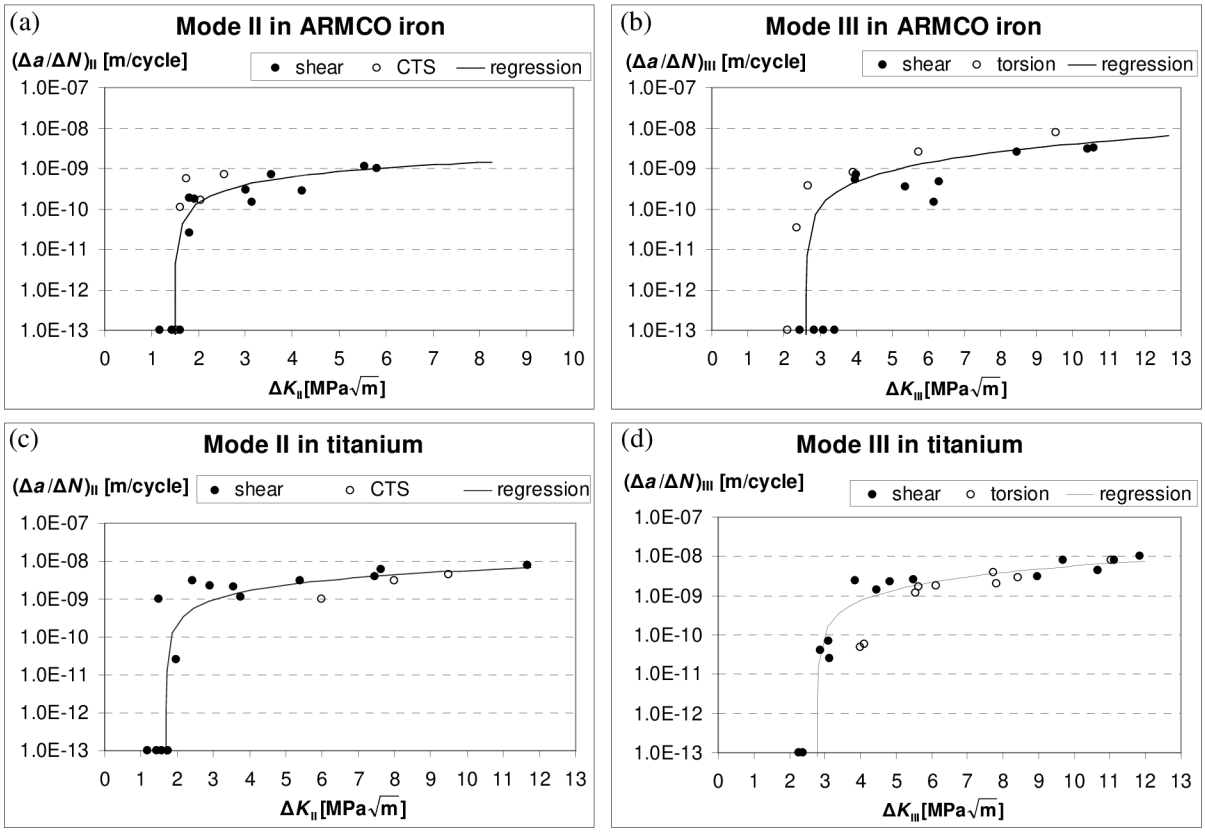

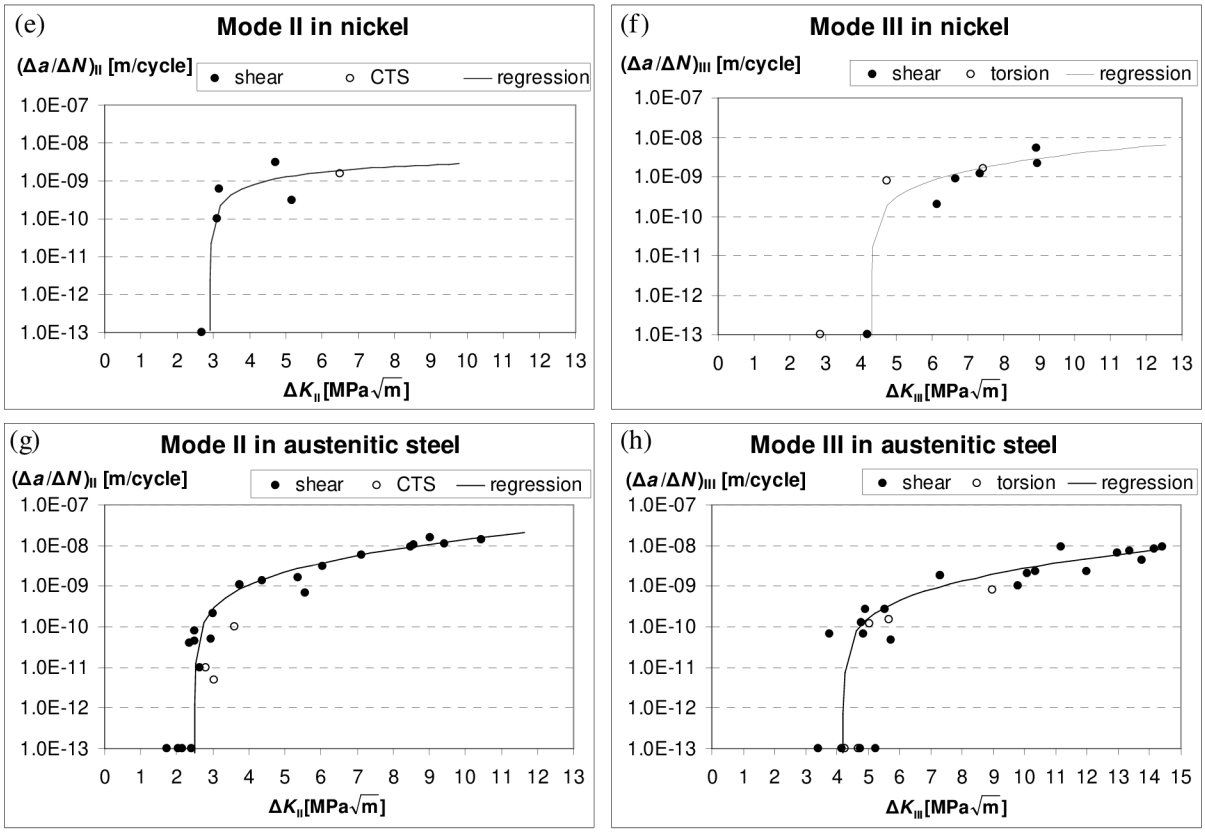

Fig. 21. Mean crack growth rate data for (a), (b) ARMCO iron; (c), (d) for α-titanium; (e), (f) for nickel and (g), (h) for austenitic steel X5CrNi18-10 obtained under remote mode II and III loading. The threshold values $\Delta K_{II,th}$ and $\Delta K_{III,th}$ for $\Delta a/\Delta N = 10^{-13}$ m/cycle are very close to the effective ones ($\Delta K_{II,th} \approx \Delta K_{IIeff,th}$ and $\Delta K_{III,th} \approx \Delta K_{IIIeff,th}$). It should be noted that the calculated ΔK_{II} and ΔK_{III} are global K values which do not take into account crack branching. Full circles – pure shear specimens, hollow circles – CTS specimens in mode II, torsion specimens in mode III.

In the ARMCO iron the crack growth rates are similar in both modes II and III, while in austenitic steel the crack growth rates are different in modes II and III. This is caused by the difference in levels of roughness-induced crack closure. In ARMCO iron small deviation of crack growth directions cause the same level of friction in modes II and III. In austenitic steel, the branches to local mode I cause that a highly deflected crack in the remote mode II is open and friction is reduced, whereas the factory-roof morphology in the remote mode III cause clamping of fracture surface and a high level of friction. The higher the tendency to deviate/twist to local mode I, the higher retardation of remote mode III cracks compared to those of remote mode II. ARMCO iron and austenitic steel exhibit the highest level of this effect. In a lower extent it can also be seen in nickel and titanium.

A principal difference between the mechanisms of mode II and mode III crack growth in the near-threshold region should be emphasized. In the first case, the mode I component induced by a deflection from the coplanar crack growth opens the crack thus reducing the friction and accelerating crack propagation. In the latter case, the local twisting processes inducing the mode I component create the factory-roof morphology that, in contrary, enhances the clamping of asperities in the crack wake and decelerates the mode III crack propagation [19,28,66,67]. This was, for example, the reason of the inverted notch effect in the austenitic steel in cyclic torsion, recently reported by Tanaka [28].

3.2 Fractographic Analysis in Three Dimensions

Micrographs of fracture surfaces from the experiments are presented in Fig. 22 – Fig. 26. Three crack path regions can be distinguished on the fracture morphology of the four investigated materials. They are marked by white dotted lines: a precrack emanating from the notch, the shear-mode crack and the final fracture (brittle or fatigue fracture in mode I). One should note that no traces of abrasive wear were found on precrack fracture surfaces of all specimens loaded near the threshold, thus confirming that the cracks propagated with a negligible interaction of crack flanks under a friction-free growth status.

In the ARMCO iron, both mode II and mode III faceted fracture surfaces suggest an influence of crystallography on the crack growth, which is also documented in the fracture profile in Fig. 22. Diversely oriented fibrous patterns with spatially random orientation may be confined to facets within individual grains. These fibrous marks highlight the positions of local crack front elements inside individual facets, which are mostly not parallel to the applied shear direction. The arrows in Fig. 22 indicate the local crack propagation directions which possess a noticeable mode II component parallel with the direction of applied shear stress. This corresponds to the model of local mode-II controlled micromechanism (Sub-section 1.3.4). The crack propagates in local mixed-mode I + II + III directions but the mode II crack growth can be considered to be predominant in both remote modes II and III loading cases.

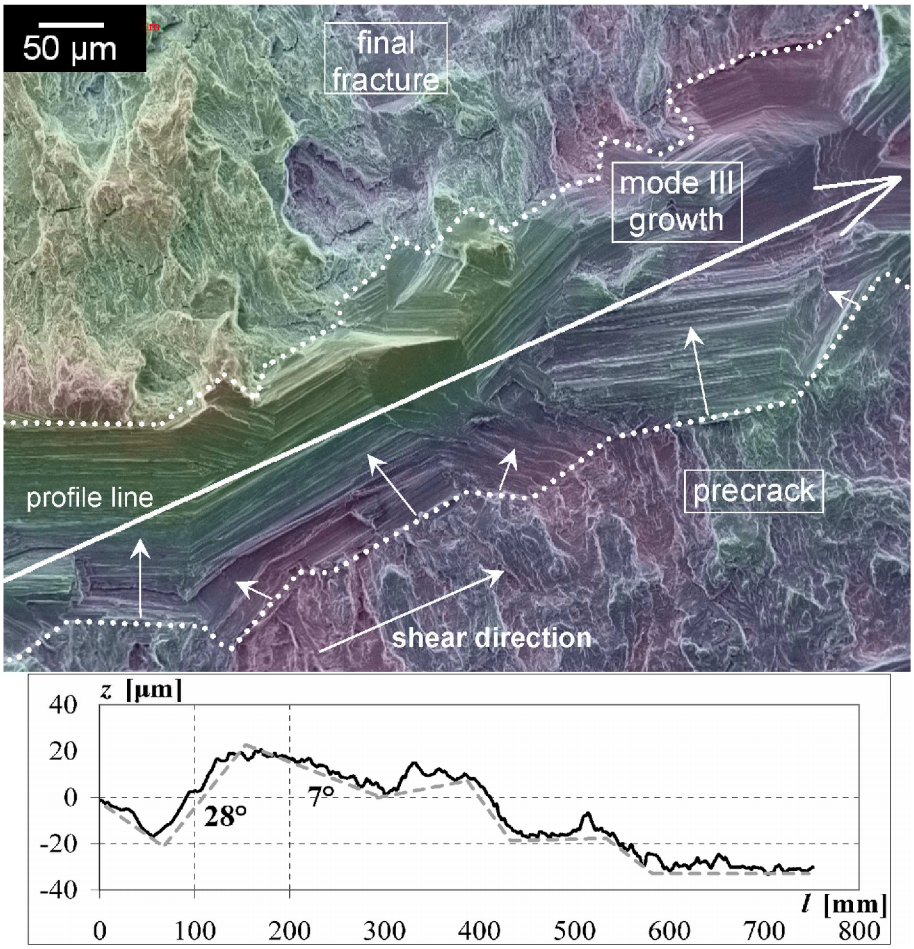

Fig. 22. Local mode II (I + II) assisted crack growth under remote mode III (torsion). The small arrows indicate the local crack propagation directions within individual grains. $\Delta K_{III} = 3.3$ MPa·m$^{1/2}$, $N = 1.5 \cdot 10^6$ cycles [50].

After the experiments, fracture surfaces of all specimens were examined by SEM and their morphologies were recontructed in 3D using stereophotogrammetry in order to identify local crack-path deviations of shear cracks from the coplanar crack growth. In Fig. 23 – Fig. 26, the fracture morphologies are presented along with the computed height profiles running parallel to the direction of applied shear stress. The vertical cutting planes that define the profiles are denoted by long white arrows. The coordinate l passes along the line from the left to the right or from the top to the bottom and the topological data are determined by the vertical coordinate z. These profiles were used for measurement of angles corresponding to the crack deflection or twisting from the crack (the maximum shear stress plane). The angles corresponding to crack deflection around the crack front were denoted α while angles β indicate twisting around the axis perpendicular to the crack front.

The profiles providing deflection angles run parallel to the shear direction in mode II (angles α_{II}) and perpendicular to the shear direction in mode III (angles α_{III}). The profiles providing twisting angles run perpendicular to the shear direction in mode II (angles β_{II}) and parallel to the shear direction in mode III (angles β_{III}). The angles α_{II} and β_{III} indicate the levels of deflection and twisting of crack fronts, determining the amount of local mode I support to in-plane shear crack propagation. The angles α_{III} and β_{II} do not have a special significance with respect to mode I contributions except for torsion test where the angles α_{III} also reflect the amount of the local mode I support at the crack front. Mean values and standard deviations of all angles are summarized separately for each of the two specimen types in Tables 3 and 4.

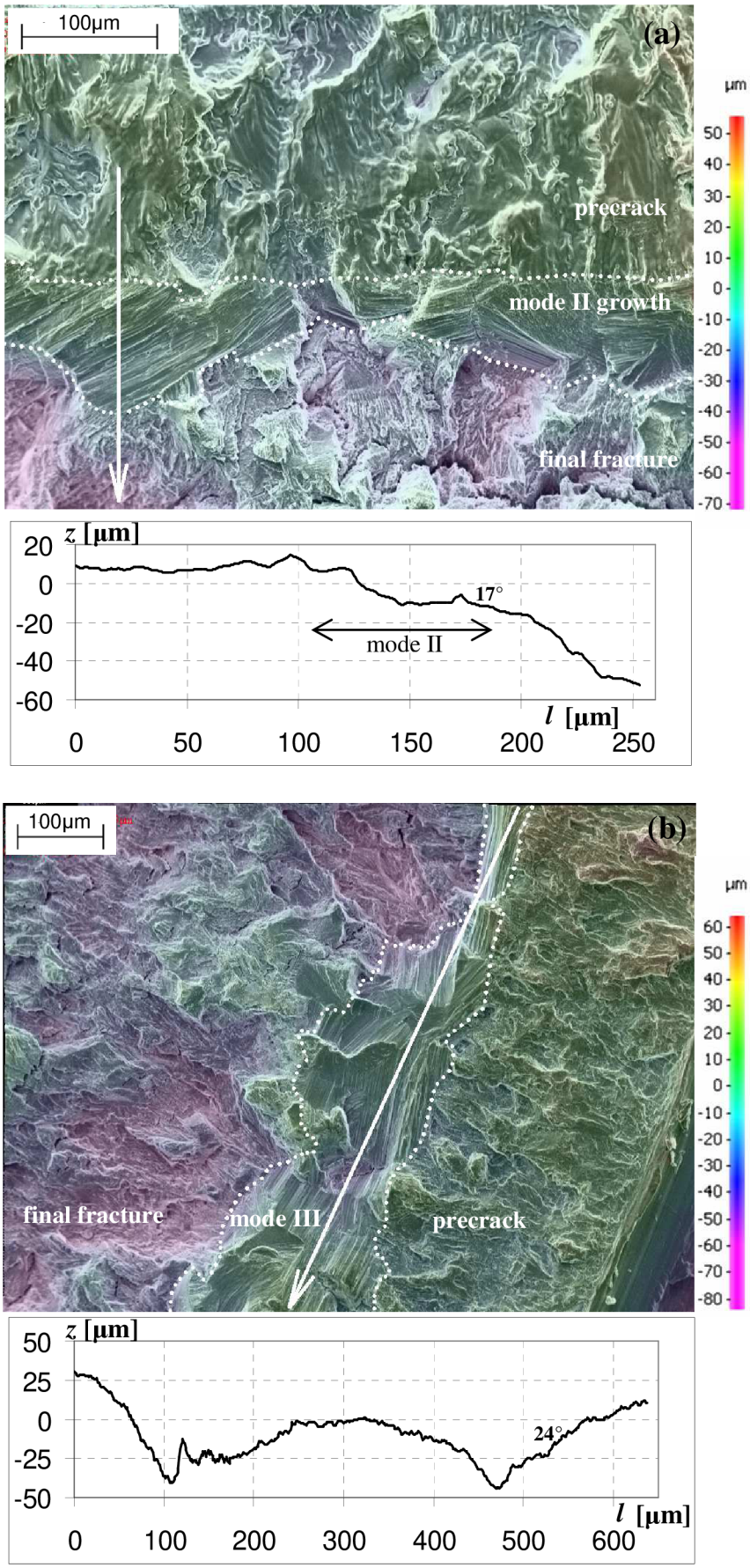

Fig. 23 Examples of fracture morphology and profiles along the indicated arrows for (a) mode II and (b) mode III in ARMCO iron. The heights in three dimensions can be assessed according to the colour codes.

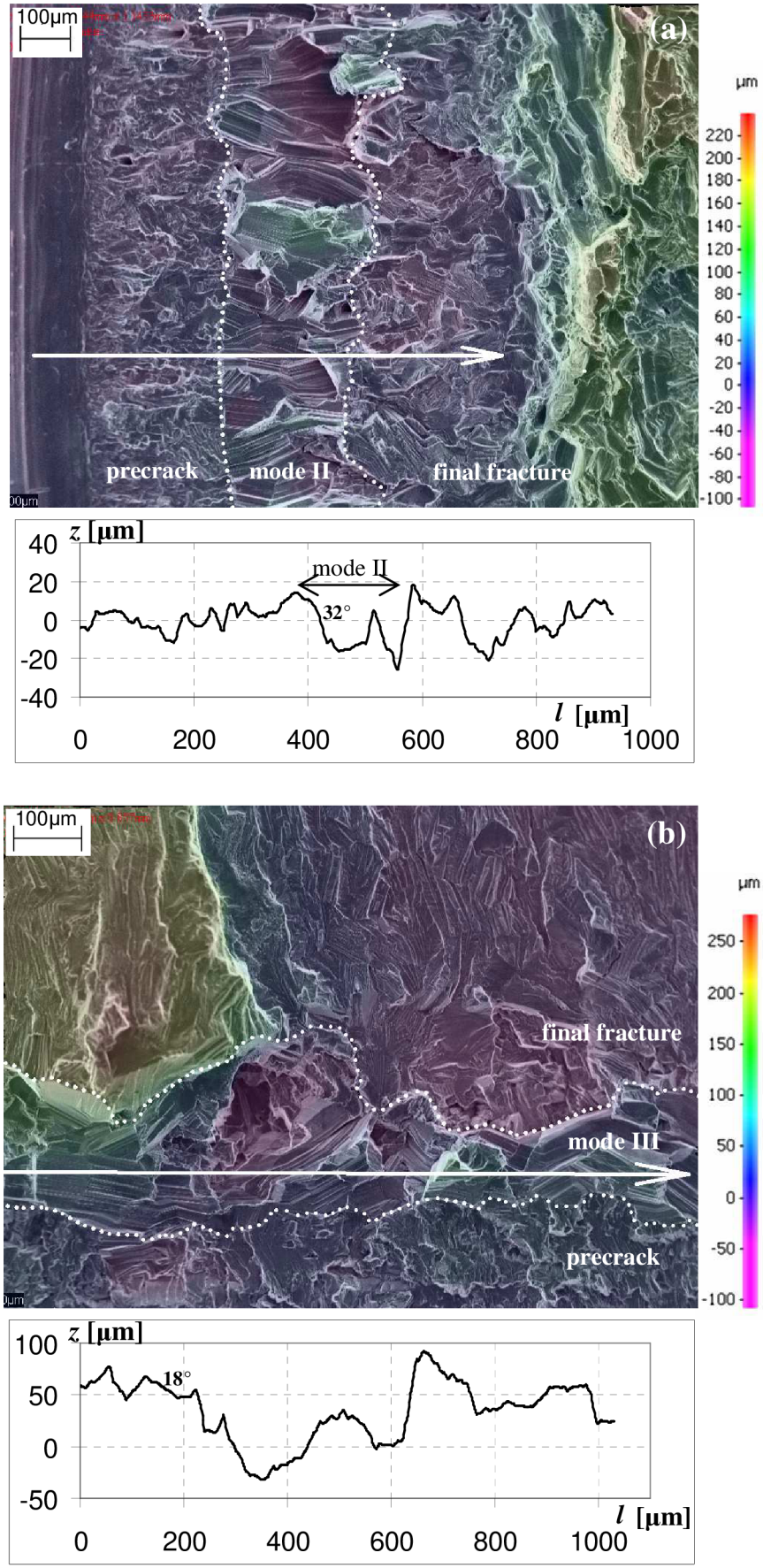

Fig. 24 Examples of fracture morphology and profiles along the indicated arrows for (a) mode II and (b) mode III in α-titanium (basic microstructure obtained by annealing at 850 °C). The heights in three dimensions can be assessed according to the colour codes.

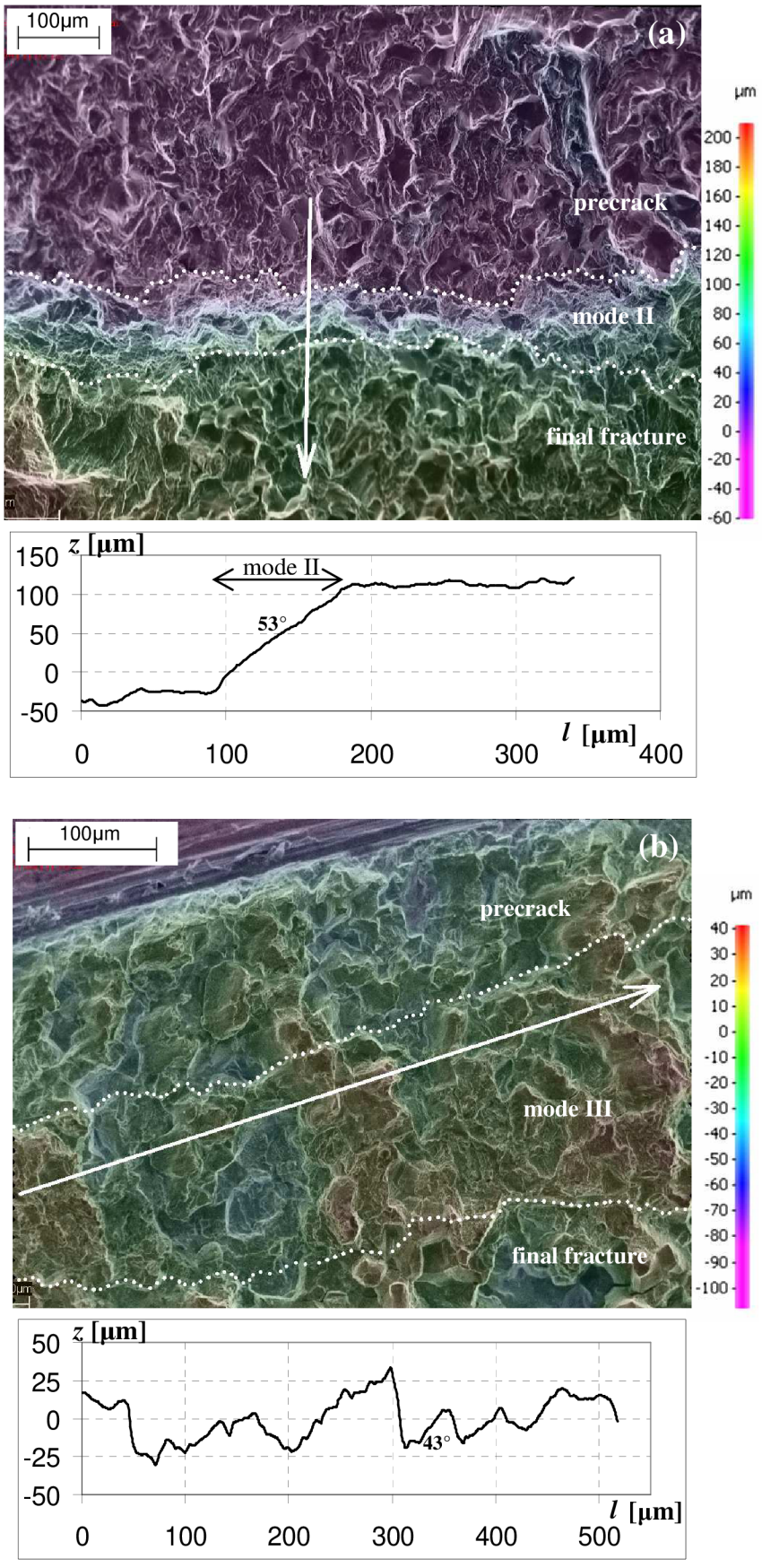

Fig. 25 Examples of fracture morphology and profiles along the indicated arrows for (a) mode II and (b) mode III in nickel. The heights in three dimensions can be assessed according to the colour codes.

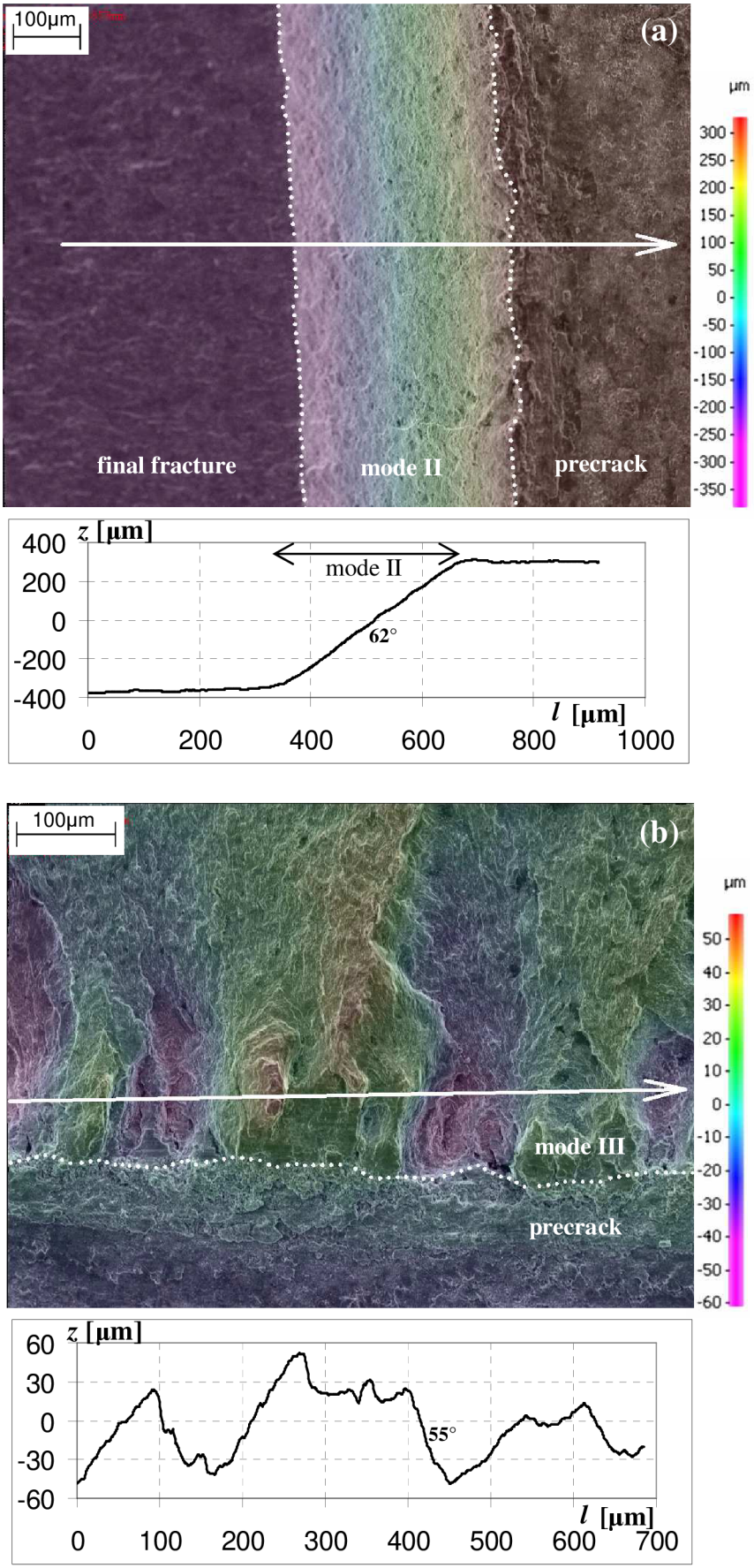

Fig. 26 Examples of fracture morphology and profiles along the indicated arrows for (a) mode II and (b) mode III in austenitic steel. The heights in three dimensions can be assessed according to the colour codes.

Table 3. Mean deflection and twisting angles [°] of mode II cracks near the threshold.

				specimen	
				shear	CTS
II	α_{II} [°]	deflection	ARMCO iron	18 ± 17	19 ± 8
			austenitic steel	66 ± 4	67 ± 5
			Ti	23 ± 19	56 ± 12
			Ti (needles)	43 ± 23	33 ± 30
			Ni	54 ± 22	50 ± 25
	β_{II} [°]	twist	ARMCO iron	18 ± 16	25 ± 20
			austenitic steel	7 ± 8	16 ± 8
			Ti	35 ± 20	9 ± 13
			Ti (needles)	39 ± 14	17 ± 16
			Ni	34 ± 23	42 ± 26

Table 4. Mean deflection and twisting angles [°] of mode III cracks near the threshold.

				specimen	
				shear	torsion
III	α_{III} [°]	deflection	ARMCO iron	18 ± 13	33 ± 34
			austenitic steel	19 ± 14	29 ± 18
			Ti	35 ± 24	25 ± 20
			Ti-needles		35 ± 19
			Ni	34 ± 18	28 ± 17
	β_{III} [°]	twist	ARMCO iron	19 ± 13	13 ± 10
			austenitic steel	33 ± 23	45 ± 8
			Ti	29 ± 21	38 ± 21
			Ti-needles		41 ± 19
			Ni	38 ± 22	34 ± 21

The fracture surfaces in the ARMCO iron are rather smooth with small relatively small mean angles (≈ 19°) of both deflection and twisting angles in all directions, which indicates a nearly coplanar crack growth. This means that the local crack growth was dominantly under shear modes with a relatively small support of mode I. The mean deflection angle β_{III} measured from the fracture surfaces of torsional specimens is rather high, which means that the torsional cracks propagated under a high mode-I support. This was already reported in [38] for specimens made of high strength steel.

A clear influence of crystallography was also detected on the fracture surfaces of both titanium grades (Fig. 24) but the angles α_{II} and β_{III} were found to be considerably higher. Even higher angles α_{II} and β_{III} were identified in nickel where the deflection of some facets was already close to the theoretical value of 70.5° of pure mode I branches. Nevertheless, whole fracture surface of both mode II and mode III cracks in nickel were still of a crystallographic nature with some exceptions for nickel as demonstrated in Fig. 25(a). Here a step of a deflection angle α_{II} = 53° was developed as a mode I branch under the remote mode II loading.

On the other hand, the deflection angles α_{II} measured on both the shear and CTS specimens in austenitic steel are close to the theoretical value of 70.5° of mode I branches. Here, the mode II cracks immediately formed a mode I branch and grew under the local opening mode. A steep step formed in this way on the fracture surface is showed in Fig. 26 along with the related crack path profile. The twisting angles α_{III} on fracture surfaces of shear and torsion specimens also approach the theoretical value of 45° for a mode I branch under remote mode III loading. The factory-roof morphology was created in both shear and torsion specimens. The related crack profile for a shear specimen is in Fig. 26. This reveals that such kind of morphology can be formed not only under torsion as reported in the literature [19,31] but also under simple shear. The fracture surfaces are locally rather smooth with no sign of crystallography influence and the morphology was very similar to that observed under mode I loading [50], see also Fig. 27(b). Thus, all remote shear-mode cracks in austenitic steel propagated locally under nearly pure opening mode I, controlled by a simple rule of the maximum-tangential stress criterion.

3.2.1 Connection to Dislocation Models

In the deformation model, the dislocations generated at the crack tip cause crack sliding displacements and generate new surfaces. Therefore, the crack should preferentially propagate in a mode II manner, with small inclinations to the direction where the tensile stresses are developed during the crack-tip loading. Such a small deflection generates an opening of the crack during loading, thus avoiding crack closure and friction of the crack flanks.

A comparison of the characteristic fractographic features near the threshold of stress intensity range indicates that the crack in the ARMCO iron propagates by the deformation model. On the other hand, it seems that dislocation-stimulated decohesion dominates the fatigue crack propagation in the austenitic steel near the threshold. This difference can also be observed in the mode I near-threshold fracture morphology as illustrated in Fig. 27. In the ARMCO iron, a crystallographic propagation along slip planes and in austenitic steel a non-crystallographic morphology of the fracture surface can be seen.

The fact that the crack growths near the threshold in austenitic steel and the ARMCO iron are controlled by different mechanisms (decohesion or deformation) might be attributed to the number of slip systems available for shear crack propagation in these metals. In the bcc structure of the ARMCO iron, a dense spatial set of possible slip systems <111> {110} and <111> {112} is available for dislocation emission and slip. This set consists of slip planes mutually exhibiting as much as nine different angles in the range of 0 – 90 degrees [35]. Therefore, there is a high probability to find slip planes in grains, adjacent to the precrack front, which exhibit the Schmid factor comparable to that of the precrack plane with maximum shear stress. Consequently, the crack can easily propagate along slip planes according to the deformation-based model by only slight deviations or twists with respect to the precrack plane in the ARMCO iron (low averaged deflection and twist angles in Table 3 and 4). On the other hand, the possible slip systems <110> {111} in the fcc structure of austenitic steel form a very thin set of planes exhibiting only one angle between 0 – 90 degrees. In austenitic steel, the crystallographically controlled crack growth becomes improbable.

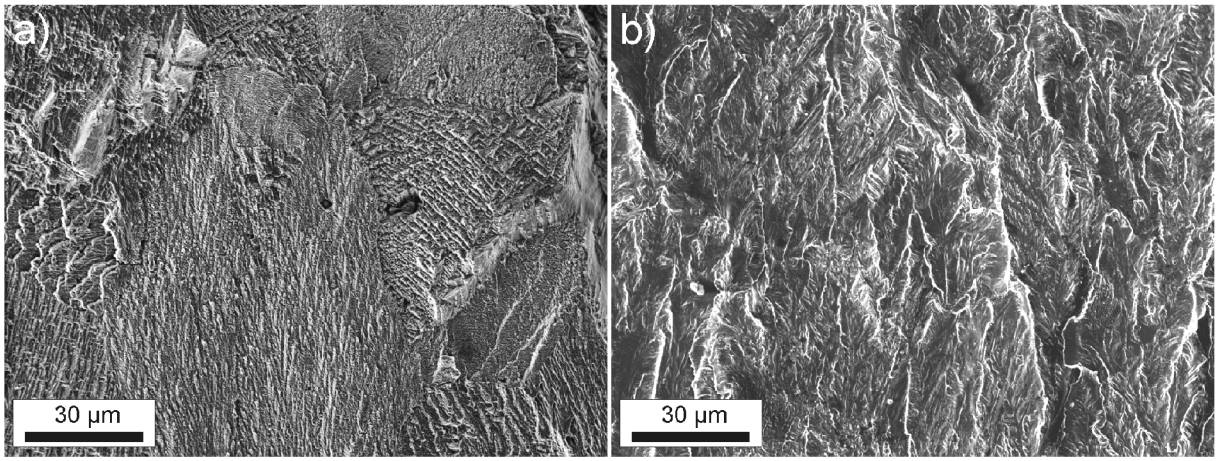

Fig. 27 Comparison of the typical fatigue fracture surface in mode I in the near-threshold regime: (a) ARMCO; (b) austenitic steel. In the case of the austenitic steel the crack propagates without exhibiting crystallographic features whereas in the ARMCO iron, a tendency of crack propagation along crystallographic planes is visible.

It should be noted that the two models used to explain the differences between austenitic steel and the ARMCO iron are not as diverse as they look. Both models originally used a 2D dislocation description of deformation and propagation of a cyclically loaded crack which, in some cases, represents a good approximation [25]. In many cases, however, the 3D nature of dislocation slip may become important and bring the two models closer together, for example the emission of dislocations on an inclined and twisted plane. Indeed, even such emitted dislocations cause blunting and can produce anti-shielding dislocations, which may trigger the decohesion process.

In the case of titanium and nickel, the crack morphologies and the mean deflection and twisting angles revealed that the propagation was a mixture of those in the ARMCO iron and austenitic steel. The crack growth was crystallography-controlled but the deflection/twisting angles were lower than those in the austenitic steel. Thus, the cracks locally propagated under a mixed mode I + II (or I + III). Such a behavior can also be understood in terms of available slip systems in the crystal lattices. In the hcp structure of α-titanium easy slip systems in the basal plane and more difficult slip systems in the prismatic and pyramidal planes create a state that represents a transition between the two extremes – the bcc structure with many available slip systems and the fcc structure of the austenitic steel with stacking faults. Nickel has also the fcc structure but it has high stacking-fault energy and the absence of stacking faults enables an easy cross slip of screw dislocations. Therefore, better manoeuvrability of dislocations in nickel favours, to some extent, the deformation model when comparing with the austenitic steel.

3.2.2 Local Loading Modes of Cracks Growing under Remote Modes II and III

The fractographical results in Section 3.2 revealed that, unlike in the ARMCO iron, titanium and nickel, a negligible local mode II component corresponded to the non-crystallographic mode I controlled crack branching in the austenitic steel. Here the difficult cross slip of screws favours single slip which seems to hinder a transfer of slip among incompatible slip systems inside the adjacent grains in directions both along the crack front and perpendicular to it. Similarly, the very low shear-mode component documents the factory-roof morphology that was formed under the remote mode III loading. There are also some indications that cyclic softening favours coplanar slip localization whereas cyclic hardening tends to prevent it [89]. However, cyclic softening/hardening response of studied materials was not investigated.

Knowledge of angles α_{II} and β_{III} enables us to approximately assess the mean values of local SIFRs $\Delta k_{Ieff,d}$, $\Delta k_{IIeff,d}$, $\Delta k_{Ieff,t}$, $\Delta k_{IIIeff,t}$ and the local mode mixities during the shear crack growth. When adopting simple schemes in Fig. 6 in Section 1.4 for mode II and mode III loaded precracks with elementary kinked and twisted crack fronts, the following relationships can be utilized:

$$\Delta k_{Ieff,d} = \frac{3}{2}\cos\frac{\alpha_{IIm}}{2}\sin\alpha_{IIm}\,\Delta K_{IIeff}, \tag{15}$$

$$\Delta k_{IIeff,d} = \frac{1}{2}\cos\frac{\alpha_{IIm}}{2}(3\cos\alpha_{IIm}-1)\Delta K_{IIeff}, \tag{16}$$

$$\Delta k_{Ieff,t} = \sin 2\beta_{IIIm}\,\Delta K_{IIIeff}, \tag{17}$$

$$\Delta k_{IIIeff,t} = \cos 2\beta_{IIIm}\,\Delta K_{IIIeff}, \tag{18}$$

$$\frac{\Delta k_{IIeff,d}}{\Delta k_{Ieff,d}} = \frac{3\cos\alpha_{IIm}-1}{3\sin\alpha_{IIm}}, \tag{19}$$

$$\frac{\Delta k_{IIIeff,t}}{\Delta k_{Ieff,t}} = \cot 2\beta_{IIIm}, \tag{20}$$

where α_{IIm} and β_{IIIm} are deflection and twist angles averaged for mode II and mode III specimens, respectively, and ΔK_{IIeff} and ΔK_{IIIeff} are effective SIFRs for straight precrack fronts [52]. The accuracy of Eqs. (15) – (20) is better than 2% except for Eq. (16) and $50° > |\alpha_{IIm}| > 70°$, where the accuracy is only within 5%. Local mode mixities computed according to Eqs. (19) and (20) are displayed in Table 5 for all investigated materials.

Table 5. Mean local mode mixities $\Delta k_{\mathrm{IIeff,d}}/\Delta k_{\mathrm{Ieff,d}}$ and $\Delta k_{\mathrm{IIIeff,t}}/\Delta k_{\mathrm{Ieff,t}}$ for investigated materials

	α_{IIm} [°]	$\Delta k_{\mathrm{IIeff,d}}/\Delta k_{\mathrm{Ieff,d}}$	β_{IIIm} [°]	$\Delta k_{\mathrm{IIIeff,t}}/\Delta k_{\mathrm{Ieff,t}}$
ARMCO iron	18	2.00	16	1.60
Titanium	39	0.70	36	0.32
Nickel	52	0.43	35	0.36
Austenitic steel	66	0.07	39	0.21

3.3 Intrinsic Resistance to Shear-mode Crack Growth

Effective thresholds $\Delta K_{\mathrm{IIeff,th}}$ and $\Delta K_{\mathrm{IIIeff,th}}$ for ARMCO iron, austenitic steel, titanium and nickel are displayed in Table 6. First, the question arises if the values of $\Delta K_{\mathrm{IIeff,th}}$ and $\Delta K_{\mathrm{IIIeff,th}}$ are really the effective ones. This can be assessed by comparison with results of atomistic models for cracked iron single crystal [57,58]. These models give the averaged value $k_{\mathrm{IIe}} \approx 0.75$ MPa·m$^{1/2}$ for generation of first dislocation during monotonic loading. Assuming the factor of 1.3 – 1.5 to reach the cyclic threshold [41] it gives $\Delta K_{\mathrm{IIeff,th}} \approx 1.0 - 1.2$ MPa·m$^{1/2}$. This is in a good agreement with the result of 1.5 MPa·m$^{1/2}$ for ARMCO iron that is expected to be somewhat higher than that for the single crystal due to incompatible geometrical crack/slip conditions for the dislocation emission in individual grains along the crack front. There is no plausible reason why such an agreement should not stand for the threshold data of other investigated metals as well.

Table 6. Measured effective thresholds $\Delta K_{\mathrm{IIeff,th}}$ and $\Delta K_{\mathrm{IIIeff,th}}$

Material	$\Delta K_{\mathrm{IIth,eff}}$ [MPa·m$^{1/2}$]	$\Delta K_{\mathrm{IIIth,eff}}$ [MPa·m$^{1/2}$]
ARMCO iron	1.5	2.6
Titanium	1.7	2.8
Austenitic steel	2.5	4.2
Nickel	2.9	4.3

3.3.1 Analytical Formulae for Intrinsic Thresholds in Modes I and II

The threshold data can be discussed from the point of view of the underlying physical principles. Liaw et al. [90] predicted that the effective mode I thresholds in metallic materials should be proportional to the Young modulus E. This was confirmed and further refined by the discrete dislocation models [41] which predicted the proportionality

$$\Delta k_{\mathrm{Ie}} \approx q_{\mathrm{I}} E \sqrt{b} \tag{22}$$

and, in the case of mode II cracks

$$\Delta k_{\mathrm{IIe}} \approx q_{\mathrm{II}} G \sqrt{b}\,, \tag{23}$$

where G is the shear modulus, b is the magnitude of Burgers vector and q_{I} and q_{II} are dimensionless coefficients. Values E, G and b along with products $Eb^{1/2}$ and $Gb^{1/2}$ for

investigated metals are presented in Table 7. In this table, $\boldsymbol{b} = a_L/2\ \langle 111 \rangle$ of the magnitude b = 248 pm for the ARMCO iron, $\boldsymbol{b} = a_L/2\ \langle 110 \rangle$ (b = 249 pm) for Ni and (b = 254 pm) for the austenitic steel were considered to be relevant. For Ti with hcp lattice, the dislocations with the Burgers vector $\boldsymbol{b}_{a+c} = a_L/3\ \langle 11\bar{2}3 \rangle$ (b = 554 pm) in "a+c" (pyramidal) slip systems $\{10\bar{1}1\}$ or $\{11\bar{2}2\}$ are the most representative ones since they are also responsible for twinning [91,92]. Indeed, the twinning deformation mechanism was observed in the investigated titanium, see EBSD image taken from the CTS specimen.

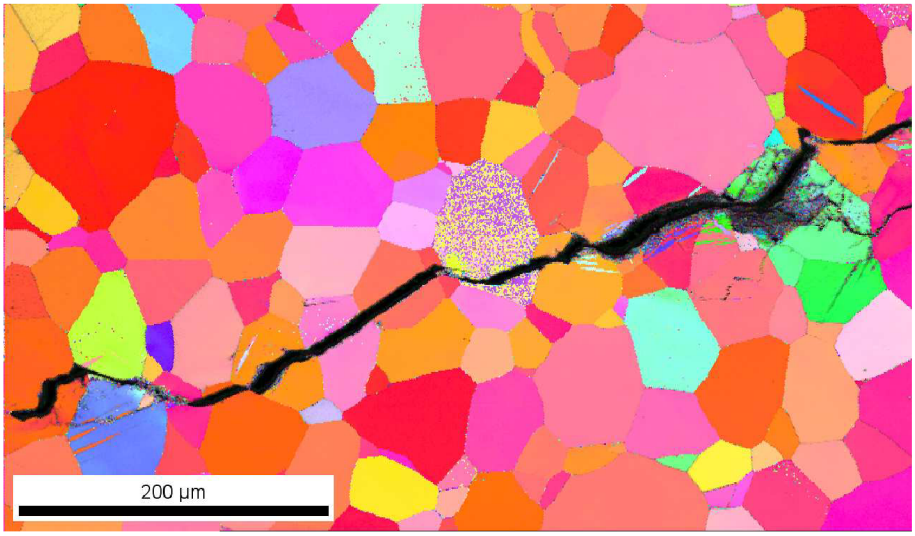

Fig. 28. EBSD image of a mode II crack in the CTS specimen in titanium (basic microstructure). Twinning deformation mechanism occurred in some of the grains.

Table 7. Values E, G, b, α_{IIm}, $Eb^{1/2}$, $Gb^{1/2}$ and $Gb^{1/2}/n_\alpha$ for investigated materials

Material	E [GPa]	G [GPa]	b [pm]	$Eb^{1/2}$	$Gb^{1/2}$	α_{IIm} [°]	$Gb^{1/2}/n_\alpha$
ARMCO iron	211	82	248.5	3.326	1.293	18	1.41
Titanium	116	44	554.0	2.730	1.036	39	1.66
Nickel	200	76	248.9	3.155	1.199	52	3.14
Austenitic steel	210	79	253.9	3.346	1.259	66	-

The simple deformation-based models consider a coplanar shear-mode crack propagation that was observed in the ARMCO iron only. In other metals the crack propagated along significantly deflected planes (see Table 3 and 4). As suggested by Vojtek et al. [50], this difference can be attributed to a much higher number of slip systems available for shear crack propagation in the bcc lattice when compared to both fcc and hcp ones. In the bcc structure, a dense spatial set of possible slip systems <111> {110} and <111> {112} is available for dislocation emission and slip. This set consists of slip planes mutually exhibiting as much as nine different angles in the range of 0 – 90 degrees (and even more when <111> {123} slip is activated). Therefore, there is a high probability to find slip planes in grains adjacent to the precrack front and exhibiting the Schmid factor comparable to that of the precrack plane of maximum shear stress. Consequently, the crack can easily propagate along such slip planes by only slight deviations with respect to the precrack plane which corresponds well to low

averaged deflection angles α_{IIm} measured for ARMCO (see Table 3). On the other hand, the possible slip systems <110> {111} in fcc structures of nickel and austenitic steel form a very thin set of planes exhibiting only one angle between 0 – 90 degrees. In the hcp lattice of titanium, similarly, the plastic deformation in the direction of c -axis cannot be ensured by easy slips in basal and prismatic systems. As a consequence, a significantly lower averaged local $\Delta k_{\mathrm{IIeff,d}}$ on deflected slip planes raises the $\Delta K_{\mathrm{IIeff,th}}$ value in fcc and hcp metals. This corresponds well to high deflection angles α_{IIm} of fracture facets measured for these materials (see Table 3 and 4). With respect to Eq. (22) and combining Eq. (16) and (23) one obtains the following formulas for effective mode I and II thresholds:

$$\Delta K_{\mathrm{Ieff,th}} = q_{\mathrm{I}} E\sqrt{b}\,, \tag{22a}$$

$$\Delta K_{\mathrm{IIeff,th}} = \frac{q_{\mathrm{II}}}{n_{\alpha}} G\sqrt{b}\,, \tag{23a}$$

where $n_{\alpha} = \frac{1}{2}\cos\frac{\alpha_{\mathrm{IIm}}}{2}(3\cos\alpha_{\mathrm{IIm}} - 1)$ [52]. The values α_{IIm} and $G\sqrt{b}/n_{\alpha}$ for ARMCO iron, titanium and nickel are displayed in Table 7. In the austenitic steel, a non-crystallographic mode I crack growth was observed. Therefore, Eqs. (23) and (23a) are not applicable and the "mode II" threshold is controlled by mode I loading, i.e., by Eq. (22a). A comparison of experimental $\Delta K_{\mathrm{Ieff,th}}$ (not available for nickel) and $\Delta K_{\mathrm{IIeff,th}}$ data with those calculated using Eqs. (22a) and (23a) for $q_{\mathrm{I}} \approx 0.75$ and $q_{\mathrm{II}} \approx 1.0$, respectively, is presented in Table 8. One can see a reasonable agreement between experimental and calculated values, including a precise prediction of the value $\Delta K_{\mathrm{IIeff,th}}$ = 2.5 MPa·m$^{1/2}$ for the austenitic steel using Eq. (22a). This value is also close to $\Delta K_{\mathrm{Ieff,th}}$ = 2.3 MPa·m$^{1/2}$ experimentally determined for mode I loading [93]. Note that the values $\Delta K_{\mathrm{IIeff,th}}$ calculated for ARMCO iron, titanium and nickel according to Eq. (23) that does not include the factor n_{α} would not fit the experimental data given in Table 8 – compare with values $Gb^{1/2}$ in Table 7. Thus, Eq. (23a) can be used for a rough prediction of $\Delta K_{\mathrm{IIeff,th}}$ for metallic materials when assuming $n_{\alpha,\mathrm{bcc}} \approx 0.9$, $n_{\alpha,\mathrm{hcp}} \approx 0.6$ and $n_{\alpha,\mathrm{fcc}} \approx 0.4$ for bcc, hcp and fcc metals, respectively. For fcc metals with a very low stacking fault energy, however, Eq. (22a) should be applied instead of Eq. (23a).

Table 8. Comparison of experimental and theoretical effective thresholds in modes I and II.

Material	$\Delta K_{\mathrm{Ieff,th}}$ [MPa·m$^{1/2}$]		$\Delta K_{\mathrm{IIeff,th}}$ [MPa·m$^{1/2}$]	
	experiment	Eq. (22a)	experiment	Eq. (23a)
ARMCO iron	2.7[a)]	2.5	1.5	1.4
Titanium	2.0[b)]	2.0	1.7	1.7
Nickel		2.3	2.9	3.1
Austenitic steel	2.3[c)]	2.5	2.5	2.5[d)]

[a)] [94], [b)] [95,96], [c)] [93], [d)] Eq.(22a)

3.3.2 Comparison of Theoretical and Experimental Threshold Ratios

Both dislocation models of crack growth give mode I threshold values somewhat smaller than the experimentally observed effective values, which might be a consequence of the 3-dimensional nature of the crack [48]. Both mechanisms are reasonable and, in principle, they might be responsible for the threshold at different positions along the crack front in a material. The mechanism which delivers the smallest local $\Delta K_{\mathrm{eff,th}}$ should determine whether the crack can locally propagate or not.

The experimentally determined differences in the effective thresholds can be compared with predictions based on the assumed crack growth models explaining the fractographic features. In the case of the deformation-induced surface generation (ARMCO iron) the ratio between $\Delta K_{\mathrm{Ieff,th}}$ and $\Delta K_{\mathrm{IIeff,th}}$ should be equal to the ratio of the local stress intensities k_{Ie} and k_{IIe} to generate an edge dislocation under modes I and II, respectively, i.e.,

$$\frac{\Delta K_{\mathrm{Ieff,th}}}{\Delta K_{\mathrm{IIeff,th}}} \approx 2\,. \tag{24}$$

There are several estimations of k_{Ie} and k_{IIe} in the literature [25], the differences are relatively small. The ratio of $k_{\mathrm{Ie}}/k_{\mathrm{IIe}}$ is about 2, which fits well with measured ratios of $\Delta K_{\mathrm{Ieff,th}}/\Delta K_{\mathrm{IIeff,th}} \approx 1.84$ for the ARMCO iron ($\Delta K_{\mathrm{Ieff,th}} = 2.75$ MPa·m$^{1/2}$ [94], see also Table 8).

If the decohesion controls the fatigue crack propagation (austenitic steel) both the tensile stress field of the crack and the tensile stress field of a dislocation for the different loading cases should control the effective threshold. The near crack tip tensile stress is determined by the local k_{I}. The maximum of the local k_{I} for a global K_{II} is obtained for a kink angle $\alpha_{\mathrm{IId}} = 70°$ from Eq. (6) as $k_{\mathrm{Id}} = 1.15K_{\mathrm{II}}$. The local k_{I} under global mode I loading has a maximum for the straight crack where $k_{\mathrm{I}} = K_{\mathrm{I}}$. If one assumes that the probability to move dislocation with its tension stress field close to the crack tip is the same for the mode I and the kinked mode II, then

$$\frac{\Delta K_{\mathrm{Ieff,th}}}{\Delta K_{\mathrm{IIeff,th}}} = 1.15\,. \tag{25}$$

For austenitic steel $\Delta K_{\mathrm{Ieff,th}} = 2.3$ MPa·m$^{1/2}$ [93] and $\Delta K_{\mathrm{IIeff,th}} = 2.5$ MPa·m$^{1/2}$ which gives $\Delta K_{\mathrm{Ieff,th}}/\Delta K_{\mathrm{IIeff,th}} \approx 0.9$. This small discrepancy might be caused by the different probability to move antishielding dislocations sufficiently close to the crack tip in the case of a global mode I and mode II crack.

The k_{IIIe} values for the coplanar emission of screw dislocations at the mode III crack front (see, for example [58]) were estimated to be somewhat smaller than those of k_{IIe}, which would not fit the measured ratio $\Delta K_{\mathrm{IIIeff,th}}/\Delta K_{\mathrm{IIeff,th}} \approx 1.7$ for investigated materials at all. If one supposes that only the local mode II segments propagate under global mode III loading then the local mode II stress components at the microtortuous crack front should only be taken into account. Assuming that the mean deviation angle of the in-plane ledges of the precrack front is 30°, the ratio of the local mode II and mode III shear stress is $\tau_{\mathrm{II,d}}/\tau_{\mathrm{III}} = 0.5$ as follows from a geometrical separation of the local shear stresses [38] (see also Fig. 5(a)) and, consequently, the ratio $\Delta K_{\mathrm{IIIeff,th}}/\Delta K_{\mathrm{IIeff,th}}$ should be about 2. However, the in-plane angle of 30°is rather an upper limit of the precrack tortuosity. Therefore, it seems that also mechanisms other than the local mode II displacements partially contribute to mode III crack growth as, e.g., the accumulative damage mechanism inside the cyclic plastic zone.

3.3.3 Mode I Branching Criterion

When knowing the effective values $\Delta K_{\mathrm{IIeff,th}}$, one can check the validity of the simple branching (bifurcation) criterion $\Delta k_{\mathrm{Id}} = 1.15\ \Delta K_{\mathrm{IIeff,th}} \geq \Delta K_{\mathrm{Ieff,th}}$ at the crack growth thresholds of all investigated materials. This is presented in Table 9. When inserting Eqs. (22a) and (23a) into the criterion, $1.15\ \Delta K_{\mathrm{IIeff,th}} = \Delta K_{\mathrm{Ieff,th}}$, the transition branching angle $\alpha_{\mathrm{IIts}} \approx 40°$ can be determined as a value practically independent of a material. Indeed, one gradually obtains ($\nu \approx 0.3$) [52]:

$$n_\alpha = 1.15\frac{4G}{3E} \approx \frac{0.77}{1+\nu} \approx 0.6 = \frac{1}{2}\cos\frac{\alpha_{\mathrm{IIts}}}{2}(3\cos\alpha_{\mathrm{IIts}} - 1) \ \rightarrow\ \alpha_{\mathrm{IIts}} \approx 40^{\mathrm{o}} \tag{26}$$

Table 9. Fulfilment of the branching criterion $\Delta k_{\mathrm{Id}} \geq \Delta K_{\mathrm{Ieff,th}}$

Material	Branching criterion [MPa·m$^{1/2}$]
ARMCO iron	1.7 < 2.7
Titanium	2.0 ≈ 2.0
Nickel	3.3 > 2.3
Austenitic steel	2.9 > 2.3

With respect to Table 9, obviously, the value $\alpha_{\mathrm{IIts}} \approx 40°$ and the related mode mixity $\Delta k_{\mathrm{IIeff,d}}/\Delta k_{\mathrm{Ieff,d}} = 0.67$ according to Eq. (19) well correspond to respective $\alpha_{\mathrm{IIm}} = 39°$ and $\Delta k_{\mathrm{IIeff,d}}/\Delta k_{\mathrm{Ieff,d}} = 0.70$ as measured for titanium (Table 5). Although the branching condition in nickel is fulfilled, the global character of the morphology is still of a crystallographic shear dominance. There are, however, some facets exhibiting a pure mode I control (see Fig. 8) which might explain that the prediction $\Delta K_{\mathrm{IIeff,th}} = 3.1$ MPa·m$^{1/2}$ according to Eq. (23a) is somewhat higher than the experimental value of 2.9 MPa·m$^{1/2}$. Indeed, Eq. (22a) based on a pure mode I loading predicts a considerably lower value of 2.3 MPa·m$^{1/2}$. A comparison of the results in Table 9 with the mode mixities $\Delta k_{\mathrm{IIeff}}/\Delta k_{\mathrm{Ieff}}$ in Table 5 shows that the criterion starts to be fulfilled when the local opening mode becomes higher than the local shear-mode one. In another words, the criterion is sensitive to the transition from the local shear mode to the local opening mode. However, a global control of the opening mode over the crack propagation starts only at angles $\alpha_{\mathrm{II}} \approx 60°$ significantly higher than α_{IIts}. Note that the mode mixity related to the transition angle α_{IIts} is close to that for small crystallographic cracks growing in surface slip bands under remote push-pull loading. These cracks are also shear-mode controlled since the movement of dislocations in slip planes is practically unaffected by the normal stress.

Finally, it should be mentioned that another bifurcation criterion based on the maximum crack growth rate [73,89]. It turns out that mode II is faster than mode I in the large-scale-yielding region but that effective mode I and mode II kinetics seem to converge and intersect at the transition to small-scale yielding region. This intersection is associated with a transition from tensile-stress controlled (deflected) crack path at small-scale yielding to shear-stress controlled (coplanar) one at large scale yielding. Prediction of this transition can be done either through laboratory tests of mode I and II crack growth rates [89] or theoretically by application of two critical-plane based fatigue life criteria [73].

3.3.4 Important Outcomes for Materials Science and Engineering

At the threshold loading level (R = 0.1), the extent of the cyclic plastic zone, R_p, at the precrack tip is less than (or comparable to) the characteristic microstructural distance in all the investigated materials. Indeed, when using a simple Irwin's formula, the Rice transformation scheme and the Tresca criterion for the yield stress in simple shear $\tau_y = \sigma_y/2$ one obtains $r_p \approx \frac{1}{2\pi}\left(\frac{K_{\mathrm{IIeff,th}}}{\sigma_y}\right)^2$. This gives $r_p \approx 10$ µm for ARMCO iron, $r_p \approx 15$ µm (8 µm) for titanium 850 °C (950 °C), $r_p \approx 60$ µm for nickel and $r_p \approx 20$ µm for the austenitic steel [52] which means that the influence of microstructural barriers does not play any important role and the main factors controlling the intrinsic shear-mode thresholds are only related to matrix (lattice) characteristics G, b and α_{IIm} that explicitly appear in Eq. (23a). A high intrinsic shear-mode threshold is, therefore, ensured by a high shear modulus G (high strength of interatomic bonds), a long Burgers vector (small manoeuvrability of dislocations) and a high mean deflection angle α_{IIm} (small number of available slip systems).

During crack propagation, the cyclic plastic zone becomes comparable to or higher than the characteristic microstructure distance and the intrinsic resistance to shear-mode crack growth starts to be microstructurally dependent. In the near-threshold region, however, the extrinsic part of the resistance (friction induced closure) is usually much higher than the intrinsic one. Therefore, the existence of large crack-wake asperities resistant to rubbing is decisive for an improvement of the total resistance to shear-mode crack growth. This means that a coarse and stable microstructure still possessing a sufficiently high yield stress is the most important demand for a high resistance to propagation of shear-mode cracks in the near-threshold region. Several times higher extrinsic (closure) component than the intrinsic one also play a significant role in propagation/non-propagation of modes II, III and II + III cracks in engineering structures, e.g. rails [18].

Height of the crack-wake asperities, which depends on the level of local mode I branching, determines the difference between crack growth rates in modes II and III. In material with relatively plain fracture surfaces (emission of dislocations from the crack tip is a dominant mechanism) crack growth rates in modes II and III are nearly comparable. On the other hand, crack growth rates are much higher for mode III than those of mode II in materials where factory-roof crack flanks are generated. Considering the relationship (1), effective thresholds, which can be obtained by the experimental procedure presented in this work, enable predicting of the closure component:

$$\Delta K_{\mathrm{closure}} = \Delta K_{\mathrm{applied}} - \Delta K_{\mathrm{effective}}. \tag{27}$$

In the large scale yielding region the intrinsic component becomes dominant due larger displacement of the crack flanks and a friction wear of the asperities. In this case crack propagation in mode III is slower than mode II because of the more complicated intrinsic mechanism.

Finally, it should be mentioned that in some cases the crack closure is small, e.g. cracks initiated by corrosion or microcracks along grain boundaries created after thermal treatment. Their threshold can be close to the effective one. The effective thresholds measured in this work represent the theoretical minimum which should be taken into account for design in order to be on the safe side.

3.4 Mixed Mode II + III

So far the work was focused on pure modes II and III. However, a combination of these two modes occurs in many real cases. The amount of known experimental and theoretical effective data for mixed mode II + III is even more limited than that of pure modes II and III. Some new experimental data along with a few attempts found in literature are shortly presented in this section.

In order to describe the mixed-mode II + III crack propagation, there is an effort to express the data in terms of an equivalent stress intensity range (ΔK_{eq}). When assuming that the range of energy release rate is a quantity controlling the crack growth rate under plane strain and small scale yielding conditions, the mixed-mode crack growth rate data can be described by an equivalent SIFR $\Delta K_{eq} = \sqrt{\Delta K_{II}^2 + \lambda \Delta K_{III}^2}$. The coefficient λ decides about the weights of contributions of mode II and III components to the crack growth rate: $\lambda = 1/(1 - \nu) \approx 1.45$ stands for equal weights of ΔK_{II} and ΔK_{III} and $\lambda < 1.45$ ($\lambda > 1.45$) means a lower (higher) weight of mode III component. Doquet et al. [17] searched the optimum correlation (based on the correlation coefficient) for maraging steel and Ti-6Al-4V alloy using the relationship $\Delta K_{eq,eff} = \sqrt{\Delta K_{IIeff}^2 + \lambda \Delta K_{IIIeff}^2}$ in the Paris-Erdogan crack-growth regime. The effective values of SIFR were determined by means of a comparison of measured in-plane and out-of-plane sliding displacements on free surfaces with those obtained from elastic-plastic FEM calculations. The values $\lambda = 1.2$ for the maraging steel and $\lambda = 0.9$ for the Ti-6Al-4Vwere found to be the most appropriate ones. This means that, in both investigated materials, the mode III component of the crack driving force was less efficient than that of the mode II.

Doquet et al. [17] also assessed the ratio of effective and nominal SIFR $\Delta K_{eff}/\Delta K_{nom}$ for Ti-6Al-4V and maraging steel in the Paris-Erdogan region. For Ti-6Al-4V this ratio ranged from 0.12 to 0.7 and in the maraging steel from 0.51 to 1.0 in dependence of applied loading level and the mode mixity $\Delta K_{II}/\Delta K_{III}$. Higher loading amplitude and mixity ratio corresponded to higher values of $\Delta K_{eff}/\Delta K_{nom}$, which is in agreement with assumptions (Section 3.3.4) about higher extrinsic component of mode III cracks compared to that of mode II cracks.

3.4.1 Tested Equivalent Stress Intensity Factors for Mixed Mode II + III in ARMCO Iron

If the modes II and III crack growth mechanisms under the same applied SIFs ΔK_{II} and ΔK_{III} were equally efficient, i.e., if the contributions of ΔK_{II} and ΔK_{III} in the mixed-mode II + III were identical, the crack growth rate under this kind of loading should be described in terms of the classical criterion based on the energy released rate:

$$G_E = \frac{1-\nu^2}{E}\left(K_{II}^2 + \frac{1}{1-\nu}K_{III}^2\right) \tag{28}$$

$$\Delta K_{eq} = \sqrt{\Delta K_{II}^2 + \frac{1}{1-\nu}\Delta K_{III}^2}\,. \tag{29}$$

Since the identical influence of ΔK_{II} and ΔK_{III} is not necessarily true, a more justified equivalent SIFR in the above mentioned manner [17] was used and assessed.

$$\Delta K_{eq} = \sqrt{\Delta K_{II}^2 + \lambda \cdot \Delta K_{III}^2}\ , \tag{30}$$

If the coefficient λ is smaller than $1/(1 - \nu) \approx 1.43$, the efficiency of mode III mechanism is less than that of the mode II. Values $\lambda \in \langle 0.4, 3.0 \rangle$ were used for fitting the experimental data and the results were assessed according to the goodness of fits of the regression curves based on the coefficient of determination R^2. The formula of Klesnil and Lukáš [11] (31) was used as a regression function suitable for the near-threshold region, where A, ΔK_{th} and n are fitting parameters.

$$\frac{\Delta a}{\Delta N} = A\left(\Delta K^n - \Delta K_{th}^n\right), \tag{31}$$

Examples of evaluated ΔK_{eq} for λ = 0.6, λ = 1.1 and λ = 2.0 are presented in Fig. 29. The diagram in Fig. 30 shows the dependence of R^2 on the tested values of λ from Eq. (30). The coefficient R^2 reached its maximum value for λ between 1.0 and 1.2.

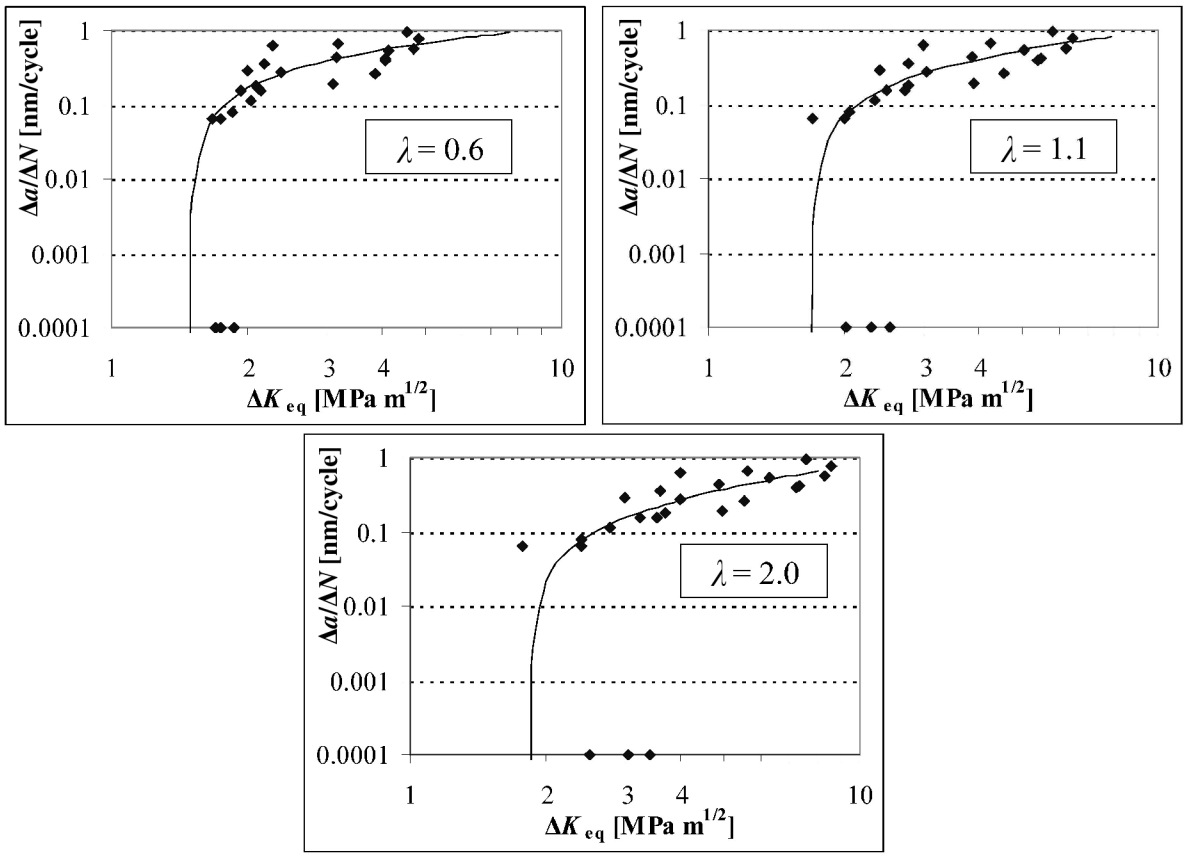

Fig. 29. Examples of diagrams with evaluated fitting curves for λ = 0.6, λ = 1.1 and λ = 2.0.

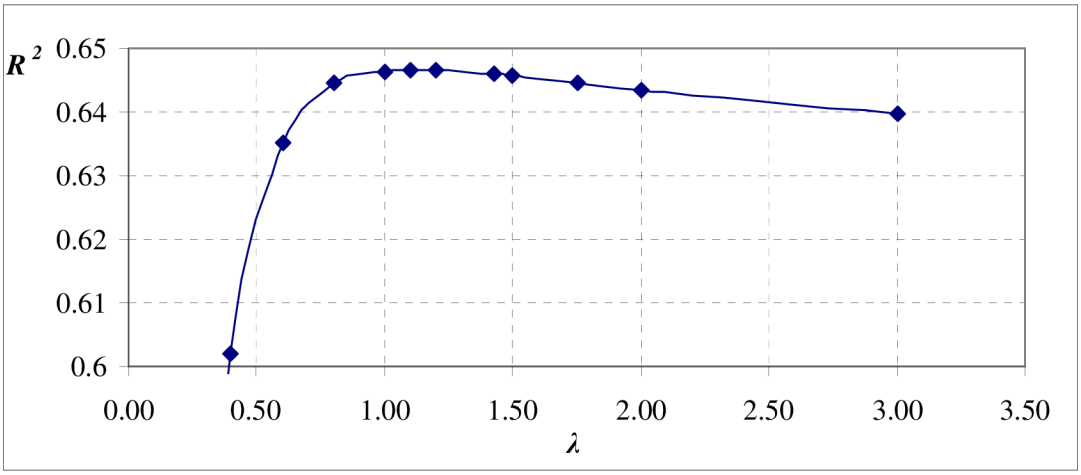

Fig. 30. Dependence of the coefficient of determination R^2 on tested values of λ.

First, it should be noted that the only truly effective values are those at the threshold $\Delta K_{eq,th}$. The crack growth above the equivalent threshold is already accompanied by a certain level of friction (closure), which means that the values of ΔK_{eq} are somewhat higher than those of $\Delta K_{eq,eff}$.

The results showed that the weight parameter λ with the best fit was $\lambda \approx 1.1$. This value is less than $1/(1 - \nu)$ which means that, in the near-threshold regime, the mode III component of the crack driving force was slightly less efficient than that of the mode II. These results are in accordance with those from [17].

Other formulas for sorting the mixed-mode data were also used. The following formulae normalized to 1 when approaching the mixed-mode threshold were used in [97]:

$$A = \sqrt{\left(\frac{\Delta K_{IIm}}{\Delta K_{IIth}}\right)^2 + \left(\frac{\Delta K_{IIIm}}{\Delta K_{IIIth}}\right)^2} \tag{32}$$

$$B = \frac{\sqrt{\Delta K_{IIm}{}^2 + \Delta K_{IIIm}{}^2}}{\Delta K_{th}} \; ; \qquad \Delta K_{th} = \frac{1}{2}\left(\Delta K_{IIth} + \Delta K_{IIIth}\right) \tag{33}$$

$$C = \frac{\sqrt{\kappa_2 \cdot \Delta K_{II}{}^2 + \kappa_3 \cdot \Delta K_{III}{}^2}}{\sqrt{\kappa_2 \cdot \left(\Delta K_{IIth} \cos\varphi\right)^2 + \kappa_3 \cdot \left(\Delta K_{IIIth} \sin\varphi\right)^2}} . \tag{34}$$

Values of mode II and III thresholds $\Delta K_{II,th}$ (= $\Delta K_{IIeff,th}$) = 1.5 MPa·m$^{1/2}$ and $\Delta K_{III,th}$ (= $\Delta K_{IIIeff,th}$) = 2.6 MPa·m$^{1/2}$ were included into these criteria. In the criterion (34) weights of pure mode components κ_2 and κ_3 were investigated and the best result provided the combination of values κ_2 = 1.5 – 2.0 and κ_3 = 1.0, which is also in a qualitative agreement with the previous results.

3.4.2 Mixed-mode II + III Fractography

The relationship for intrinsic resistance to crack propagation under pure mode II near threshold and a verification of mode-I-branching criterion are mentioned in Section 3.3. As regards mixed mode II + III loading, however, such an analysis has not yet been done.

Data from experiments with the simple shear specimens (2.4) were analyzed [98]. A three-dimensional topography of mixed-mode II + III cracks and a comparison of the stereophoto-grammetrical data obtained from fracture surfaces of the ARMCO iron, α-titanium, nickel and austenitic steel was done. The objective was to show how each of the local modes II and III contributes to a generation of fracture surfaces. This can provide an initial viewpoint on the intrinsic resistance to crack growth under mixed mode II + III loading and an assessment of the crack growth micromechanisms (in relation to the atomistic models presented in Section 1.3).

Fracture surfaces were reconstructed in 3D using the stereophotogrammetry in SEM. The resulting images are presented in Fig. 31. They reveal an evidence of crystallography-controlled crack propagation for ARMCO iron, titanium and nickel which was also observed for pure modes II and III. On the other hand, no crystallography influence can be detected in the austenitic steel (Fig. 31(d)) where characteristic regular-shaped hills are created during the remote mixed-mode II + III loading. They represent a transition between the high crack front deflection observed in pure remote mode II and the factory-roof morphology typical for pure remote mode III [1,2]. This is, most probably, caused by a local mode I crack growth mechanism according to the model of Deshpande et al. [7]. A qualitatively similar fracture morphology consisting of periodical fracture segments differently inclined to the macroscopic plane was observed by Hourlier and Pineau [8] in the high-strength low-alloy steel loaded in mixed mode I(cyclic)+III(static).

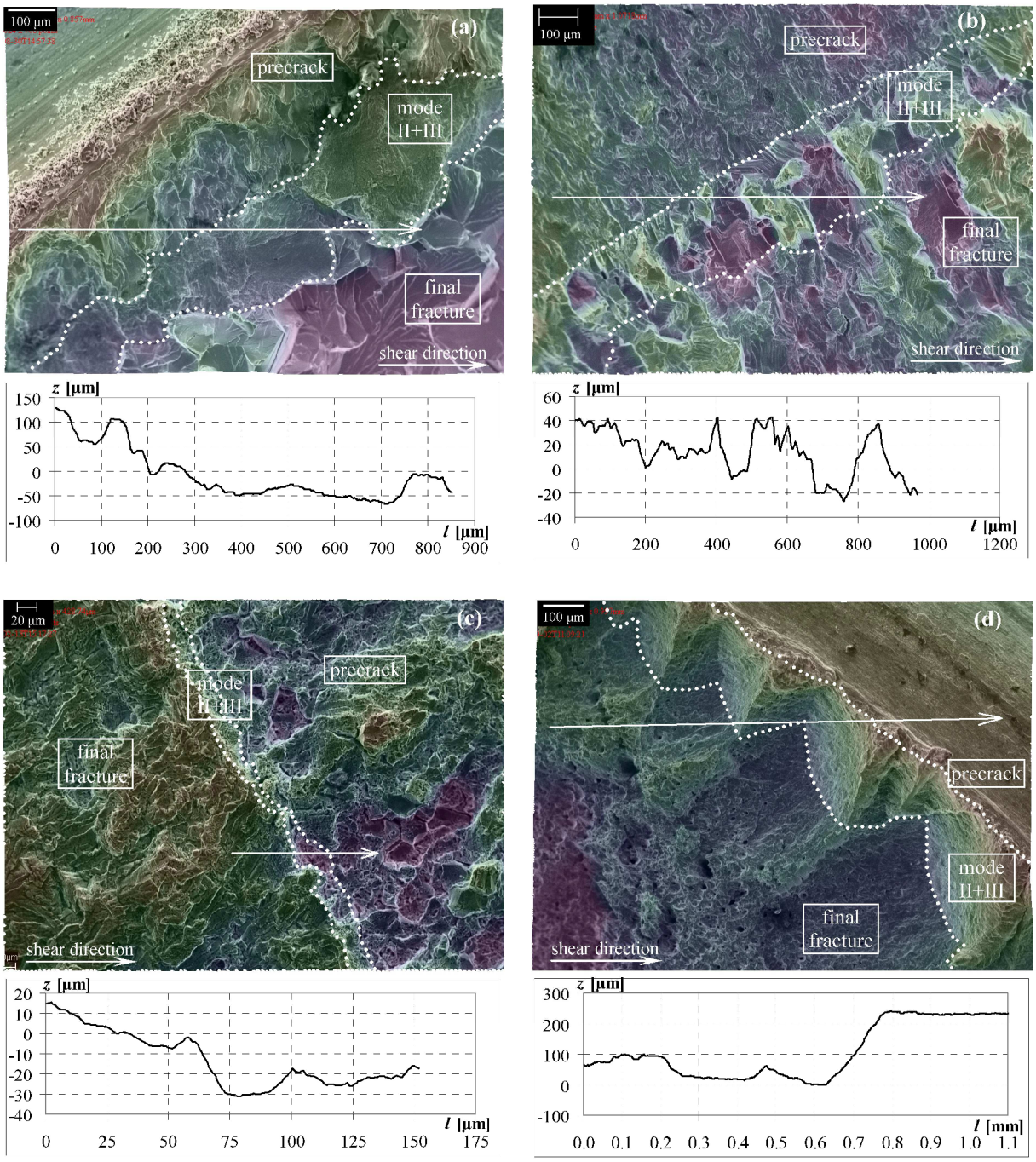

Fig. 31. Examples of fracture morphologies for remote mixed-mode II + III cracks with the height profiles corresponding to the white horizontal arrows in (a) ARMCO iron; (b) titanium; (c) nickel; (d) austenitic steel.

Quantification of the 3D data was done by analysis of height profiles determined by cutting planes denoted by the white arrows in Fig. 31. The coordinate l passes along the line from the left to the right and the topological profiles were determined by the vertical coordinate z. These profiles were used for a measurement of angles γ corresponding to the average crack deviation from the plane of the maximum shear stress. The profiles running parallel to the shear direction provide angles α while those of the perpendicular direction indicate angles β. The average deviation angles $\gamma_{II+III} = (\alpha + \beta)/2$ were calculated, summarized in Table 10 for all investigated materials and compared to those for respective pure modes II and III, obtained in the same way as average deviation angles γ_{II} and γ_{III}.

The deviation angles in the ARMCO iron are relatively small (up to 20°) and the cracks propagated here in a nearly coplanar manner under shear-mode dominance. In titanium these angles were much higher compared to those in the ARMCO iron. The highest angles corresponding to nearly pure local mode I growth were measured for nickel and austenitic steel. The differences can be attributed to a different number of slip systems available in crystal structures of these metals (bcc, hcp and fcc) as reported for pure mode II and III cracks in more detail in [3]. Influence of crystallography was observed in all materials except for the austenitic steel.

Table 10. Comparison of mean deviation angles of mode II, mode III and mixed-mode II + III cracks.

Mode	Angle	ARMCO [°]	Titanium [°]	Nickel [°]	Austenitic steel [°]
II + III	γ_{II+III}	**15 ± 8**	**36 ± 16**	**45 ± 15**	**45 ± 15**
II	γ_{II}	21 ± 11	32 ± 13	45 ± 17	39 ± 5
III	γ_{III}	21 ± 13	34 ± 15	34 ± 14	32 ± 11

The average angles γ_{II} are nearly equal to γ_{III} ones in ARMCO iron and titanium, while $\gamma_{II} > \gamma_{III}$ in nickel and austenitic steel. The latter unequality corresponds to the fact that the maximum local mode I deviations can reach 70° for remote mode II cracks but only 45° for remote mode III ones. The values of γ_{II+III} are rather close to those of γ_{II} in all materials and higher than γ_{III} in nickel and austenitic steel. The obtained results provide a useful basis for an assessment of micromechanisms of mixed-mode II + III crack propagation and a quantitative interpretation of values of the intrinsic II + III threshold in these materials.

4 Conclusions

Experiments were done in the near-threshold region of the shear-mode crack growth in metallic materials and brought new data on effective crack growth thresholds for ARMCO iron, α-titanium, nickel and austenitic steel. The physical background of both the intrinsic resistance to shear-mode crack propagation and a simple crack branching criterion was presented.

Experimental data were obtained for two types of specimens for each of loading modes II and III. Observations of fracture surfaces in three dimensions were done by means of stereophotogrammetry in SEM.

Analysis of crack deviation angles revealed that in the ARMCO iron the cracks deflected and twisted randomly in all directions by a small angle ~ 20° and that the crack propagated along the maximum shear plane. The facets in the ARMCO iron indicated a significant influence of crystallography. In austenitic steel the high deflection and twisting angles corresponded to local mode I branching in both remote mode II and remote mode III. No crystallographic influence was observed in austenitic steel. According to these observations, the model of shielding dislocations (described in Sub-section 1.3.1) can be attributed to crack growth in the ARMCO iron and the model of absorption of antishielding dislocations (in Sub-section 1.3.2) can be applied on crack growth in the austenitic steel.

There is a principal difference between the mechanisms of mode II and mode III crack growth in the near-threshold region. In the first case, the mode I component induced by a deflection from the precrack plane usually accelerates mode II crack propagation due to a reduced friction. In the latter case, a deceleration of the mode III crack growth caused by twisting to local mode I and the related clamping of crack-wake asperities is mostly observed, particularly in materials forming the factory-roof morphology.

In all investigated materials, the effective thresholds $\Delta K_{\mathrm{IIeff,th}}$ under the remote mode II loading were found to be about 1.7 times lower than the thresholds $\Delta K_{\mathrm{IIIeff,th}}$ under the remote mode III loading. This is in a qualitative accordance with a prediction of mode III growth models based on the local mode II displacements but it also indicates a certain contribution of other mechanisms as the accumulative damage (microcracking) inside the cyclic plastic zone.

These results are a good contribution to understanding of nature of shear-mode crack propagation in metallic materials. The work also presents an application of the approach of micromechanics of fracture in the fields of fracture mechanics and materials science.

4.1 The Most Significant New Scientific Findings

Effective thresholds under mode I and mode II loading of investigated materials follow the relationships $\Delta K_{\mathrm{Ieff,th}} = 3E\sqrt{b}/4$ and $\Delta K_{\mathrm{IIeff,th}} = G\sqrt{b}/n_{\alpha}$, respectively, where E and G are the respective Young's and shear moduli, b is the magnitude of Burgers vector and n_{α} is a function of mean deflection angle α_{IIm}: $n_{\alpha,\mathrm{bcc}} \approx 0.9$, $n_{\alpha,\mathrm{hcp}} \approx 0.6$ and $n_{\alpha,\mathrm{fcc}} \approx 0.4$ can roughly be assumed for bcc, hcp and fcc metals, respectively. Consequently, the intrinsic resistance to shear-mode crack growth is predetermined by strength of interatomic bonds (G), manoeuvrability of dislocations (b) and the number of slip systems in the lattice (n_{α}).

The simple criterion $1.15\Delta K_{\mathrm{IIeff,th}} \geq \Delta K_{\mathrm{Ieff,th}}$ for mode I branching well reflects a transition

from the shear-mode to the opening-mode controlled crack propagation. The associated deflection angle $\alpha_{IIts} \approx 40°$ practically does not depend on a material.

These results bring the important possibility of comparison of the effective thresholds with results of theoretical models. They also enable predicting of the closure component by subtracting the effective value from the applied loading.

Finally, it should be emphasized that the level of friction-induced closure component is usually several times higher than the effective one in the near-threshold region. Therefore, the shear-mode crack growth behaviour is predominantly determined by extrinsic factors, which can also be estimated based on the applied load and the intrinsic factors. This work presents a new way to find the intrinsic resistance to shear-mode crack growth in metallic materials.

4.2 Author's Contributions

The first contribution that should be mentioned is that the author conducted the experimental procedure, which was a demanding process as regards both time consumption and technical skills. Under the guidance of his supervisor Prof. Pokluda and special supervisors at the Erich Schmid Institute of Austrian Academy of Sciences (ESI AAS) Prof. Pippan and Dr. Hohenwarter the author managed to successfully accomplish all experiments and observations individually. This work along with the visits of Prof. Pokluda maintained and deepened the cooperation between Brno University of Technology and the ESI AAS.

The most important scientific contributions are the outcomes in the form of new findings about shear-mode cracks published in articles in well impacted international journals. The author was the main writing author of one article published in Engineering Fracture Mechanics (IF = 1.41), was involved in author writing of one article published in Acta Materialia (IF = 3.94) and had a co-author participation of one overview article published in Fatigue & Fracture of Engineering Materials & Structures (IF = 0.86).

Another contribution was author's active participations at international conferences, from which he had an oral presentation at nine of them. Several articles were published in the conference proceedings or in journals indexed in the SCOPUS.

4.3 Follow-up Research in the Future

The results indicate that the effective thresholds for mode III are higher than that for mode II, for all four investigated materials. Also application of micromechanistic models was proposed to explanation some of the observed phenomena. These findings need to be verified by conducting experiments on other materials. Currently (2014), experiments for modes II and III in ferritic-pearlitic steel are in process. Other experiments are planned for pure pearlitic steel and the Ti-6Al-4V alloy. Further verification of results for single-phase bcc and hcp metals is planned to be done for niobium and zirconium.

A deeper analysis and discussion should be done on the appropriate description of mixed-mode II + III cracks propagation. Optimized criteria for evaluation of near-threshold data can be used in multiaxial fatigue research in the future.

References

[1] LAWN, B. R.; WILSHAW, T. R. *Fracture of Solids*. Cambridge: Cambridge University Press, 1975.

[2] OTSUKA, A; MORI, K; MYIATI, T. The condition of fatigue crack growth in mixed mode condition. *Engineering Fracture Mechanics*, 1975, vol. 7, pp. 429-439.

[3] SWEDLOW, J. L. Criteria for growth of the angled cracks. *Cracks and Fracture*, ASTM STP 601, 1976, West Conshohocken: ASTM, pp. 506-521.

[4] HOURLIER, F.; McLEAN, D.; PINEAU, A. Fatigue crack growth behaviour of Ti-5Al-2·5Sn alloy under complex stress (mode I + steady mode III). *Metals Technology*, 1978, vol. 5, pp. 154-158.

[5] HOURLIER, F.; PINEAU, A. Propagation of fatigue cracks under polymodal loading. *Fatigue & Fracture of Engineering Materials & Structures,* 1982, vol. 5, pp. 287-302.

[6] TSCHEGG, E. K. The influence of the static load mode I and R ratio on mode III fatigue crack growth behaviour in mild steel. *Materials Science and Engineering*, 1982, vol. 54, pp. 127-136.

[7] TSCHEGG, E. K.; RITCHIE, R. O.; McCLINTOCK, F. A. On the influence of rubbing fracture surfaces on fatigue crack propagation in mode III. *International Journal of Fatigue*, 1983, vol. 5, pp. 29-35.

[8] TSCHEGG, E. K. Sliding mode crack closure and mode III fatigue crack growth in mild steel. *Acta Metallurgica*, 1984, vol. 31, pp. 1323-1330.

[9] POOK, L. P. The fatigue crack direction and threshold behaviour of mild steel under mixed mode I and III loading. *International Journal of Fatigue*, 1985, vol. 7, pp. 21-30.

[10] BROWN, M. W.; HAY, E.; MILLER, K. J. Fatigue at notches subjected to reversed torsion and static axial loads. *Fatigue & Fracture of Engineering Materials & Structures*, 1985, vol. 8, pp. 243-258.

[11] OTSUKA, A.; MORI, K.; TOGHO, K. Mode II fatigue crack growth in aluminium alloys. *Current Japanese Materials Research*, 1987, vol. 1, pp. 163-185.

[12] TSCHEGG, E. K.; STANZL, S. E. The significance of sliding mode crack closure on mode III fatigue crack growth. *Basic questions in fatigue*, ASTM STP 924, vol. 1, West Conshohocken: ASTM, 1988, pp. 214-232.

[13] HELLIER, A. K.; McGIRR, M. B.; CORDEROY, D. J. H. A finite element and fatigue threshold study of shelling in heavy haul rails. *Wear*, 1991, vol. 144, pp. 289-306.

[14] DOQUET, V.; POMMIER, S. Fatigue crack growth under non-proportional mixed-mode loading in ferritic-pearlitic steel. *Fatigue & Fracture of Engineering Materials & Structures*, 2004, vol. 27, pp. 1051-1060.

[15] VAZIRI, A.; NAYEB-HASHEMI, H. The effect of crack surface interaction on the stress intensity factor in Mode III crack growth in round shafts. *Engineering Fracture Mechanics*, 2005, vol. 72, pp. 617-629.

[16] POKLUDA, J; TRATTNIG, G.; MARTINSCHITZ, C.; PIPPAN, R. Straightforward comparison of fatigue crack growth under modes II and III. *International Journal of Fatigue*, 2008, vol. 30, pp. 1498-1506.

[17] DOQUET, V.; BUI, Q. H.; BERTOLINO G.; MERHY, E.; ALVES, L. 3D shear-mode fatigue crack growth in maraging steel and Ti-6Al-4V. *International Journal of Fracture*, 2010, vol. 165, pp. 61-76.

[18] TARANTINO, M. G.; BERETTA, S.; FOLETTI, S.; PAPADOPOULOS, I. Experiments under pure shear and rolling contact fatigue conditions: Competition between tensile and shear mode crack growth. *International Journal of Fatigue*, 2013, vol. 46, pp. 67-80.

[19] POKLUDA, J.; ŠANDERA, P. *Micromechanisms of Fracture and Fatigue*. London: Springer, 2010. 295 p. ISBN 978-1-84996-265-0.

[20] POLÁK, J. *Cyclic Plasticity and Low Cycle Fatigue of Metals*. Praha: Academia, 1991.

[21] UHNÁKOVÁ, A.; POKLUDA, J.; MACHOVÁ, A.; HORA, P. 3D atomistic simulation of fatigue behaviour of cracked single crystal of bcc iron loaded in mode III. *International Journal of Fatigue*, 2011, vol. 33, pp. 1564-1573.

[22] UHNÁKOVÁ, A.; POKLUDA, J.; MACHOVÁ, A.; HORA, P. 3D atomistic simulation of fatigue behavior of a ductile crack in bcc iron loaded in mode II. *Computational Material Science*, 2012, vol. 61, pp. 12-19.

[23] RITCHIE, R. O. Mechanisms of fatigue crack propagation in metals, ceramics and composites: Role of crack tip shielding. *Materials Science and Engineering: A*, 1988, vol. 103, pp. 15-28.

[24] SURESH, S. *Fatigue of Materials.* Cambridge: Cambridge University Press, 1998, 704 p.

[25] POKLUDA, J.; ŠANDERA, P.; HORNÍKOVÁ, J. Statistical Approach to Roughness-Induced Shielding Effects. *Fatigue & Fracture of Engineering Materials & Structures*, 2004, vol. 27, pp. 141-157.

[26] GROSS, T. S.; MENDELSOHN, D. Mode I stress intensity factors induced by fracture surface roughness under pure mode III loading: application to the effect of loading modes on stress corrosion crack growth. *Metallurgical Transactions*, 1989, vol. 20A, 1989-1999.

[27] POKLUDA, J.; SLÁMEČKA, K.; ŠANDERA, P. Mechanism of factory-roof formation. *Engineering Fracture Mechanics*, 2010, vol. 77, pp. 1763-1771.

[28] TANAKA, K. Small Crack Propagation in Multiaxial Notch Fatigue. In *Crack Paths (CP 2012)*, Ed. A. CARPINTERI, F. IACOVIELLO, L. P. POOK, L. SUSMEL, Gaeta: Gruppo Italiano Frattura, 2012, pp. 31-45.

[29] TANAKA, K.; IWATA, Y.; AKINIWA, Y. Fatigue crack propagation in lead-free solder under mode I and II loading. *Transactions of the Japan Society of Mechanical Engineers*, 2009, vol. 75, pp. 1738-1745.

[30] HOLÁŇ, L.; POKLUDA, J.; SLÁMEČKA, K. Local Aspects of Shear-mode Crack Propagation in Austenitic Steel. *Chemické Listy*, 2010, vol. 104, pp. 314-317.

[31] POOK, L. P. *Crack Paths*. Southampton-Boston: Wit Press, 2002. 154 p. ISBN 978-1-8531-2927-8

[32] MURAKAMI, Y.; KUSUMOTO, R.; TAKAHASHI, K. Growth mechanism and threshold of mode II and mode III fatigue crack. *Fracture mechanics beyond 2000 (ECF 14)*, vol. II. Sheffield: EMAS, 2002, pp. 493-500.

[33] RITCHIE, R. O.; McCLINTOCK, F. A.; NAYEB-HASHEMI, H.; RITTER, M. A. Mode III fatigue crack propagation in low alloy steel. *Metallurgical Transactions A*, 1982, vol. 13, pp. 101-110.

[34] NAYEB-HASHEMI, H.; McCLINTOCK, F. A.; RITCHIE, R. O. Micro-mechanical modelling of mode III fatigue crack growth in rotor steels. *International Journal of Fracture*, 1983, vol. 23, pp. 163-185.

[35] HELLIER, A. K.; McGIRR, M. B.; CORDEROY, D. J. H.; KUTAJCZYK, L. A. Fatigue of head hardened rail steel under mode III loading. *International Journal of Fracture*, 1990, vol. 42, pp. R19-R23.

[36] JAMES, M.; HERMAN, D. J.; SCOTT, F. Crack Growth Rate Stress Intensity Factor Corrections for Out-of-Plane Crack Growth. In *Fatigue and Fracture Mechanics*. Ed. S. R. DANIEWITZ, J. C. NEWMAN, K. H. SCHWALBE, West Conshohocken: ASTM, 2003.

[37] SCHÖLLMANN, M.; FULLAND, M.; RICHARD, H. A. Development of a new software for adaptive crack growth simulations in 3D structures. *Engineering Fracture Mechanics*, 2003, vol. 70, pp. 249-268.

[38] POKLUDA, J.; PIPPAN, R. Can a pure mode III fatigue loading contribute to crack propagation in metallic materials? *Fatigue & Fracture of Engineering Materials & Structures*, 2005, vol. 28, pp. 179-186.

[39] PIPPAN, R.; GUMBSCH, P. *Multiscale Modelling of Plasticity and Fracture by Means of Dislocation Mechanics*. CISM Coursed and Lectures, vol. 522, Wien-New York: Springer, 2010, 394 p. ISBN 978-3-7091-0283-1.

[40] PIPPAN, R. Dislocation emission and fatigue crack-growth threshold. *Acta Metallurgica et Materialia*, 1991, vol. 39, pp. 255-262.

[41] RIEMELMOSER, F. O.; GUMBSCH, P.; PIPPAN, R. Dislocation modelling of fatigue cracks: An overview. *Materials Transactions, JIM*, 2001, vol. 42, pp. 2-13.

[42] PIPPAN, R.; RIEMELMOSER, F. O.; WEINHANDL, H.; KREUZER, H. Plasticity-induced crack closure under plane-strain conditions in the near-threshold regime. *Philosophical Magazine A*, 2002, vol. 82, pp. 3299-3309.

[43] DESHPANDE, V. S.; NEEDLEMAN, A; VAN DER GIESSEN, E. A discrete dislocation analysis of near-threshold fatigue crack growth. *Acta Materialia*, 2001, vol. 49, pp. 3189-3203.

[44] VAN DER GIESSEN, E; DESHPANDE, V. S.; CLEVERINGA, H. H. M.; NEEDLEMAN, A. Discrete dislocation plasticity and crack tip fields in single crystals. *Journal of the Mechanics and Physics of Solids*, 2001, vol. 49, pp. 2133-2153.

[45] PELLOUX, R. M. N. Mechanisms of formation of ductile fatigue striations. *ASM Transactions Quarterly*, 1969, vol. 62, pp. 281-287.

[46] NEUMANN, P. New experiments concerning slip processes at propagating fatigue cracks. *Acta Metallurgica*, 1974, vol. 22, pp. 1155-1165.

[47] VEHOFF, H. Crack propagation and cleavage initiation in Fe-2.6 percent Si single-crystals under controlled plastic crack tip opening rate in various gaseous environments. *Acta Materialia*, 1980, vol. 28, pp. 265-272.

[48] PIPPAN, R.; ZELGER, C.; GACH, E.; BICHLER, C.; WEINHANDL, H. On the mechanism of fatigue crack propagation in ductile metallic materials. *Fatigue & Fracture of Engineering Materials & Structures*, 2011, vol. 34, pp. 1-16.

[49] WEERTMAN, J. Rate of growth of fatigue cracks calculated from the theory of infinitesimal dislocations distributed on a plane. *International Journal of Fracture Mechanics*, 1966, vol. 2, pp. 460-467.

[50] VOJTEK, T.; PIPPAN, R.; HOHENWARTER, A.; HOLÁŇ, L.; POKLUDA, J. Near-threshold propagation of mode II and mode III fatigue cracks in ferrite and austenite. *Acta Materialia*, 2013, vol. 61, pp. 4625-4635.

[51] POKLUDA, J.; SLÁMEČKA, K.; ŠANDERA, P. On the Mechanism of Factory-Roof Formation. In *Crack Paths (CP 2009)*. Ed. B. ATZORI, A. CARPINTERI, P. LAZZARIN, L. P. POOK, Vicenza: University of Padua, 2009, pp. 155 – 166.

[52] POKLUDA, J; PIPPAN, R.; VOJTEK, T.; HOHENWARTER, A. Near-threshold Behaviour of Shear-mode Fatigue Cracks in Metallic Materials. *Fatigue & Fracture of Engineering Materials & Structures*, 2014, vol. 37, pp. 232-254.

[53] TANAKA, K.; AKINAWA, Y.; YU, H. The propagation of a circumferential fatigue crack in medium-carbon steel bars under combined torsional and axial loadings. *Mixed-mode crack behaviour*, ASTM 1359, West Conshohocken: ASTM, 1999, pp. 295-311.

[54] PONS, A. J.; KARMA, A. Helical crack front instability in mixed-mode loading. *Nature*, 2010, vol. 464, pp. 85-89.

[55] LEBLOND, J. B.; KARMA, A.; LAZARUS, V. Theoretical analysis of crack front instability in mode I + III, *Journal of the Mechanics and Physics of Solids*, 2011, vol. 59, pp. 1872-1887.

[56] POOK, L. P. A 50-year retrospective review of three-dimensional effects at cracks and sharp notches. *Fatigue & Fracture of Engineering Materials & Structures*, 2013, vol. 36, pp. 699-723.

[57] VATNE, I. R.; STUKOWSKI, A.; THAULOW, C.; OSTBY, E.; MARIAN, J. Three-dimensional crack initiation mechanisms in bcc-Fe under loading modes I, II and III. *Materials Science and Engineering A*, 2013, vol. 560, pp. 306-331.

[58] OHR, S. M. An electron microscope study of crack tip deformation and its impact on the dislocation theory of fracture. *Materials Science and Engineering*, 1985, vol. 72, pp. 1-35.

[59] MURAKAMI, Y. *Metal Fatigue: Effects of small defects and nonmetallic inclusions*. Amsterdam – Tokyo: Elsevier, 2002.

[60] TONG, J.; YATES, J. R.; BROWN, M. W. The formation and propagation of mode I branch cracks in mixed mode fatigue failure. *Engineering Fracture Mechanics*, 1997, vol. 56, pp. 213-231.

[61] DOQUET, V.; ABADI, M.; BUI, Q. H.; PONS, A. Influence of the loading path on fatigue crack growth under mixed-mode loading. *International Journal of Fracture*, 2009, vol. 159, pp. 219-232.

[62] CAMPBELL, J. P.; RITCHIE, R. O. Mixed mode, high-cycle fatigue-crack growth thresholds in Ti-6Al-4V: I. A comparison of large- and short-crack behavior. *Engineering Fracture Mechanics*, 2000, vol. 67, pp. 209-227.

[63] MERATI, A. A.; HELLIER, A. K.; ZARRABI, K. On the mixed mode II/III fatigue threshold behaviour for aluminium alloys 2014-T6 and 7075-T6. *Fatigue & Fracture of Engineering Materials & Structures*, 2011, vol. 35, pp. 2-12.

[64] TONG, J.; YATES, J. R.; BROWN, M. W. Some aspects of fatigue thresholds under mode III and mixed mode III and I loadings. *International Journal of Fatigue*, 1996, vol. 18, pp. 279-285.

[65] BERETTA, S.; FOLETTI, S.; VALIULIN, K. Fatigue crack propagation and threshold for shallow micro-cracks under out-of-phase multiaxial loading in a gear steel. *Engineering Fracture Mechanics*, 2010, vol. 77, pp. 1835-1848.

[66] HOLÁŇ, L.; HOHENWARTER, A.; SLÁMEČKA, K.; PIPPAN, R.; POKLUDA, J. Experimental Evaluation of Fatigue Long Crack Propagation under Remote Shear Loading Modes II and III. *Materials Science and Technology* (ISSN: 1335-9053), 2008, vol. 8, pp. 55-59.

[67] VOJTEK, T.; POKLUDA, J.; HOHENWARTER, A.; PIPPAN, R. Three-dimensional Morphology of Fracture Surfaces Generated by Modes II and III Fatigue Loading in Ferrite and Austenite. *Engineering Fracture Mechanics*, 2013, vol. 10, pp. 285-293.

[68] QIAN, J.; FATEMI, A. Mixed mode fatigue crack growth: A literature survey. *Engineering Fracture Mechanics*, 1996, vol. 55, pp. 969-990.

[69] CHELL, G. G.; GIRVAN, E. An experimental technique for fast fracture testing in mixed mode. *International Journal of Fatigue*, 1978, vol. 14, pp. R81-R84.

[70] HELLIER, A. K.; CORDEROY, D. J. H.; McGIRR, M. B. A practical mixed mode II/III fatigue test rig. *International Journal of Fatigue*, 1987, vol. 9, pp. 95-101.

[71] FREMY, F.; POMMIER, S.; PONCELET, M.; RAKA, B.; GALENNE, E.; COURTIN, S.; LE ROUX, J. C. Load path effect on fatigue crack propagation in I + II + III mixed mode conditions – Part 1: Experimental investigations. *International Journal of Fatigue*, 2014, vol. 62, pp. 104-112.

[72] RICHARD, H. A.; BENITZ, K. Loading device for the creation of mixed mode in fracture mechanics. *International Journal of Fracture*, 1983, vol. 22, pp. R55-58.

[73] DOQUET, V.; BERTOLINO, G. Local approach to fatigue cracks bifurcation. *International Journal of Fracture*, 2008, vol. 30, pp. 942-950.

[74] PLANK, R.; KUHN, G. Fatigue crack propagation under non-proportional mixed mode loading. *Engineering Fracture Mechanics*, 1999, vol. 62, pp. 203-229.

[75] ZHAO, J.; GUO, W. Three-parameter K–T–Tz characterization of the crack-tip fields in compact-tension-shear specimens. *Engineering Fracture Mechanics*, 2012, vol. 92, pp. 72-88.

[76] BENTHEM, J. P.; KOITER, W. T. Asymptotic approximations to crack problems. *Mechanics of Fracture: Method of Analysis and Solutions of Crack Problems*, Ed. Sih G. C., Leyden: Noordhof International Publishing, 1973, pp. 131-178.

[77] NODA, Nao-Aki; TAKASE, Y. Generalized stress intensity factors of V-shaped notch in a round bar under torsion, tension, and bending. Engineering Fracture Mechanics, 2003, vol. 70, pp. 1447-1466.

[78] HORNÍKOVÁ, J.; ŠANDERA, P.; POKLUDA, J. Linear-Elastic and Elastoplastic Mode II and III Crack Tip Stress-Strain Fields in Cylindrical Specimens with Circumferential Crack. *Key Engineering Materials*, 2010, vol. 417-418, pp. 321-324, ISSN: 1662-9795.

[79] HORNÍKOVÁ, J.; ŽÁK, S.; ŠANDERA, P. K-calibration of special specimen for Mode II, III and II+III Crack Growth. *Engineering Fracture Mechanics*, 2013, vol. 110, pp. 430-437.

[80] PIPPAN, R. The growth of short cracks under cyclic compression. *Fatigue & Fracture of Engineering Materials & Structures*, 1987, vol. 9, pp. 319-328.

[81] PIPPAN, R. The length and shape of cracks under cyclic compression – the influence of notch geometry. *Engineering Fracture Mechanics*, 1988, vol. 31, pp. 715-718.

[82] PIPPAN, R.; BERGER, M.; STÜWE, H. P. The influence of crack length on fatigue crack growth in deep sharp notches. *Metallurgical Transactions A*, 1987, vol. 18, pp 429-435.

[83] MURAKAMI, Y. Editor-in-Chief. *Stress Intensity Factors Handbook*. Vols. 1 and 2, Oxford: Pergamon Press, 1987.

[84] VOJTEK, T.; POKLUDA, J.; ŠANDERA, P.; HORNÍKOVÁ, J.; SLÁMEČKA, K.; HOHENWARTER, A.; PIPPAN, R. Near-threshold Fatigue Crack Propagation under Mixed-mode II+III in ARMCO Iron. In *Fracture Mechanics for Durability, Reliability and Safety (ECF19)*. Ed. R. GOLDSTEIN, Kazan: Kazan Scientific Centre of the Russian Academy of Sciences, 2012, p. 188 (CD ROM).

[85] STAMPFL, J.; SCHERER, S; GRUBER, M.; KOLEDNIK, O. Reconstruction of surface topographies by scanning electron microscopy for application in fracture research. *Applied Physics A*, 1996, vol. 63, pp. 341-346.

[86] SEMPRIMOSCHNIG, C. O. A.; STAMPFL, J.; PIPPAN, R.; KOLEDNIK, O. A new powerful tool for surveying cleavage fracture surfaces. *Fatigue & Fracture of Engineering Materials & Structures*, 1997, vol. 20, pp. 1541-1550.

[87] HORNÍKOVÁ, J.; ŠANDERA, P.; ŽÁK, S.; POKLUDA, J. Specimens for Simultaneous Mode II, III and II+III Fatigue Crack Propagation: Elasto-Plastic Solution of Crack Tip Stress-Strain Field. *Advanced Materials Research*, 2014, vol. 891-892, pp. 1585-1590.

[88] KLESNIL, M.; LUKÁŠ, P. *Fatigue of Metallic Materials*. Amsterdam: Elsevier, 1992, 270 p.

[89] DOQUET, V.; BERTOLINO, G. A material and environment-dependent criterion for the prediction of fatigue crack paths in metallic structures. *Engineering Fracture Mechanics*, 2008, vol. 75, pp. 3399-3412.

[90] LIAW, P. K.; LEA, T. R.; LOGSDON, W. A. Near-threshold fatigue crack growth behavior in metals. *Acta Metallurgica*, 1983, vol. 31, pp. 1581-1587.

[91] SHIN, D. H.; KIM, I.; KIM, J.; KIM, Y. S.; SEMIATIN, S. L. Microstructure development during equal-channel angular pressing of titanium. *Acta Materialia*, 2003, vol. 51, pp. 983-996.

[92] BANERJEE, D.; WILLIAMS, J. C. Perspectives on Titanium Science and Technology. *Acta Materialia*, 2013, vol. 61, pp. 844-879.

[93] POKLUDA, J.; KONDO, Y.; SLÁMEČKA, K.; ŠANDERA, P.; HORNÍKOVÁ, J. Assessment of Extrinsic Crack Tip Shielding in Austenitic Steel near Fatigue Threshold. *Key Engng. Mater.*, 2008, vol. 385-387, pp. 49-52.

[94] PIPPAN, R. Threshold and effective threshold of fatigue crack propagation in ARMCO iron I: The influence of grain size and cold working. *Materials Science and Engineering A*, 1991, vol. 138, pp. 1-13.

[95] IRWING, P. E.; ROBINSON, J. L.; BEEVERS, C. J. Fatigue crack closure in titanium and titanium alloys. *International Journal of Fracture*, 1973, vol. 9, pp. 105-108.

[96] BOYCE, B. L.; RITCHIE, R. O. Effect of load ratio and maximum stress intensity on the fatigue threshold in Ti-6Al-4V. *Engineering Fracture Mechanics*, 2001, vol. 68, pp. 129-147.

[97] VOJTEK, T.; POKLUDA, J.; ŠANDERA, P.; HORNÍKOVÁ, J.; HOHENWARTER, A.; PIPPAN, R. Analysis of Fatigue Crack Propagation under Mixed Mode II+III in ARMCO Iron. *International Journal of Fatigue*, submitted to.

[98] VOJTEK, T.; POKLUDA, J.; HOHENWARTER, A.; SLÁMEČKA, K.; PIPPAN, R. 3D Morphology of Fracture Surfaces Created by Mixed-mode II+III Fatigue Loading in Metallic Materials. *Procedia Engineering*, 2014, in print.

Nomenclature

bcc	body centred cubic
fcc	face centred cubic
hcp	hexagonal close packed
CTS	compact-tension shear specimen
FEA	finite element analysis
FEM	finite element method
SEM	scanning electron microscope
SFE	stacking-fault energy
SIF	stress intensity factor
SIFR	stress intensity factor range

a	total crack length
a_{L}	lattice parameter
$(\Delta a/\Delta N)_{\mathrm{I}}$	fatigue crack growth rate in remote mode I
$(\Delta a/\Delta N)_{\mathrm{II}}$	fatigue crack growth rate in remote mode II
$(\Delta a/\Delta N)_{\mathrm{III}}$	fatigue crack growth rate in remote mode III
A	coefficient in Klesnil – Lukas formula
$\boldsymbol{b}$	Burgers vector in fcc and bcc lattices
$\boldsymbol{b}_{\mathbf{a+c}}$	Burgers vector in hcp lattice
b	magnitude of $\boldsymbol{b}$ Burgers vector
d	inner diameter of simple-shear specimen
d_{m}	mean grain size
D	outer diameter of simple-shear specimen
E	Young's modulus
F	applied force
F_{c}	applied compressive force
G	shear modulus
G_{E}	crack driving force
k_{IIe}	monotonic mode II threshold for dislocation emission
k_{IIIe}	monotonic mode III threshold for dislocation emission
K_{II}	remote mode II SIF
K_{III}	remote mode III SIF
$K_{\mathrm{II,ind}}$	induced mode II SIF
$K_{\mathrm{III,ind}}$	induced mode III SIF
K_{G}	Griffith's SIF
l	length coordinate of a fracture surface profile
l_{n1}	notch depth in simple-shear specimen
l_{n2}	notch depth in CTS specimen
l_{o}	precrack length
l_{s}	shear crack length
n	exponent in Klesnil – Lukas formula
n_{α}	function of mean deflection angle
$n_{\alpha,\mathrm{bcc}}$	function of mean deflection angle for bcc structure

$n_{\alpha,fcc}$	function of mean deflection angle for fcc structure
$n_{\alpha,hcp}$	function of mean deflection angle for hcp structure
N	number of loading cycles
q_I	coefficient in Eqs. (22) and (22a)
q_{II}	coefficient in Eqs. (23) and (23a)
R	cyclic stress ratio
R^2.	coefficient of determination
r_p	size of cyclic plastic zone
t	CTS specimen thickness
T	applied torque
W	CTS specimen width
Y_{II}	geometry function of SIF for mode II loading
Y_{III}	geometry function of SIF for mode III loading
Y_{BK}	Benthem-Koiter's dimensionless stress intensity
z	height coordinate of a profile
α_{II}	angle of deflection of a remote mode II crack with respect to the shear plane
α_{III}	angle of deflection of a remote mode III crack with respect to the shear plane
α_{IId}	theoretical deflection angle of elementary mode I branch under remote mode II loading
α_{IIm}	mean deflection angle of elementary branch under remote mode II loading
α_{IIts}	mean transition angle of elementary branch under remote mode II loading
β_{II}	angle of twisting of a remote mode II crack with respect to the shear plane
β_{III}	angle of twisting of a remote mode III crack with respect to the shear plane
β_{IIIc}	critical twist angle of elementary branch under remote mode III loading
Δk_{Id}	local mode I SIFR at deflected crack front under remote mode II loading
Δk_{It}	local mode I SIFR at twisted crack front under remote mode III loading
Δk_{Ie}	cyclic mode I threshold for dislocation emission
Δk_{IIe}	cyclic mode II threshold for dislocation emission
$\Delta k_{Ieff,d}$	local effective mode I SIFR at deflected crack front under remote mode II loading
$\Delta k_{Ieff,t}$	local effective mode I SIFR at twisted crack front under remote mode II loading
$\Delta k_{IIeff,d}$	local effective mode II SIFR at deflected crack front under remote mode II loading
$\Delta k_{IIIeff,t}$	local effective mode III SIFR at twisted crack front under remote mode III loading
ΔK_I	remote SIFR for mode I loading
ΔK_{II}	remote SIFR for mode II loading
ΔK_{III}	remote SIFR for mode III loading
ΔK_{eq}	equivalent SIFR for mixed mode II+II loading
$\Delta K_{I,th}$	crack growth threshold for remote mode I loading
$\Delta K_{II,th}$	crack growth threshold for remote mode II loading
$\Delta K_{III,th}$	crack growth threshold for remote mode III loading
ΔK_{IIeff}	effective SIFR for mode II loading
ΔK_{IIIeff}	effective SIFR for mode III loading
$\Delta K_{eff,eq}$	equivalent effective SIF for mixed mode II+III loading
$\Delta K_{Ieff,th}$	effective (intrinsic) crack growth threshold for mode I loading
$\Delta K_{IIeff,th}$	effective (intrinsic) crack growth threshold for mode II loading

$\Delta K_{\mathrm{IIIeff,th}}$	effective (intrinsic) crack growth threshold for mode III loading
φ	polar angle on the cross section of simple-shear specimen
κ_2, κ_3	coefficients in the normalized formula for sorting mixed-mode II+III data
λ	coefficient in the equivalent SIFR in mixed mode II+III
ν	Poisson's ratio
σ_{N}	nominal tensile stress
σ_{y}	yield stress in tension
τ	nominal shear stress
τ_{y}	yield stress in shear
$\tau_{\mathrm{III,global}}$	global mode III shear stress
$\tau^{\mathrm{A}}_{\mathrm{II,local}}$	local mode II component of global mode III shear stress in the first half-cycle
$\tau^{\mathrm{A}}_{\mathrm{III,local}}$	local mode III component of global mode III shear stress in the first half-cycle
$\tau^{\mathrm{A}}_{\mathrm{III,global}}$	global mode III shear stress in the first half-cycle
$\tau^{\mathrm{B}}_{\mathrm{II,local}}$	local mode II component of global mode III shear stress in the second half-cycle
ψ	orientation angle of the CTS specimen, 0° for pure mode I, 90° for pure mode II